The Pennsylvania State University

The Graduate School

Department of Electrical Engineering

ADVANCED LASER BEAM DEFLECTION AND LASER INDUCED ACTIVATION

A Dissertation in

Electrical Engineering

by

Ju-Hung Chao

Submitted in Partial Fulfillment
of the Requirements
for the Degree of

Doctor of Philosophy

May 2019

The dissertation of Ju-Hung Chao was reviewed and approved* by the following:

Shizhuo Yin
Professor of Electrical Engineering
Dissertation Advisor
Chair of Committee

James K. Breakall
Professor of Electrical Engineering

Victor P. Pasko
Professor of Electrical Engineering

Jian Hsu
Associate Professor of Engineering Science & Mechanics

Kultegin Aydin
Professor of Electrical Engineering
Head of the Department of Department of Electrical Engineering

*Signatures are on file in the Graduate School

ABSTRACT

A high-speed optical beam deflector based on potassium tantalate niobate ($KTa_{1-x}Nb_xO_3$ [KTN]) crystal, which has been used in swept-source optical coherence tomography (SSOCT), has been gaining interest for its potential application to laser measurement, sensing, imaging, printing, display, storage, and communication in advanced optical systems. The studies in this dissertation aimed to explore the unknown aspects of the KTN beam deflection technique and identify novel functionalities. Our investigation of non-uniform charge distribution in KTN crystals led us to develop a method to quantitatively simulate space-charge-controlled (SCC) beam deflection in KTN crystals with non-uniform charge distribution. Our method of dividing charge densities in KTN crystals with respect to the distance from the KTN cathode was experimentally verified and found to be useful when designing SCC KTN beam deflectors with non-uniform charge distribution. We also discovered that 2-D beam deflection can be achieved on a single piece of KTN crystal by combining space-charge-controlled (SCC) deflection and temperature-gradient-controlled (TGC) deflection. When a temperature gradient is induced on a SCC KTN beam deflector in a direction perpendicular to the external electric field, 2-D beam deflection occurs in the KTN crystal. In addition to beam deflection, I studied the high-speed laser activation technique involving SI-GaAs and a photoconductive semiconductor switch (PCSS). I identified unconventional lock-on behavior during non-linear switching in PCSS by activating the PCSS with optical beams of multiple wavelengths simultaneously. After bonding the activating portion of the PCSS with a ruby crystal, the PCSS was triggered by a combination of a 532-nm laser pulse and a 694-nm fluorescent light. This resulted in an ultra-long lock-on time (i.e., on the order of milliseconds) three orders of magnitude longer than the typical lock-on behavior in the non-linear switching mode of PCSS.

TABLE OF CONTENTS

LIST OF FIGURES

LIST OF TABLES

ACKNOWLEDGEMENTS

I would like to express my utmost gratitude to my advisor, Prof. Shizhuo Yin, who inspires me with his tremendous work ethic and passion for his work. He is always willing to offer support and guidance when I need help. I am very fortunate to have him as my advisor. Many thanks to Prof. James Breakall, Prof. Victor Pasko, and Prof. Jian Hsu for being on my dissertation committee and providing valuable remarks about my research.

I would also like to thank all of my colleagues throughout the years—Dr. Yun-Ching Chang, Dr. Chi-min Lin, Dr. Chao Wang, Dr. Jimmy Yao, Dr. Wenbin Zhu, Chang-Jiang Chen, Yun-Goo Lee, Annan Shang, and Ruijia Liu—for their help with research and support in my personal life.

I am very appreciative of Mary Ann Henderson, Maria DiCola, and SherryDawn Jackson, who have always been incredibly kind and helpful regardless of when I interacted with them at Penn State. Their jobs were not easy, but they really made a difference in my life.

My humblest gratitude to my parents, who have always believed in me and provided everything I needed. I am eternally indebted to them.

Last but not least, tremendous thanks to my wife, Angela, for her love and support.

The works in this dissertation had been partially funded by US Army Research Laboratory under Cooperative Agreement Number (W911NF-17-2-0135). The views and conclusions contained in this document are those of the authors and should not be interpreted as representing the official policies, either expressed or implied, of the Army Research Laboratory or the U.S. Government. The U.S. Government is authorized to reproduce and distribute reprints for Government purposes notwithstanding any copyright notation hereon.

Chapter 1

Introduction

An optical beam deflector is a key component that is used to change the direction of light in a range of advanced techniques, including imaging, sensing, printing, optical storage, and communication. Driven by the various needs of optical instruments and communication systems, including swept-source optical coherence tomography [1], laser displays [2], laser printing [3], switchable waveguides [4], and spectral multiplexed holograms [5], researchers have made a tremendous effort to develop different ways to enhance our ability to steer optical beams. Generally, there are two types of optical beam steering systems: mirror-based mechanical deflectors and optical solid-state deflectors. By far, the most advanced mechanical beam steering systems are rotating polygonal mirror scanners [6-8], microelectromechanical system (MEMS) mirror scanners [9–11], and piezoelectric beam deflectors [12,13]. Solid-state beam steering systems include acousto-optic deflectors (AODs) [14–16] and electro-optic deflectors (EODs) [17–18], as illustrated in Fig. 1-1.

Table 1-1 briefly compares the common properties of the aforementioned optical scanners. In comparison to mechanical beam deflectors, solid-state optical deflectors not only are free of the mechanical movement associated with refractive mirrors, and thus make much less noise and avoid wear and tear, but also feature much faster scanning speed, and therefore are better candidates for applications that require higher operation frequency. Both AODs and EODs can achieve high deflection velocities, short response time, and high angular accuracy. However, AODs suffer from heavily attenuated open-state transmittance, which significantly limits their application.

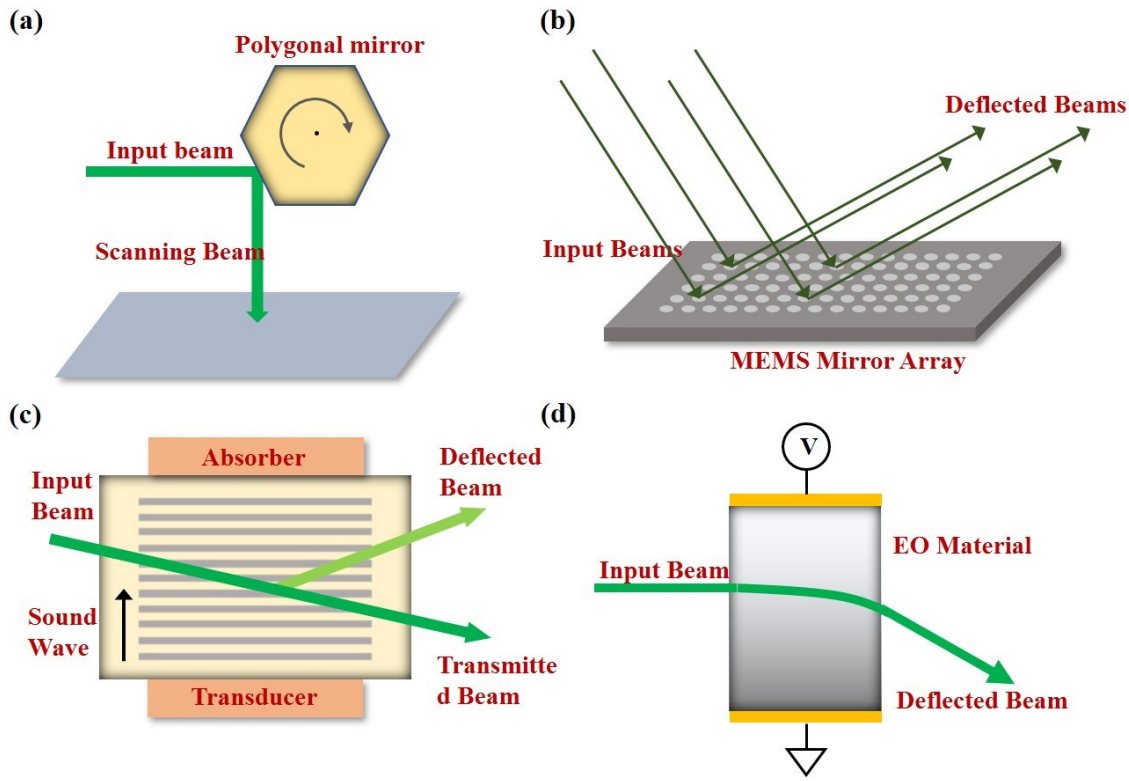

Figure **1-1**: Illustration of optical beam deflectors: (a) polygonal mirror deflector, (b) MEMS mirror deflector, (c) AO beam deflector, and (d) EO beam deflector.

Table **1-1**: Comparison of the properties of optical beam steering systems [19].

Beam steering technology	**Aperture size [mm]**	**Deflection angle [rad]**	**Scanning speed [10^3 rad/s]**	**Response time**	**Transmittance (Efficiency)**
Galvo deflector	7-30	0.5-1	0.1	ms	95%
Polygon deflector	2-12	0.6-1	1-10	$\gg$ ms	90%
Piezo deflector	10-25	0.01-0.1	0.01-0.1	ms	95%

MEMS - static	1-2.5	0.5	0.1-1	ms	90%
MEMS - resonant	1	0.5-1	10-30	$\gg$ ms	90%
AOD	1-10	0.01-0.05	5-250	μs	60-80%
EOD (Pockels)	2	0.001	2-20	ns	85%
EOD (Kerr)	0.5	0.2	40	ns	90%

By nature, EODs feature high scanning speed, high accuracy and control, fast response, and high efficiency across the visible wavelengths. Although they are not without limitations in terms of some factors, such as aperture size, they are the best option for high-speed beam steering. They can be divided into two types based on which EO effect is dominant: (1) the linear Pockels effect or (2) the quadratic Kerr effect. These effects are discussed in detail in chapter 2 of this dissertation.

Materials with a strong EO effect have been widely investigated. Typical Pockels cells, including zinc selenide (ZnSe), lithium niobite ($LiNbO_3$), and monopotassium phosphate (KDP), were found to have linear EO coefficients ranging from 10^{-13} to 10^{-12} m/V. Additionally, the quadratic EO coefficients of common Kerr cells, such as lead zirconate titanate (PLZT), barium titanate ($BaTiO_3$), and potassium tantalite niobite (KTN), were found to range from 10^{-15} to 10^{-14} m^2/V^2. Tables 1-2 and 1-3 list the largest EO coefficients found for Pockels and Kerr cells, respectively.

Table **1-2**: EO coefficients of Pockels cells [20].

Pockels cell	**r_{ij} (10^{-12} m/V)**
ZnSe	$r_{41} = 2.2$
ZnTe	$r_{41} = 4.5$
CdSe	$r_{33} = 4.3$
$LiNbO_3$	$r_{51} = 32.6$
$LiTaO_3$	$r_{33} = 33$
KH_2PO_4 (KDP)	$r_{63} = 10.3$
$(NH_4)H_2PO_4$ (ADP)	$r_{41} = 23.76$
$KNbO_3$	$r_{42} = 380$
$BaTiO_3$	$r_{51} = 1640$
$Ba_{0.25}Sr_{0.75}Nb_2O_6$	$r_{33} = 1340$
$KTa_{0.35}Nb_{0.65}O_3$	$r_{51} = 8000$

Table **1-3**. EO coefficients of Kerr cells [20].

Kerr cell	**s_{ij} (10^{-18} m/V)**
KH_2PO_4 (KDP)	s_{11} - s_{12} = -2.58
$(NH_4)H_2PO_4$ (ADP)	s_{11} - s_{12} = -1.63
$KTaO_3$	s_{11} - s_{12} = 10
$SrTiO_3$	s_{11} - s_{12} = 31
$BaTiO_3$	s_{11} - s_{12} = 2290
PLZT	s_{33} - s_{13} = 1768
$KTa_{0.6}Nb_{0.4}O_3$	s_{11} - s_{12} = 69400 [13]

Although numerous materials listed above have been adopted in high-speed EODs, most suffer from relatively small EO coefficients. $KTa_{0.6}Nb_{0.4}O_3$ (KTN), which was made available in large high-quality single crystals with the state-of-the-art top-seed solution growth (TSSG) techniques only a decade ago [21], stands out due to its exceptionally large EO coefficient. Thus, interest in KTN crystal's potential application in, for example, EO switches, modulators, dynamic waveguides, high-speed beam scanners, wavelength-tunable lasers, optical coherent tomography, and holographic memory systems [22-32], has been rapidly growing.

One of the most successful applications of KTN crystal is in the commercialized space-charge-controlled (SCC) KTN beam deflector developed by Japanese researchers [33, 34]. SCC beam deflection proceeds as follows: the incoming laser beam is deflected in the crystal by an electric-field-dependent prism-shaped refractive index distribution inside the KTN crystal, which

is formed when charge carriers are injected into the crystal and trapped by the defects inside. Figure 1-1 depicts a SCC KTN beam deflector. In this model, beam deflection in the x-direction is expressed as follows:

$$\theta(x) = -n^3 g_{11} e^2 N^2 L \left(x - \frac{d}{2} + \frac{\varepsilon V}{eNd} \right), \tag{1.1}$$

where n is the refractive index, g_{11} is the effective Kerr coefficient, N is the pre-injected space-charge density, L is the propagation length of light in the crystal, d is the distance between the two electrodes, ε is the permittivity, e is the electron charge, and V is the applied voltage. It is evident that deflection is directly proportional to the applied voltage. Details about the working mechanism of the SCC deflector are presented in Chapter 4. Because beam deflection is solely dependent on the applied voltage field, as all other parameters are predetermined upon operation, the speed of beam deflection is significantly affected by the speed of the driving source. Currently, the scanning frequency of an commercialized SCC beam deflector can be as high as 700 kHz [35].

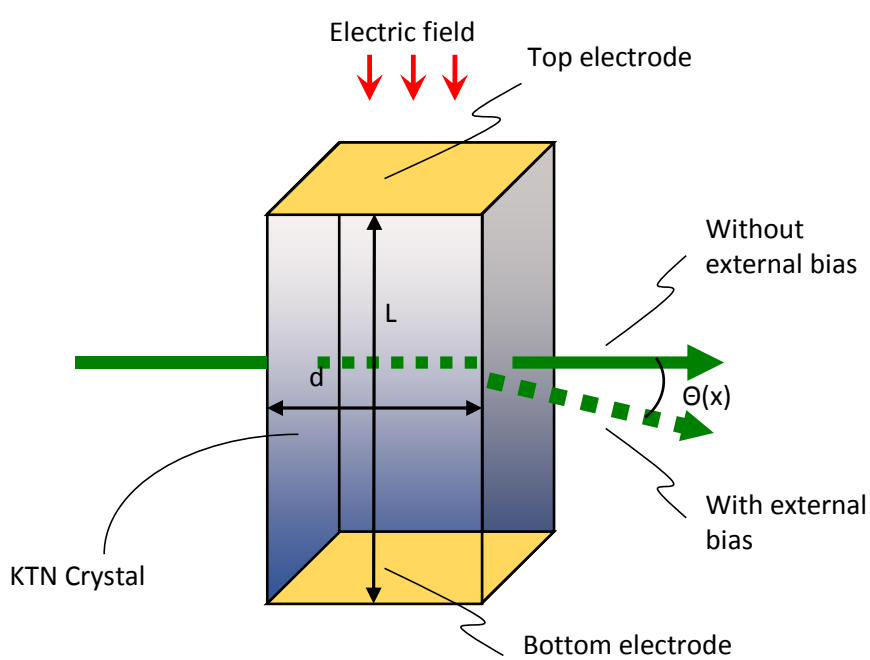

Figure **1-2**: Illustration of a SCC KTN beam deflector.

Although the SCC beam deflector has been well-investigated and commercialized, much about it remains unexplored. For example, the physical model of the SCC beam deflector was based on a KTN crystal with a uniform charge distribution. However, according to a recent report, the charge distribution inside a KTN crystal can be non-uniform [36]. Therefore, it is worth investigating non-uniform SCC beam deflectors. In this study, a model was built to describe a non-uniform SCC beam deflector, and an experiment was conducted to verify the model.

The SCC beam deflector can only perform beam deflection in a direction parallel to its electrodes. In other words, multiple deflectors are needed to perform 2-D or 3-D beam steering, increasing the costs and complications associated with the process. To this end, we have discovered a novel way to perform 2-D beam deflection using KTN single crystal that involves adding another deflection mechanism—temperature-gradient-induced beam deflection—to the existing SCC beam deflector. By employing both beam deflection mechanisms and setting the directions of deflection to be perpendicular to each other, 2-D beam steering can be performed. In this study, we comprehensively analyzed the mechanism of temperature-gradient beam deflection in KTN crystal. In addition, the effects of space-charge and temperature-gradient mechanisms were quantitatively analyzed and experimentally confirmed. This allowed us to develop a compact, 2-D, large-bandwidth, and high-speed beam deflector. In theory, proper selection of the temperature gradient and external driving field for KTN crystal are needed to scan the full projecting plane. This finding expands the functionality of KTN beam deflectors and can be used to improve many applications of KTN beam deflectors in the fields of advanced imaging, printing, and communication.

As mentioned previously, the speed of KTN beam deflector is greatly impacted by its driving source. In other words, the speed of the entire system is limited by the part with the least speed. The quadratic Kerr effect of KTN crystal can be expressed as follows:

$$s_{11} - s_{12} = \frac{\lambda d^2}{n^3 L V^2}, \tag{1.2}$$

where λ is the wavelength, d is the distance between the electrodes, n is the refractive index of KTN, L is the propagation length of light, and V is the driving voltage. Insertion of practical numbers into Eq. 1.2 provides a driving voltage, V, ranging roughly from hundreds to several thousands of volts. Unfortunately, it is often difficult to acquire a high-power voltage source with a high switching speed.

A photoconductive semiconductor switch (PCSS) made of semi-insulating gallium arsenide (SI-GaAs) was developed decades ago. However, it is still an active research topic because of its advantageous features, such as ultrafast switching speed, low-jitter response and delay, high repetition rate, high scalability to large operating voltages or currents, ability for optical control, and simple structure, which have led it to be widely used in a number of applications, including pulsed power systems, terahertz emitters, and high-speed electronics [37-40]. The abilities of various types of materials, including silicon, silicon carbide, gallium nitride, and hybrid nanocomposites, to further enhance the performance of light-controlled conductive switches have been explored [41-43].

Although the high stability and scalability of the low-bias linear switching of PCSS has been useful in some applications, such as high-speed switches, the high triggering energy required is not optimal. PCSS in a non-linear mode, however, requires much less triggering energy and features a faster turn-on time; in fact, the turn-on time can be faster than the rise time of the optical triggering pulse. In addition, non-linear PCSS has a unique lock-on phase with a lock-on time ranging from tens to hundreds of nanoseconds and a lock-on voltage determined by the material and dimensions of the switch [44]. Thus, it can be used to develop a very compact switch with an ultra-fast turn-on time, customized lock-on output, and low required triggering energy. However, an ultra-long lock-on time (i.e., on the order of milliseconds) can be even more advantageous for certain applications, such as a firing set switch [45]. Such a switch requires minimum ignition energy (for instance, igniting a propane–air mixture [46].) It usually takes several milliseconds to

accumulate enough ignition energy for the switch in a conduction state. Thus, a PCSS with long lock-on time (and thus low ignition power, low driving voltage, and compact size) is preferred as it provides enough time to achieve the minimum ignition energy.

To summarize, the studies in this dissertation aim to contribute to the field of laser beam steering, exploit the potential of KTN crystal, and develop new functionalities. The major accomplishments of this work are listed below:

- Developed and experimentally verified a non-uniform SCC model for KTN beam deflector (Chapter 3)

  (J.-H. Chao et al., *Proc. SPIE* **9958**, 99580S (2016) [47])

- Achieved a high-speed non-mechanical 2-D beam deflection on a single KTN deflector with space-charge-controlled (SCC) and temperature-gradient-controlled (TGC) deflection (Chapter 4)

  (J.-H. Chao et al., *Opt. Express* **25**(13), 15481–15492 (2017) [48])

- Designed and realized a ruby fluorescence-enabled ultra-long lock-on phase in high-gain gallium arsenic photoconductive semiconductor switch (PCSS) (Chapter 5)

  (J.-H. Chao et al., *Opt. Lett.* **43**(16), 3929–3932 (2018) [49])

Chapter 2

The Essentials of KTN Crystal

KTN crystal has attracted a significant amount of interest and has been widely used in a variety of applications since its discovery six decades ago. KTN has many spectacular physical properties because it is a solid solution of two perovskite materials, $KTaO_3$ and $KNbO_3$. One of its best-known features is its giant electro-optic (EO) effect, which has not been surpassed to this day. This chapter provides comprehensive information about KTN, including its structure, growth, various physical properties, and characteristics that are important to this research.

2.1 Structures, working phases, and preparation

2.1.1 Crystal structure of KTN

KTN crystal has a typical perovskite structure (i.e., a simple ABO_3 structure), as shown in Fig. 2-1. In this structure, the two cations, "A" and "B," are typically different sizes, with the larger one, "A," located in the corners of the cube (0,0,0) and "B" located at the center (1/2,1/2,1/2). The oxygen anion is bonded to both cations on each face of the cube (1/2,1/2,0). In the case of KTN, "A" is a potassium (K) atom, and "B" can be either a tantalum (Ta) or niobium (Nb) atom. However, the ideal cubic perovskite structure shown in Fig. 2-1 is not very common due to its strict size requirements for ions. Additionally, any temperature changes or stress can easily cause the structure to be distorted, reducing the level of crystal symmetry, which has a major impact on the physical properties of the material.

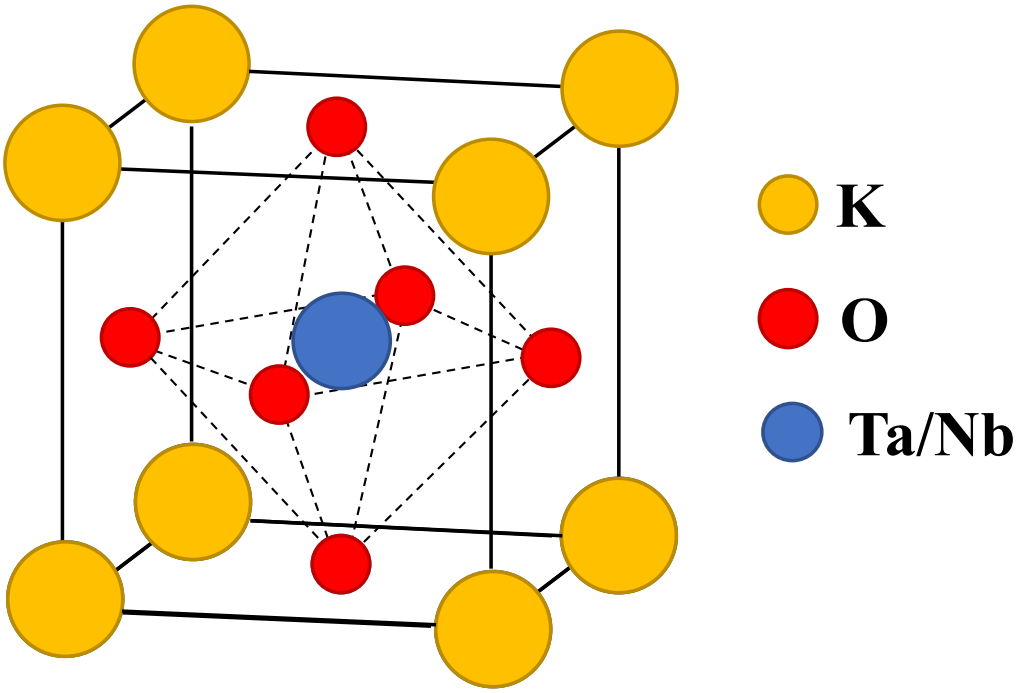

Figure **2-1**: Illustration of the structure of KTN crystal.

2.1.2 Working phases of KTN crystal

As a type of perovskite crystal, KTN crystal exhibits four crystal phases—cubic, tetragonal, orthorhombic, and rhombohedral—at different temperature ranges, depending on the concentration ratio of Ta and Nb atoms, as shown in Fig. 2-2 [50]. The solid lines in the figure represent the phase transition temperatures as a function of the concentration of Ta. In the cubic phase, KTN crystal is paraelectric and isotropic, and it exhibits both center symmetry and m3m point group symmetry. As the temperature lowers, nearing the point at which the crystal transitions to the tetragonal phase, the dielectric property of KTN crystal significantly increases, reaching its maximum at the edge of the phase transition temperature. This phenomenon led to the largest quadratic EO effect ever reported [25]. In the tetragonal phase, KTN crystal exhibits ferroelectricity and 4 mm point group symmetry. Because of the different Curie temperatures of $KTaO_3$ (Tc = 2–13 K) and $KNbO_3$ (Tc = 698–700 K), the transition temperature, T_C, between the cubic and tetragonal phase has a linear relationship with the concentration ratio of Ta. It can be expressed as follows [50, 51]:

$$T_C = 676x - 241\ ℃, \tag{2.1}$$

where x is the mol ratio of Nb atoms to the total number of Nb and Ta atoms. Based on this equation, the phase transition temperatures of KTN crystal can be altered by controlling the concentration ratio of Nb and Ta during crystal growth.

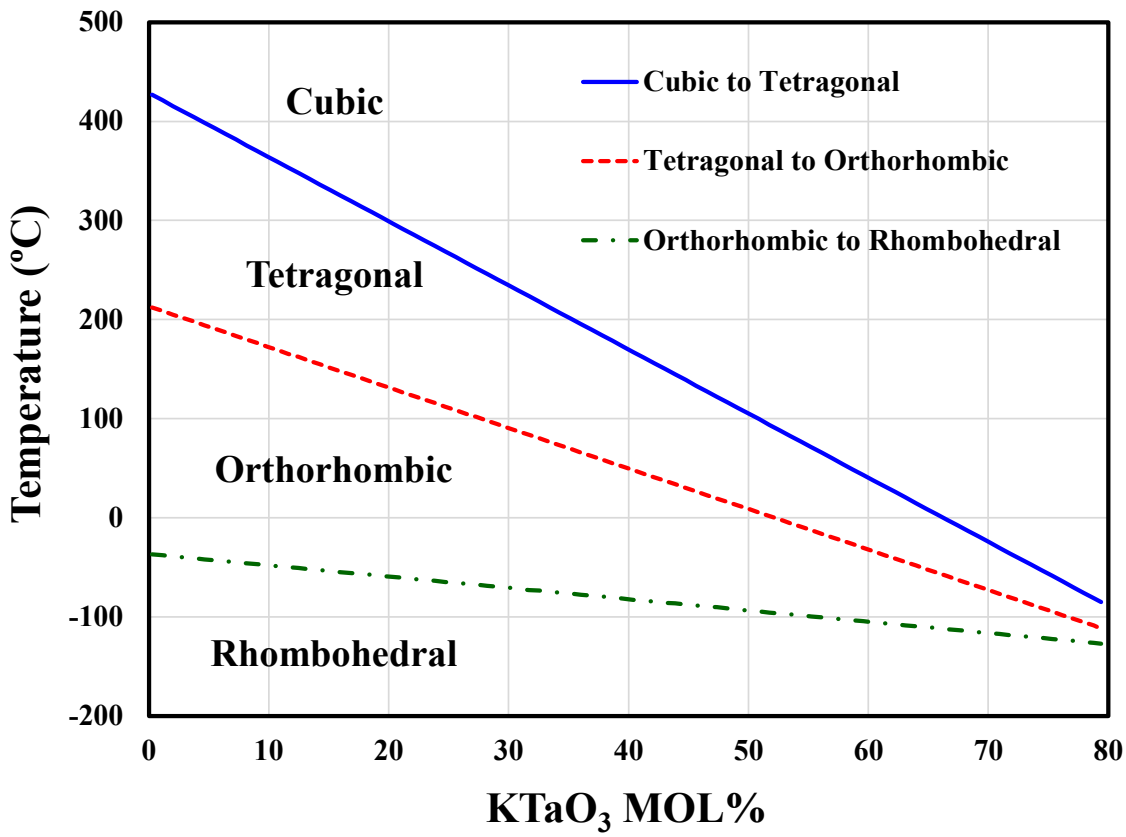

Figure **2-2**: Diagram of the crystal phase transition temperatures with respect to the concentration ratio of $KTaO_3$ of a $KTa_xNb_{1-x}O_3$ crystal. Data points were extracted from Ref. [51].

2.1.3 Preparation of KTN crystal

As it is a solid solution of two perovskite materials—$KTaO_3$ and $KNbO_3$—with very similar lattice constants (KTaO3: a_0 = 4.0026 Å; $KNbO_3$: a_0 = 4.0226 Å) but different Curie temperatures ($KTaO_3$: T_c = 2–13 K; $KNbO_3$: T_c = 698–700 K), it has always been challenging to grow KTN crystal [52, 53]. The first KTN single crystal was grown by Triebwasser in 1959 using the Kyropoulos process [53, 54], which was the most advanced technique at the time for growing large single crystals. Since this work, the superior EO properties of KTN have attracted much attention, leading to its application in, for instance, switches, modulators, and deflectors. However,

the first-generation KTN single crystal suffered from an insufficient size and an overly low working T_C due to complications during the growth process. In an attempt to improve the size and quality of the crystal, an improved top-seeded solution growth (TSSG) technique was used [55–58]. However, it was still difficult to maintain stable KTN crystal growth during the process, causing the crystal to have too many defects to function. Researchers made continuous efforts to overcome this problem in the following decades. In 2008, using a state-of-the-art TSSG technique, a high-quality, sizeable KTN single crystal with an adjustable composition ratio was successfully grown by a Japanese research group from NTT. Specifically, they reported successfully growing a bulk KTN single crystal with a size of 40 mm × 40 mm × 20 mm [21, 59]. Soon after the study was published, KTN crystal became commercially available. Many attempts were made to grow KTN in thin films using liquid phase epitaxy (LPE) [59,60], RF sputtering [60, 61], chemical solution deposition (CSD) [62, 63], sol-gel method [64, 65], metal-organic chemical vapor deposition (MOCVD) [66, 67], and pulse laser deposition (PLD) [68, 69]. KTN films could be used in a variety of applications, such as waveguides [59], pyroelectric detectors [70], optical fibers [71], semiconductor processes [69], or microwave devices [68].

2.2 Physical properties of KTN crystal

The physical properties of KTN crystal depend to a large extent on the concentration ratio of $KTaO_3$ and $KNbO_3$. In addition, its working phases vary. Table 2-1 lists the basic physical properties of KTN crystal, including its thermal and mechanical properties, and the concentration ratio and working phase in which the properties were observed.

Table **2-1**: Physical properties of $KTa_{1-x}Nb_xO_3$ crystals [57, 72–75]

Properties	Tetragonal phase	Cubic phase	Ratio (x)
Lattice constant (Å)	3.9970	3.9941	0.37
Melting point (K)	1536.90		0.33
	1520.31		0.37
Density (g/cm^3)	6.235		0.33
	6.180		0.37
Elastic stiffness coefficient (GPa)	c_{11} = 424.8295 c_{33} = 121.3778 c_{44} = 82.8600 c_{12} = 68.0517 c_{13} = 80.7003 c_{66} = 93.6141	c_{11} = 489.0866 c_{33} = 472.4396 c_{44} = 87.9732 c_{12} = 65.1750 c_{13} = 64.7585 c_{66} = 84.1298	0.50
Bulk modulus (GPa)	135.62	204.58	0.50
Shear modulus (GPa)	91.79	124.12	0.50
Young's modulus (GPa)	224.689	309.79	0.50
Thermal expansion (K^{-1})	6.4×10^{-6}		0.33
	6.6×10^{-6}		0.37
Specific heat (J/g-K)	0.421		0.33
	0.430		0.37

Thermal conductivity (W/m-K)	8.551	0.33
	5.592	0.37
Thermal diffusion coefficient (mm^2/s)	2.132	0.33
	1.689	0.37
Resistivity (Ω-cm)	5×10^{11}	0.37
	2×10^{8}	0.40

2.2.1 Optical properties

KTN single crystal is a colorless and optically transparent material with a broad transmission window. Figure 2-3 shows a sample of double-side polished KTN single crystal sized 10 mm × 10 mm × 1 mm.

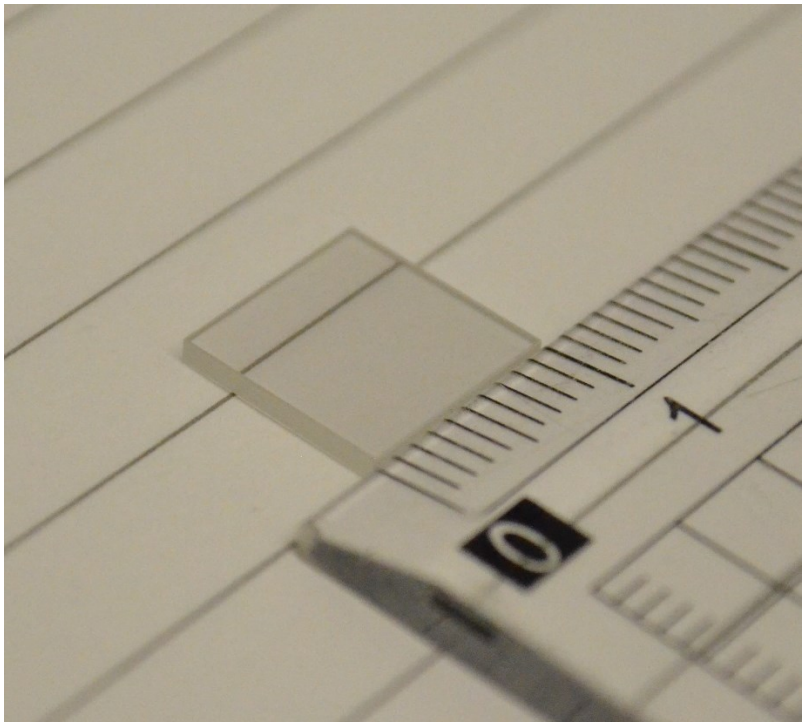

Figure **2-3**: Double-side polished KTN crystal sized 10 mm × 10 mm × 1 mm.

The optical bandgap of KTN crystal is approximately 3.1 eV, which corresponds to the absorption edge at a wavelength of 0.4 μm. The transmittance window of KTN was found to be between 0.4 and ~4 μm according to both UV-VIS and FTIR spectrometers, as shown in Fig. 2-4.

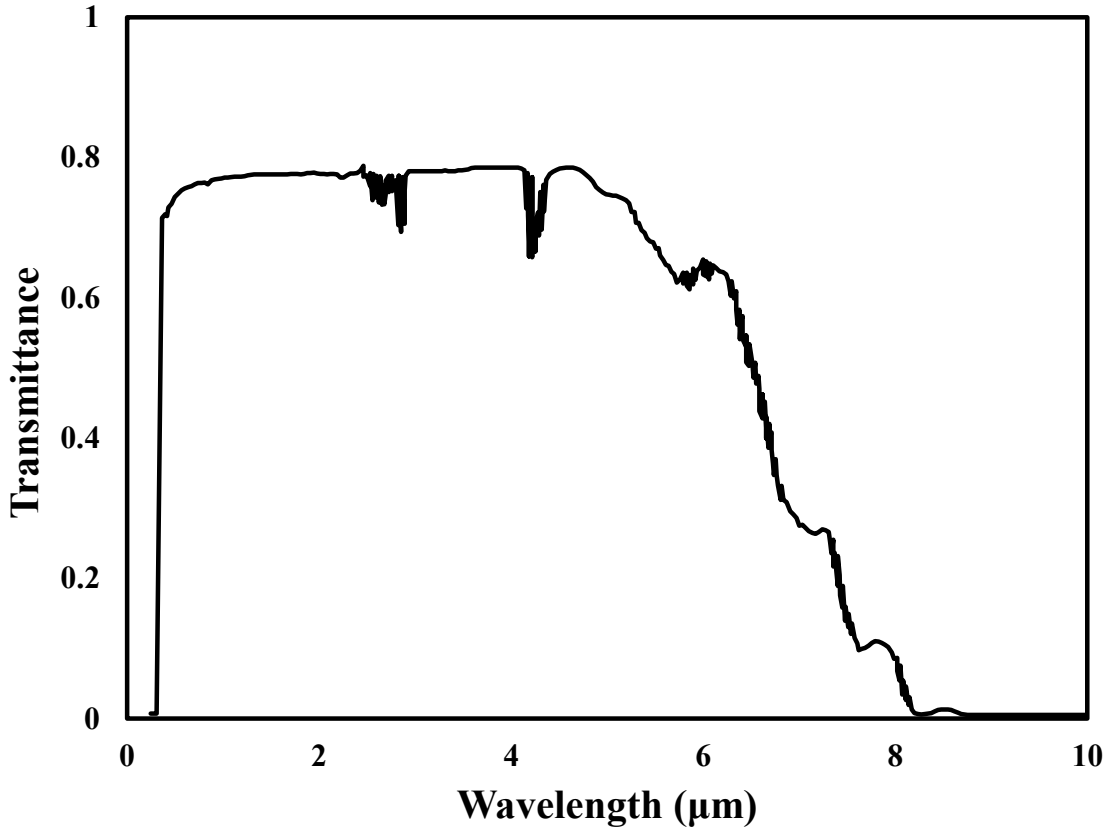

Figure **2-4**: Measured transmittance of a $KTa_{0.7}Nb_{0.3}O_3$ crystal corresponding to a spectrum of 0.25–10 μm. Data points were extracted from Ref. [76].

The refractive index of cubic-phase KTN was found to follow a dispersion equation known as the single-term Sellmeiser formula:

$$n_0^2 - 1 = \frac{3.7994}{\left[1-\left(\frac{\lambda_S}{\lambda}\right)^2\right]}, \tag{2.2}$$

where λ_S = 0.2012 μm. This dispersion relationship is shown in Fig. 2-5.

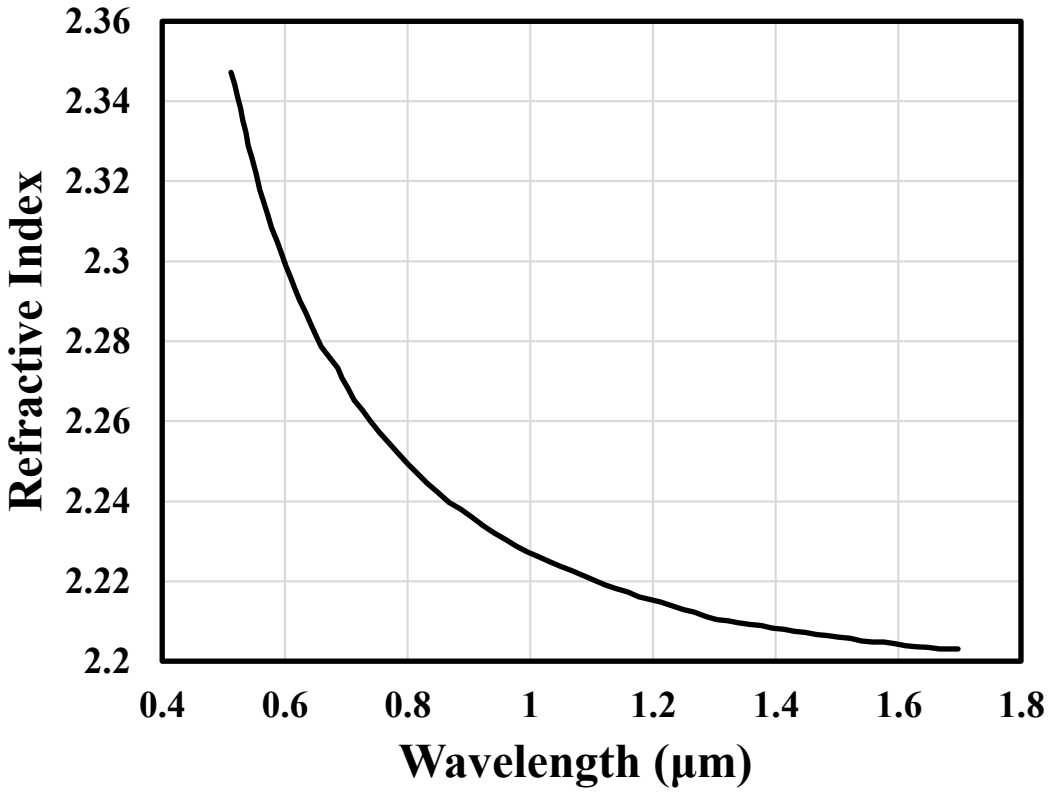

Figure **2-5**: Dispersion relationship between the refractive index and wavelength of a $KTa_{0.63}Nb_{0.37}O_3$ crystal. Data points were extracted from Ref. [77].

2.2.2 Dielectric properties

KTN crystal exhibits quite peculiar dielectric properties due to its composition and crystal structure. As a solid solution of $KNbO_3$ and $KTaO_3$, the physical properties of KTN depend on the composition ratio of these two materials. In addition, the physical properties of numerous materials with a perovskite crystal structure, including KTN, have peculiar temperature dependence. For example, the relative permittivity of KTN was found to sharply rise near its phase transition temperatures. Fig. 2-6 shows the temperature dependency of the relative permittivity of KTN crystal. The three spikes in relative permittivity correspond to the three phase transition

temperatures between the four working phases of perovskite crystal. In a phenomenon known as thermal hysteresis, temperature dependency differs in heating and cooling processes. This will be discussed further in Section 2-3.

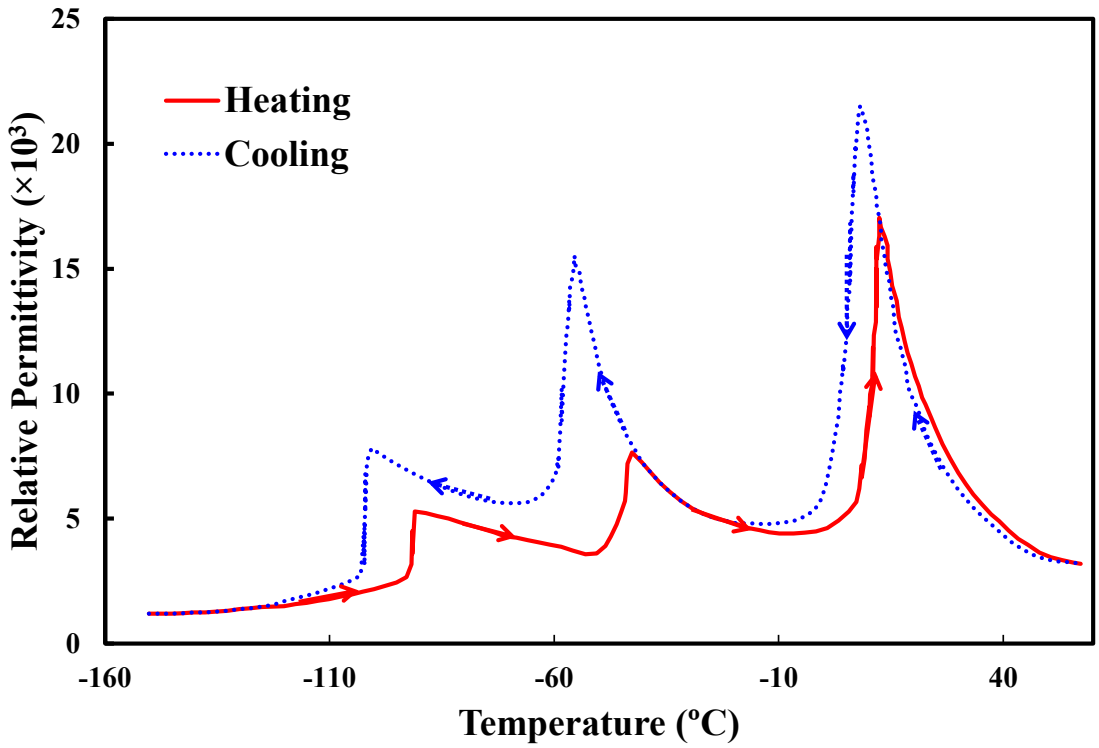

Figure **2-6**: Relative permittivity and temperature dependency of $KTa_{0.63}Nb_{0.37}O_3$ crystal. Data points were extracted from [78].

The temperature dependency of the relative permittivity, , of cubic-phase KTN follows the Curie-Wiess Law, which is expressed as follows:

$$\varepsilon_r \propto \frac{1}{T - T_c}, \tag{2.3}$$

where T is the temperature and T_c is the Curie temperature of the crystal.

2.2.3 Electro-optical properties

The EO properties of KTN crystal are a core feature of KTN on which this study is based. Prior studies have reported that KTN has a spectacular EO effect. As an EO crystal, the optical dielectric impermeability tensor, η_{ij}, of KTN depends on the distribution of charges in the crystal. When an electric field is applied to it, the E-field forces redistribution of the bond charges and slight deformation of the ion lattice in the crystal, resulting a net change in the optical dielectric impermeability tensor. This change is defined by the following equation:

$$\eta_{ij}(E) - \eta_{ij}(0) \equiv \Delta\eta_{ij} = f_{ijk}P_k + g_{ijkl}P_kP_l \,, \tag{2.4}$$

where E is the electric field, P is the electric polarization, and f_{ijk} and g_{ijkl} represent the linear and quadratic EO coefficients, respectively. Also, P and E are related by the permittivity tensor, ε_{ij}, as follows:

$$P = \left(\varepsilon_{ij} - \varepsilon_0\right)E \,. \tag{2.5}$$

Thus, Eq. (2.4) can also be expressed as follows:

$$\Delta\eta_{ij} = r_{ijk}P_k + s_{ijkl}P_kP_l \,, \tag{2.6}$$

with

$$f_{ijk} = \frac{r_{ijk}}{\varepsilon_k - \varepsilon_0} \,, \tag{2.7}$$

$$g_{ijkl} = \frac{s_{ijkl}}{(\varepsilon_k - \varepsilon_0)(\varepsilon_l - \varepsilon_0)} \,. \tag{2.8}$$

As formerly mentioned, tetragonal-phase KTN crystal is ferroelectric with 4 mm point group symmetry. The EO effect in this phase is dominated by the Pockels effect, causing the quadratic EO coefficient to typically be negligible under an external E-field. Therefore, the EO coefficient is given by the Pockels coefficient, which can be expressed in a tensor form as follows:

$$r_{ij} = \begin{pmatrix} 0 & 0 & r_{13} \\ 0 & 0 & r_{13} \\ 0 & 0 & r_{33} \\ 0 & r_{51} & 0 \\ r_{51} & 0 & 0 \\ 0 & 0 & 0 \end{pmatrix}. \tag{2.9}$$

Note that $r_{13} = r_{23}$ and $r_{42} = r_{51}$ in the above tensor due to the type of symmetry exhibited by ferroelectric KTN. Because r_{13} was found to be quite smaller than and difficult to be separated from r_{33} [79], an effective linear EO coefficient, r_c, is defined as follows:

$$r_c = r_{33} - \left(\frac{n_a}{n_c}\right)^3 r_{13}\,, \tag{2.10}$$

where n_c and n_a represent the refractive index along the polar c-axis and the index on its orthogonal plane, respectively. Both r_c and r_{51} are used to characterize the linear EO effect of ferroelectric KTN. The temperature dependencies of these two coefficients were reported by Raalte [79] and are shown in Fig. 2-7. Later, r_{33} was reported by Loheide et al. [80]. The linear EO effect in ferroelectric KTN was found to be much larger compared to other commonly used EO crystals; the half-wave voltage of linear EO modulation in KTN is approximately half of that in $BaTiO_2$, one tenth of that in $LiNbO_3$, and a mere one hundredth of that in KDP-based EO modulators.

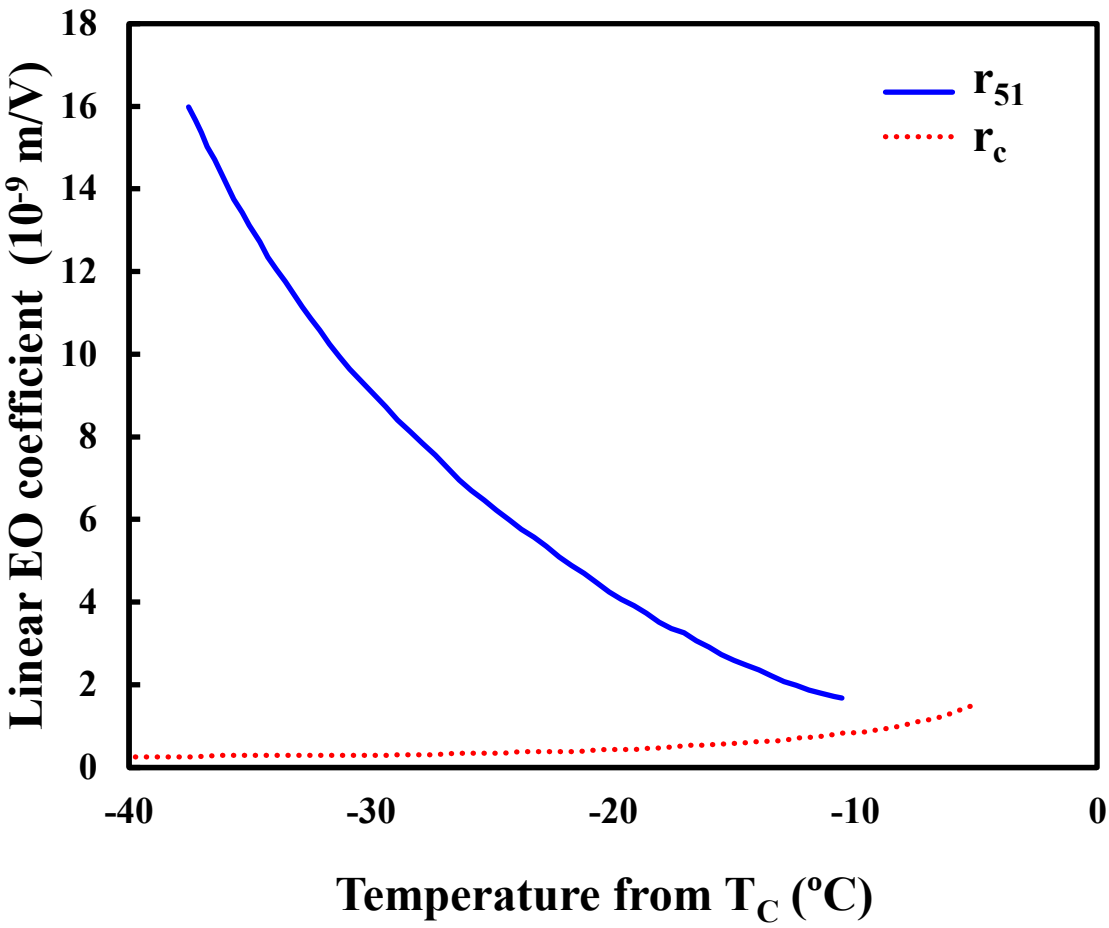

Figure **2-7**: Temperature dependence of the linear EO coefficients, r_c and r_{51}. Data were extracted from [79].

When the temperature of KTN crystal is above its Curie temperature, the crystal exhibits cubic m3m point group symmetry. As a result, the linear EO effect no longer exists when an external E-field is applied to the crystal. Therefore, the quadratic EO effect (i.e., the Kerr effect) becomes dominant in this phase. The quadratic EO coefficient, s_{ij}, in the tensor form can be written in a tensor form as follows:

$$s_{ij} = \begin{pmatrix} s_{11} & s_{12} & s_{12} & 0 & 0 & 0 \\ s_{12} & s_{11} & s_{12} & 0 & 0 & 0 \\ s_{12} & s_{12} & s_{11} & 0 & 0 & 0 \\ 0 & 0 & 0 & s_{44} & 0 & 0 \\ 0 & 0 & 0 & 0 & s_{44} & 0 \\ 0 & 0 & 0 & 0 & 0 & s_{44} \end{pmatrix}. \tag{2.11}$$

Many of the entries are either vanished or shown as their equals due to the crystal symmetry. Measurements of , , and have been reported over the past few decades and are listed in Table 2-2.

Table **2-2**: Kerr coefficients of cubic KTN crystal reported in prior studies.

Composition of KTN	Kerr coefficient*	Reference
$KTa_{0.65}Nb_{0.35}O_3$	$g_{11} = 0.136$ $g_{12} = -0.03$ $g_{11} - g_{12} = 0.174$ $g_{44} = 0.147$	[72]
$KTa_{0.65}Nb_{0.35}O_3$	$g_{11} - g_{12} = 0.140$ $g_{44} = 0.135$	[81]
$KTa_{0.65}Nb_{0.35}O_3$	$g_{11} - g_{12} = 0.217$ $g_{44} = 0.167$	[78]
$KTa_{0.65}Nb_{0.35}O_3$	$s_{11} = 3.0$ $s_{12} = -1.8$ $s_{11} - s_{12} = 4.8$	[82]
$KTa_{0.65}Nb_{0.35}O_3$	$s_{12} = -1.5$	[83]
$KTa_{0.59}Nb_{0.41}O_3$	$s_{11} = 22.4$	[33]

* The units of g_{ij} are m^4/C^2 and $s_{ij} \times 10^{-15}$ m^2/V^2.

Like other physical properties of KTN, the Kerr coefficient is very much dependent upon the temperature near the Curie point, T_C. The temperature dependence of the quadratic EO coefficients of a $KTa_{0.59}Nb_{0.41}O_3$ crystal was reported by Nakamura et al. [33]and is shown in Fig. 2-8.

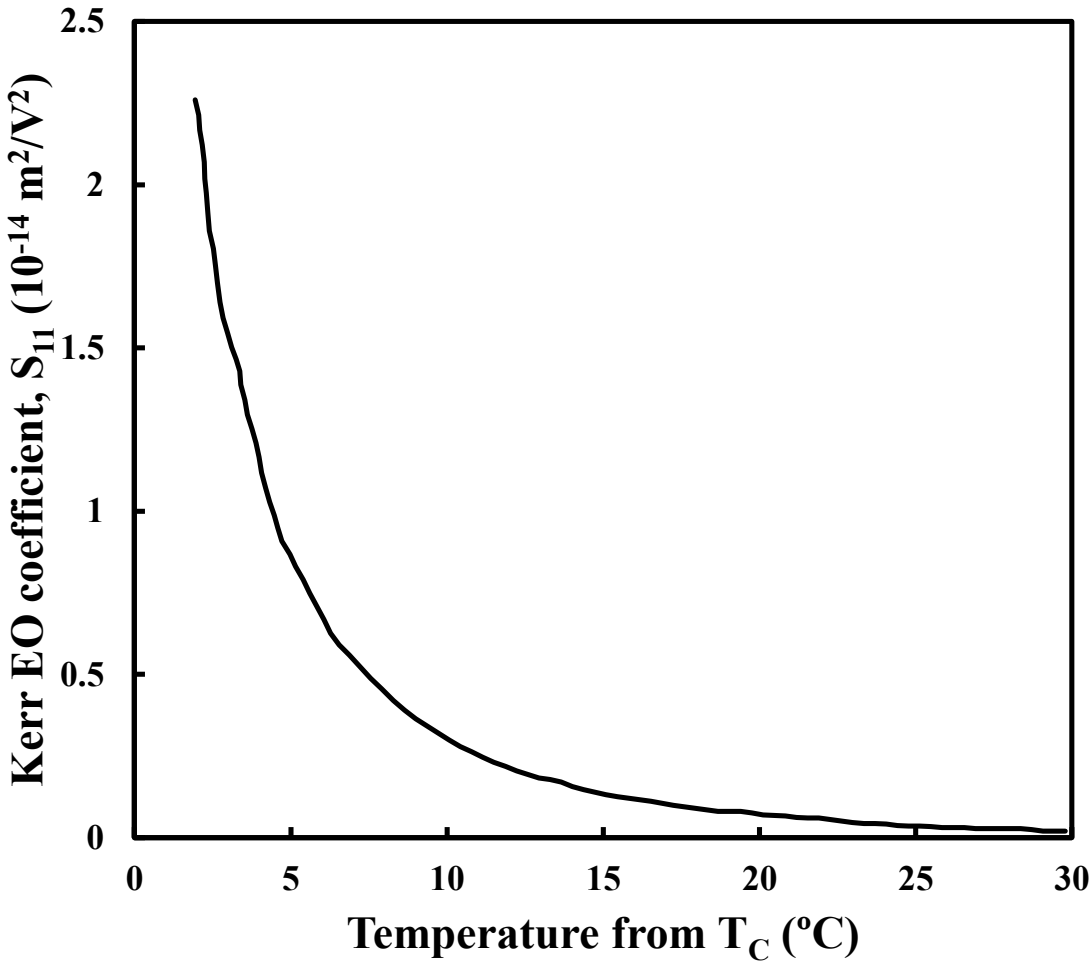

Figure **2-8**: Temperature dependence of the quadratic EO coefficients of a $KTa_{0.59}Nb_{0.41}O_3$ crystal with T_C = 35 ºC. Data were extracted from [33].

2.3 Thermal hysteresis of KTN

The term *thermal hysteresis* refers to the phenomenon in which the properties of a material behave differently during the processes of heating and cooling. It is common in materials with an ABO_3 perovskite structure. For example, it was found that the evolution of the relative permittivity of KTN crystal with respect to temperature during a heating process is very different from that during a cooling process [78], as illustrated in Fig. 2-9.

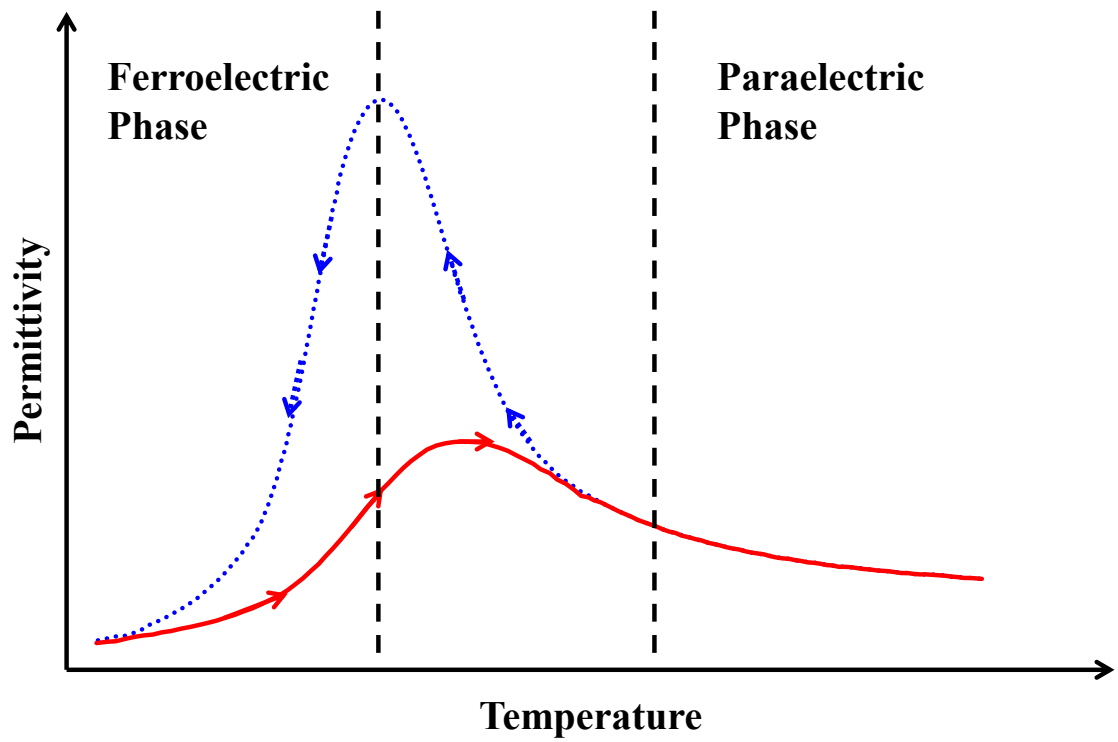

Figure **2-9**: Conceptual illustration of the temperature dependence of permittivity in KTN crystal.

Moreover, it was found that this behavior differs with respect to the rate at which the temperature changes. For example, Chang et al. [25] showed that the EO coefficient of KTN with respect to temperature differs at different cooling rates (see Fig. 2-10) and that the coefficient was greatly enhanced by super-cooling; at a cooling rate of 0.45 ºC/s, the highest in their study, they

measured an EO coefficient of 6.94 $\times 10^{-14} m^2/v^2$, which is the highest quadratic EO coefficient to ever be reported.

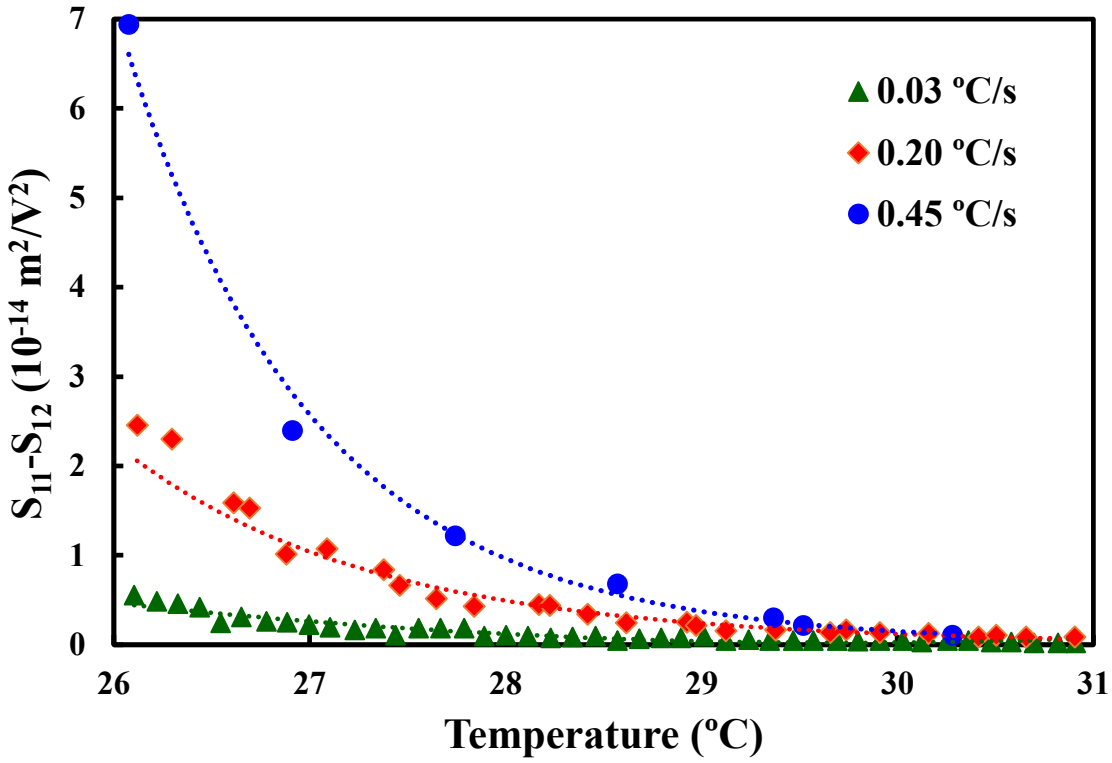

Figure **2-10**: Temperature dependence of the quadratic EO coefficients of $KTa_{0.6}Nb_{0.4}O_3$ at different cooling rates. Data points were extracted from Ref. [25].

2.4 Field-induced phase transition

The phenomenon of field-induced phase transition was observed in $K_{0.95}Li_{0.05}Ta_{0.73}Nb_{0.27}O_3$ (KLTN) by Imai et al. [84]. They found that KLTN crystal behaves as it does in its ferroelectric phase when an external electric field was applied at a temperature above the Curie temperature, which should cause the crystal to be in its paraelectric phase. It was also found that such a phase transition event would be more vigorous at a temperature closer to the Curie point of the crystal and in the presence of a higher electric field. However, above a certain temperature (the so-called critical end point), the crystal is no longer affected by the electric field. This peculiar phenomenon was also observed in KTN by Zhu et al. in 2016 [85].

It was believed that the perovskite crystal structure of KTN plays a major role in phase transitioning behavior. In a perovskite KTN cell, eight potassium (K) atoms are located at each corner of the cubic cell and six oxygen (O) atoms are positioned at the center of each face of the cube, with either a niobium (Nb) or tantalum (Ta) atom at the center of the cell, as shown in Fig, 2-1. When the crystal is in a cubic phase and the temperature is well above the Curie point, the niobium ions randomly deviate from the center of the cell, generating dipoles. All the dipoles are randomly aligned at this temperature, and hence the total sum of the polarization is zero. As the temperature lowers, nearing the Curie point, the random dipole movement becomes weaker. Also, localized polar nanoregions (PNRs) start to appear due to interactions among adjacent dipoles [86]. When the temperature is below the Curie point and the crystal is in its ferroelectric phase, the dipoles become aligned in a certain direction, generating polarization.

In the case of field-induced phase transition, the PNRs in the crystal are aligned along the direction of the biasing field, which generates polarization in the crystal, as if it were in its ferroelectric phase.

Chapter 3

Non-Uniform SCC Laser Beam Deflection

Currently, space-charge-controlled (SCC) KTN beam deflectors are based on a model of uniform charge distribution. However, non-uniform space-charge-controlled (SCC) beam deflection was proposed after a recent study [36] found non-uniform space charge distribution in KTN crystal. This chapter extensively studies non-uniform charge distribution in SCC KTN beam deflectors.

High-speed optical beam deflectors are widely employed in many applications, including laser displays [2], high speed beam scanners [3], switchable waveguides [4], low-coherence optical tomography [1], and spectral multiplexed holograms [5]. Among all sorts of beam deflectors, EO deflectors have not only rapid switching speed but also great precision control. Of the various EO materials, KTN has the greatest EO coefficient ever reported [72, 86] and thus has immense potential in the development of ultra-fast beam deflectors. One study developed an SCC KTN beam deflector with a simple configuration [87], in which beams are deflected by an electric-field-dependent prism-shaped refractive index distribution inside the KTN crystal, which is formed by injected electrons when an external field is applied to the crystal. Because the refractive index distribution is dependent on the applied voltage field through the quadratic EO effect, the speed of beam deflection is essentially determined by the switching speed of the external source, and thus, in theory, could be at the nanosecond scale. The fastest KTN beam scanner reported to date has a speed of around 700 kHz [88]. To maximize the relative permittivity of KTN crystal, beam deflectors are generally operated in their cubic phase slightly above the Curie temperature.

The behavior of charges inside KTN crystal depends strongly on the operating temperature [84]. Recent investigations have indicated that electric-field-induced phase transition usually

occurs under a high bias field and causes the phase transition temperature to rise [85]. This field-induced phase transition could affect the speed of KTN beam deflectors [25], as could non-uniform charge distribution. Thus, in this study, we perform a quantitative analysis of a non-uniform SCC KTN beam deflector.

3.1 Uniform SCC KTN beam deflector

Beam deflection occurs in SCC KTN crystal by harnessing the effect of a pre-injected charge in the crystal under an electrical bias. The deflector is a simple structure usually involving a KTN crystal located between two metallic layers, which serve as electrodes. To enable charge injection, titanium is chosen for the electrodes so that electrons can drift across the Schottky barrier between the crystal and metal and be injected into the crystal when an external bias is applied to the deflector. Under the influence of the external bias, those injected electrons are driven toward the opposite side of the electrode. The electric field distribution inside the crystal is altered as the electrons are injected into the crystal, inducing a change in the refractive index of the crystal, which in turn influences the input laser beam, causing beam deflection. However, deflection induced merely by injected charges is relatively slow, taking up to seconds [33].

A revised method of charge injection was proposed by Miyazu et al. [34]. They determined that a portion of the injected electrons were trapped inside the crystal due to defects that formed when the crystal was growing. These charges could remain trapped for many hours if they were not rapidly released by either changing the temperature or performing excitation with an external light source. Importantly, these trapped charges play a key role in high-speed beam deflection. Assuming that the trapped electrons are uniformly distributed in density N, according to Gauss's law, the overall electric field distribution inside the crystal when applying external bias would be as follows [34]:

$$E(x) = -\frac{eN}{\varepsilon}\left(x - \frac{d}{2} + \frac{\varepsilon V}{eNd}\right), \tag{3.1}$$

where e is the electric charge, ϵ is the permittivity of the crystal, d is the gap between electrodes and V is the applied voltage. The change in refractive index due to the Kerr effect is given by the following equation:

$$\Delta n(x) = -\frac{1}{2} n^3 g_{11} \varepsilon^2 E(x)^2$$

$$= -\frac{1}{2} n^3 g_{11} e^2 N^2 \left(x - \frac{d}{2} + \frac{\varepsilon V}{eNd} \right)^2, \tag{3.2}$$

where n is the refractive index and g_{11} is the EO coefficient of the crystal in polar form when the polarization of the beam is parallel to the applied electric field. The deflection angle can therefore be given by the following equation:

$$\theta(x) = L \frac{d}{dx} \Delta n(x)$$

$$= -n^3 g_{11} e^2 N^2 L \left(x - \frac{d}{2} + \frac{\varepsilon V}{eNd} \right). \tag{3.3}$$

where L is the propagation length of the beam in the crystal. Near the center of the electrode, the divergence angle of p (the polarization of light in parallel to the applied electric field) and s (the polarization of light perpendicular to the applied electric field) are given by the following equations:

$$\theta_p(\frac{d}{2}) = -n^3 g_{11} \rho(x) L \varepsilon_0 \varepsilon_r \frac{V}{d}. \tag{3.4}$$

$$\theta_s(\frac{d}{2}) = -n^3 g_{12} \rho(x) L \varepsilon_0 \varepsilon_r \frac{V}{d}. \tag{3.5}$$

where g_{11} and g_{12} are the EO coefficients in terms of polarization for the p and s polarized light beams, respectively; $\rho(x)$ is the pre-injected space charge density, which is a constant in cases of uniform charge distribution; and ϵ_0 and ϵ_r are the vacuum permittivity and relative permittivity of

KTN crystal, respectively. Fig. 3-1 shows the configuration of a pre-injected SCC KTN beam deflector.

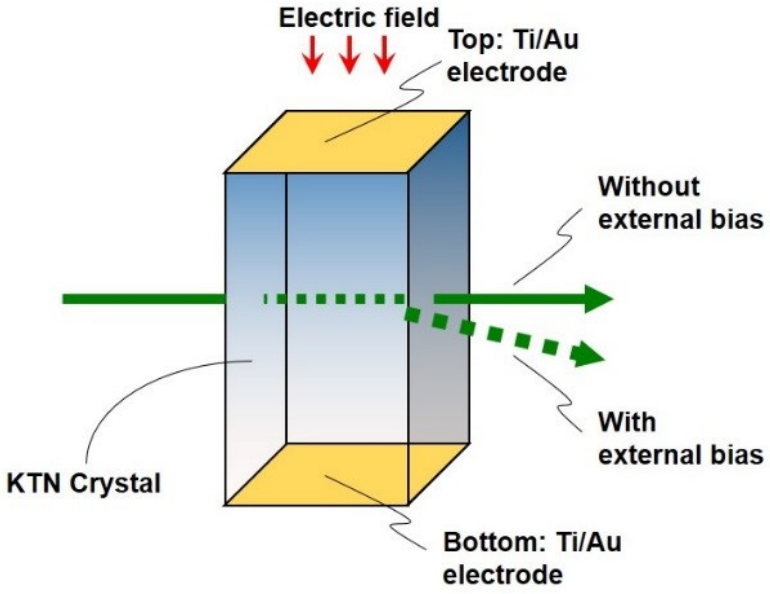

Figure **3-1**: Illustration of the configuration of an SCC KTN beam deflector.

3.2 Non-uniform SCC KTN beam deflector

Recently, Imai et al. investigated in depth the charge distribution inside KTN crystal under external bias, finding that the injected charges could have non-uniform distribution [36]. Furthermore, they found that the final penetration depth of the injected charge did not change with time, but with the applied bias field; the higher the bias field, the deeper the penetration. Thus, it is necessary to study the beam deflection effect in the context of a non-uniform space charge distribution.

When a KTN crystal is applied with an external biasing field, the charges would be injected into the crystal due to similar work functions between the KTN crystal and the titanium electrode. Part of the injected charges would be trapped by the defect states in the crystal, forming a non-uniform space charge distribution. To obtain the electric field distribution for a non-uniform injected charge, we divide the crystal into multiple sections, 1, 2, and 3, along the direction of the electrodes, x, by different depths to the cathode, d_1, d_2, and d_3, respectively, as shown in Fig. 3-2. The charge densities for each sections 1, 2, and 3 are ρ_1, ρ_2, and ρ_3, respectively. Since the charges are injected into the crystal from the cathode, typically $\rho_1 > \rho_2 > \rho_3$. To simplify the discussion, we assume that C_1 and C_2 are arbitrary constants that can be determined based on the boundary conditions and the applied voltage. Therefore, the total electric field provided on the crystal can be distributed according to the fixed charges from these sections.

When $0 \leq x \leq d_1$, from gauss's law,

$$\rho_1 = \varepsilon \frac{dE(x)}{dx} . \tag{3.6}$$

Therefore,

$$\Delta E(x) = \frac{\rho_1}{\varepsilon} x . \tag{3.7}$$

When $d_1 \leq x \leq d_2$,

$$\Delta E(x) = \frac{\rho_2}{\varepsilon} x + C_1 . \tag{3.8}$$

When $d_2 \leq x \leq d_3$,

$$\Delta E(x) = \frac{\rho_3}{\varepsilon} x + C_2 . \tag{3.9}$$

When $x = d_1$,

$$\frac{\rho_1}{\varepsilon} d_1 = \frac{\rho_2}{\varepsilon} d_1 + C_1$$

$$C_1 = \frac{(\rho_1 - \rho_2)}{\varepsilon} d_1 . \tag{3.10}$$

When $x = d_2$,

$$\frac{\rho_2}{\varepsilon} d_2 + C_1 = \frac{\rho_3}{\varepsilon} d_2 + C_2$$

$$C_2 = \frac{(\rho_2 - \rho_3)}{\varepsilon} d_2 + C_1 = \frac{(\rho_2 - \rho_3)}{\varepsilon} d_2 + \frac{(\rho_1 - \rho_2)}{\varepsilon} d_1 . \tag{3.11}$$

Eqs. (3.10) and (3.11) can be used to determine the arbitrary constants C_1 and C_2. Substituting C_1 and C_2 in Eqs. (3.7)–(3.9) enables identification of the electric field in each section. Then, the electric-field-induced refractive index change in each section can be obtained by applying the relationship $\Delta n(x) = -\frac{1}{2} n^3 g_{11} \epsilon^2 \, \Delta \, E(x)^2$. Furthermore, the deflection angle of each section can be derived by applying the relationship $\theta(x) = L \frac{d}{dx} \Delta n(x)$.

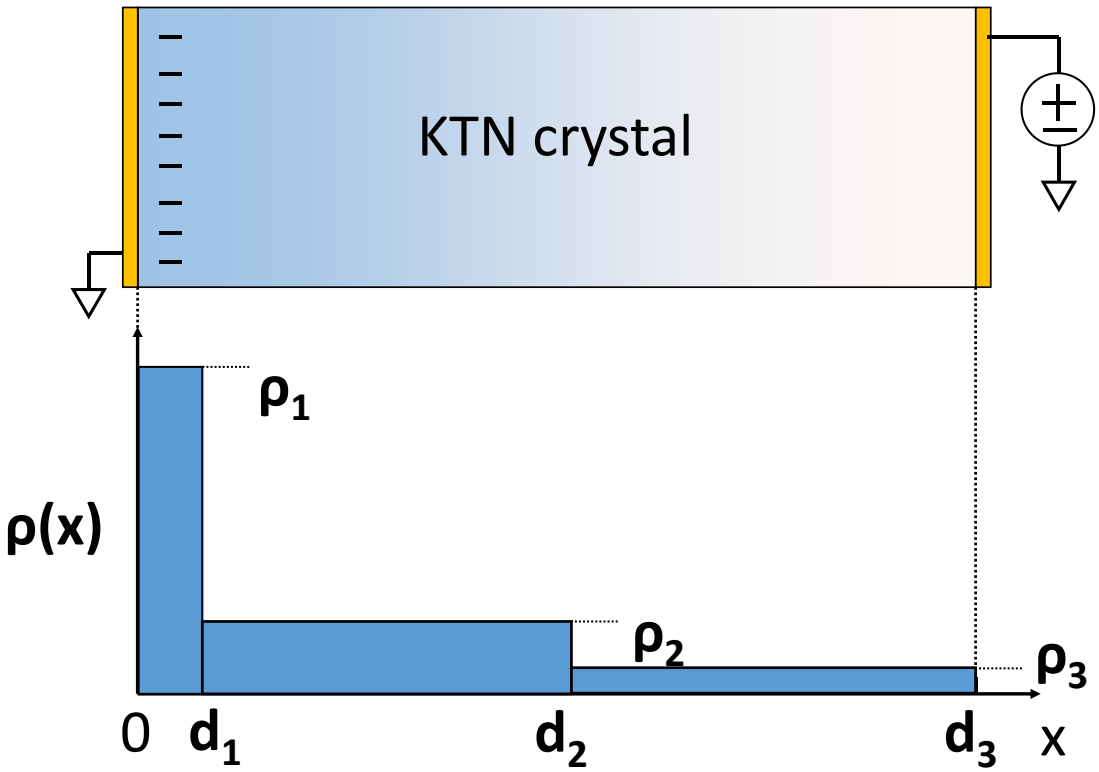

Figure **3-2**: Illustration of non-uniform charge injection in KTN crystal.

Figs. 3-3(a), (b), and (c) show the profiles calculated for the electric field distribution, refractive index gradient, and deflection angle, respectively inside the crystal. For calculation, we use the following parameters: d_1= 0.1 mm, d_2=1 mm, d_3=2 mm, $\rho_1 = -200\ C \times m^{-3}$, $\rho_2 = -50\ C \times m^{-3}$, and $\rho_3 = -5\ C \times m^{-3}$, with an applied voltage of 500V. Furthermore, the calculation was done by assuming a zero electric field occurring at the cathode in order to simplify the discussion.

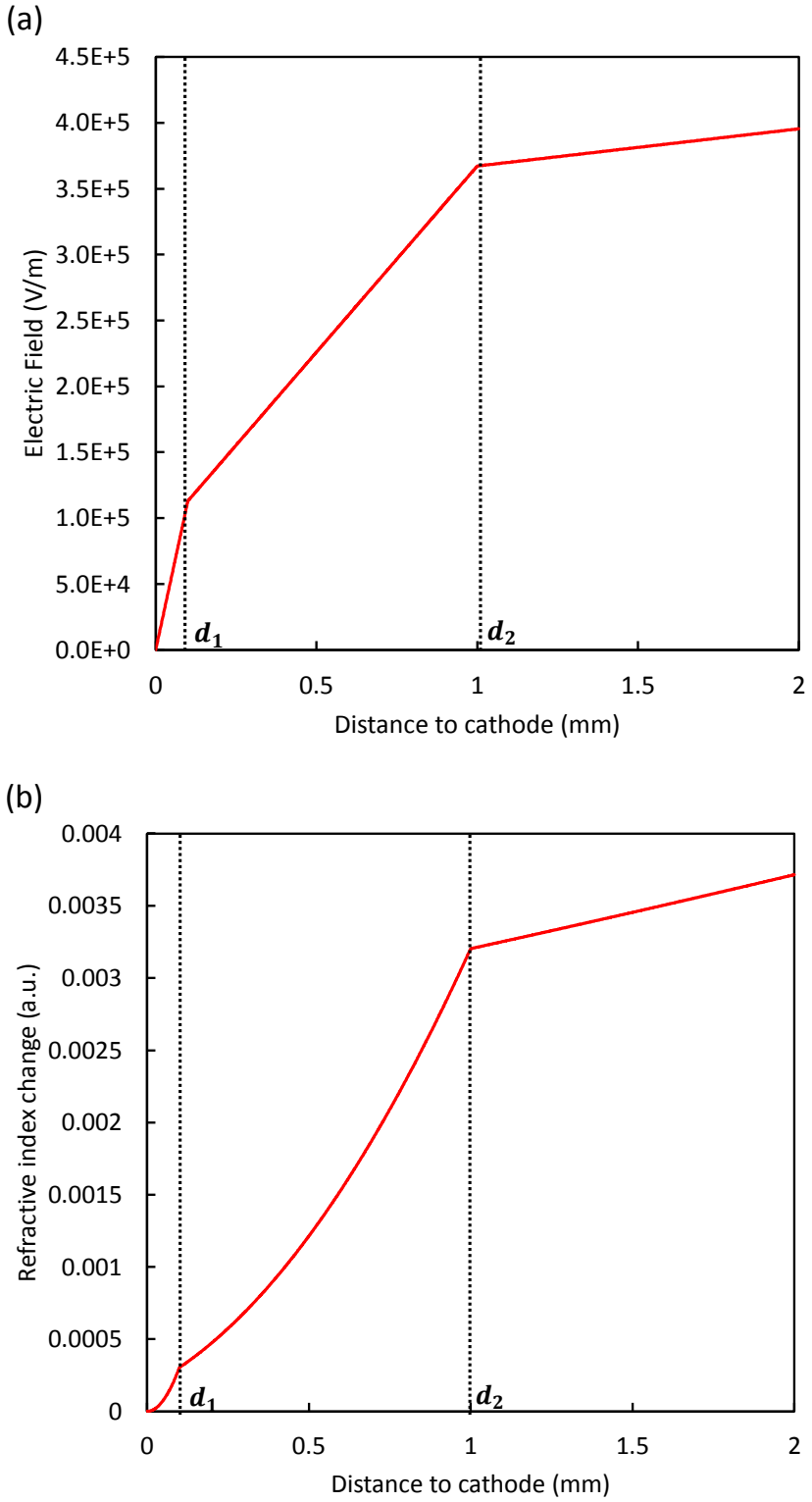
(a)
4.5E+5
4.0E+5
3.5E+5
3.0E+5
2.5E+5
2.0E+5
1.5E+5
1.0E+5
5.0E+4
0.0E+0
Electric Field (V/m)
d_1
d_2
0
0.5
1
1.5
2
Distance to cathode (mm)
(b)
0.004
0.0035
0.003
0.0025
0.002
0.0015
0.001
0.0005
0
Refractive index change (a.u.)
d_1
d_2
0
0.5
1
1.5
2
Distance to cathode (mm)

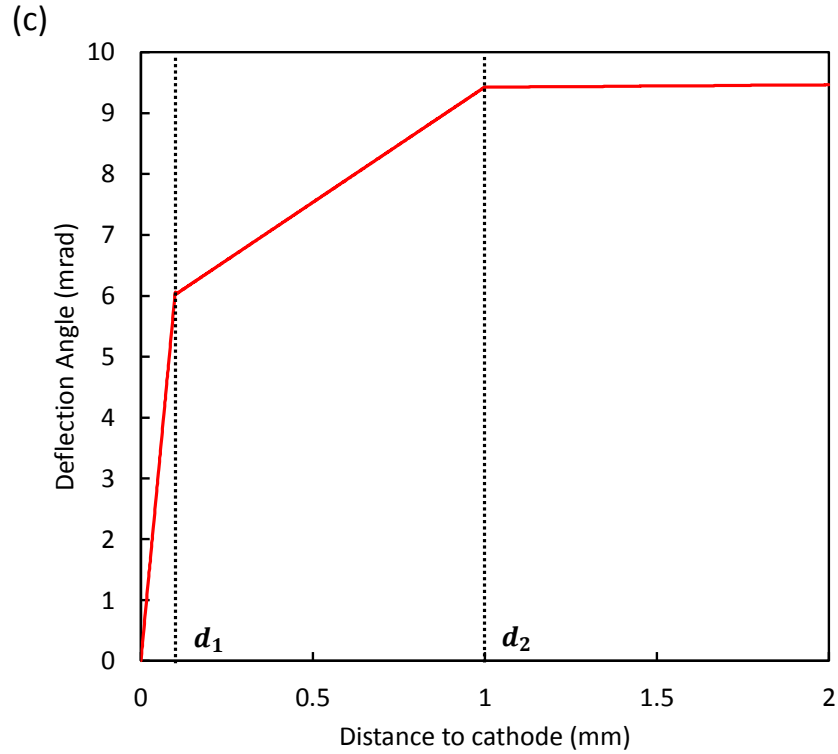

Figure **3-3**: Calculated profiles of (a) electric field, (b) refractive index gradient, and (c) deflection angle in a SCC KTN beam deflector with a non-uniform charge distribution.

Based on above figures, we can see that in the section $0 \leq x < d_1$, $\theta \propto \rho_1$, in the section $d_1 \leq x < d_2$, $\theta \propto \rho_2$, and in the section $d_2 \leq x < d_3$, $\theta \propto \rho_3$. In other words, different sections have different deflection angles. This can be useful for some applications (e.g., electric-field-controlled beam separation). However, to achieve a uniform beam deflection angle throughout the entire KTN crystal, non-uniform charge distribution must be avoided.

3.3 Experimental results and discussion

To verify our theory, we prepared a SCC beam deflector. A KTN crystal was diced into a 2.5 mm × 2.5 mm × 5 mm cuboid with six polished faces. A pair of titanium/gold electrodes were applied to the 2.5 mm × 2.5 mm faces in the x direction. The crystal was mounted onto a temperature-controlling Peltier module, which was then mounted onto a 3-D stage. A graphic sheet was set three meters away from the deflector. A DC bias was applied along the x direction, as shown in Fig. 3-4.

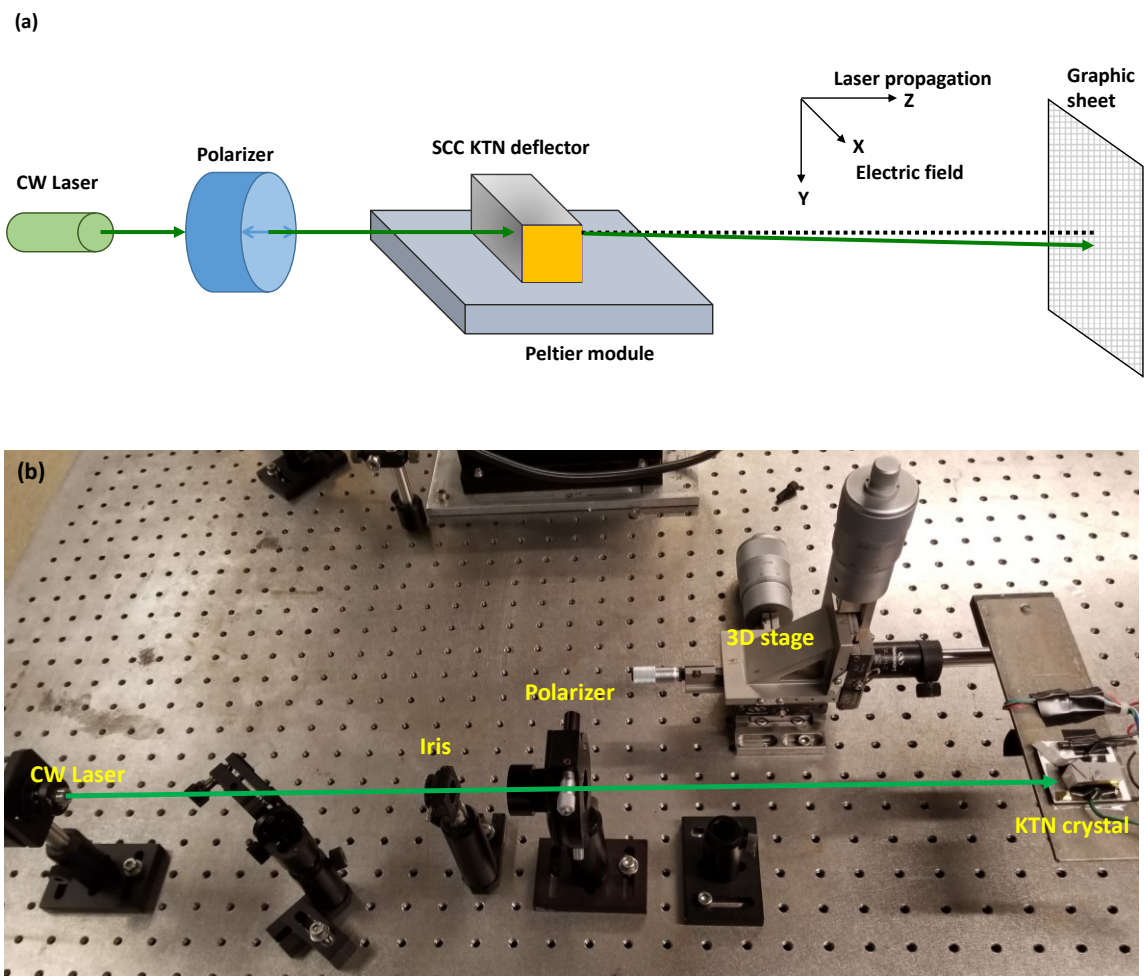

Figure **3-4**: (a) Illustration and (b) photo of the experimental setup.

The experiment was performed at a temperature of 28 ºC, which was well above the Curie temperature of the crystal (21 ºC), so that it was in a cubic phase and free of possible birefringence caused by field-induced phase transition. The external driving voltage was 2000 V, which was near 400 V/mm for the crystal and a proper biasing field for a SCC beam deflector. The laser beam was fixed at half the height of the crystal, 5 mm from the top or bottom of the crystal. A series of beam deflection procedures was then measured at the closest position to the cathode and at every mm away from the cathode until the anode was reached by horizontally adjusting the 3-D stage in the x-direction. The result of the experiment is shown in Fig. 3-5(a). Mathematical calculation was performed based on the previously proposed model, setting d_1, d_2, and d_3 at 0.8, 2.75, and 5 mm, respectively, and the space charge densities ρ_1, ρ_2, and ρ_3 at 45, 35, and 25 C/m^3, respectively, as shown in Fig. 3-5 (b). As can be seen in Fig. 3-5 (a), the deflection angle at different distances from the cathode shows a trend that, overall, aligns well with the calculated model shown in Fig. 3-5 (b). Non-uniform distribution of space charges occurred, although the charges were fairly divided into three portions between the cathode and anode. Higher accuracy can be achieved if the distribution is divided into more portions between the electrodes in the calculated model.

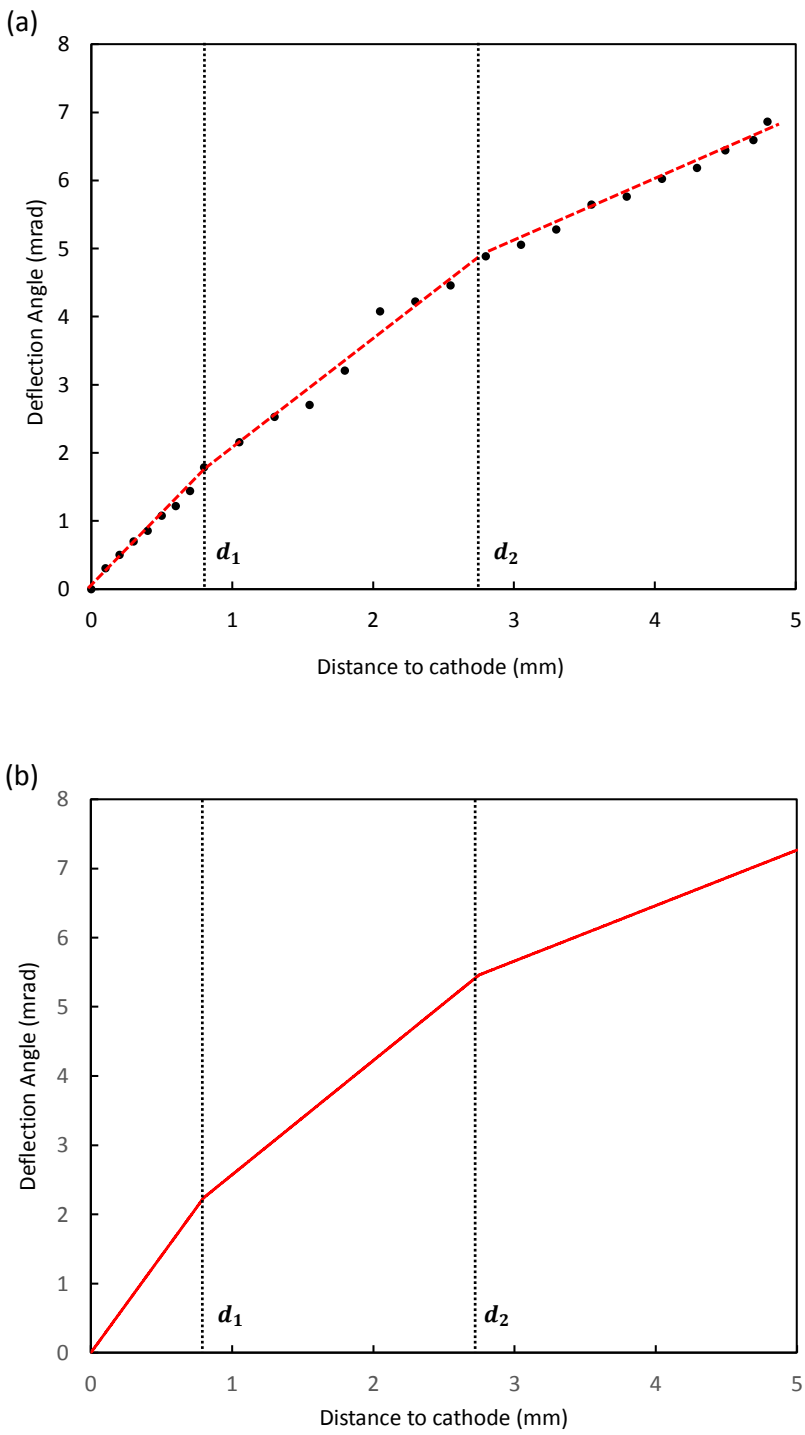

Figure **3-5**: (a) SCC beam deflection in a 2.5 mm × 2.5 mm × 5 mm KTN crystal at 28 ºC and 2000 V at different locations until halfway between the cathode and anode. (b) Calculated beam deflections based on the model proposed in this study.

3.4 Conclusion

This study quantitatively analyzed the electric field distribution and deflection angle of a non-uniform SCC KTN beam deflector. This theoretical analysis was experimentally verified.

We found that the beam deflection angle could be different in different regions due to the non-uniform injected space charge distribution. Our mathematical model provides an efficient way to analyze non-uniform charge distribution in KTN crystal, which could be useful for applications such as electric-field-induced beam separation. However, to achieve a uniform beam deflection angle, non-uniform space charge distribution must be avoided.

Chapter 4

2-D Beam Deflection Enabled by SCC and Temperature-Gradient KTN Deflectors

Due to the rapid advances in technologies such as 3D printing, vivo imaging, and optical coherence tomography, there has been increasing demand for a high-resolution, high-speed optical beam scanner that can operate in multiple dimensions [1-3]. Due to their fundamental physical limitations, it is difficult for conventional mechanical deflectors to achieve sub-microsecond deflection speed. Therefore, there has been significant interest in developing high-speed, non-mechanical beam scanners. In comparison to traditional mechanical beam deflectors, beam deflectors based on the EO effect not only features a faster frequency response, but also is free from mechanical movement-induced noise. Additionally, the deflection angle can be precisely controlled by modulating the EO phase delay. The use of different materials, such as KH_2PO_4 [17], PZT [18], and LiTaO3 [19], in EO beam deflectors has been explored. However, these materials' performance is limited by a relatively small EO coefficient.

Among the many different types of EO materials, potassium tantalate niobate (KTN) has the greatest potential due to its large EO coefficient when operated in the paraelectric phase [72]. The quadratic EO coefficient of 6.94×10^{-14} m^2/V^2 was, by far, the largest EO Kerr effect found in EO media [86], which was by far the largest EO Kerr effect found among all EO media.

By taking advantage of the large EO coefficient, KTN beam deflectors have a number of advantages, such as high-speed response, low driving voltage, and the ability to work at room temperature. These features have made KTN a popular material in various applications, such as optical coherent tomography [29], high-speed spectrometry [23], wavelength tunable lasers [30], optical wave guides [28], and holographic memory systems [32].

Recently, a type of KTN beam deflector using an SCC mechanism was developed [34, 47] and became commercially available. It functions by injecting electrons into the KTN crystal and then performing EO modulation in the paraelectric phase. The injected electrons generate a non-uniform electric field, resulting in an electric-field-dependent prism-shaped refractive index distribution via the quadratic EO effect. This distribution can deflect incoming light beams.

Despite the great qualities of this KTN beam deflector, it does have a few weaknesses that must be dealt with. One is the field-induced phase transition [26, 84, 85] associated with a rise in the Curie temperature, which occurs when a high biasing field is applied to the crystal. In addition, the resolution, which is essential for optical scanning devices, could be improved. Two major factors that determine the resolution are aperture size and deflection angle. Although the KTN beam deflector with space-charge modulation has a decent deflection angle, the aperture size is limited by the penetration depth of the injected charge. Furthermore, only 1-D beam deflection has been achieved on KTN single crystal.

Appropriately lining up two deflectors can result in 2-D beam deflection. However, such a deflector requires more power to operate and more complexity to achieve 2-D scanning. In this study, we report 2-D scanning based on a combination of two different physical scanning mechanisms in an effort to achieve compact, cost-effective 2-D deflection. In addition to SCC beam deflection in the x direction, we employ another beam-deflecting mechanism on the same KTN crystal by inducing a temperature gradient in the y direction. Since the relative permittivity of KTN near its Curie temperature is strongly dependent on the operating temperature in the paraelectric phase, a gradient forms in the refractive index and, in accordance with the induced temperature gradient inside the crystal, bends the incoming laser beam in the y direction. As a result, beam deflection can be achieved in both the x and y directions in KTN single crystal.

4.1 SCC KTN beam deflection

To understand the physical mechanisms of 2-D deflection in a KTN beam deflector characterized by both SCC and a temperature gradient, we briefly review the physical mechanism of 1-D deflection when only SCC is involved.

SCC beam deflection was first reported by Nakamura et al. [33]. It is believed that the external field induces a rise in the energy level of electrons at the electrodes, allowing charges to drift across the Schottky barrier between the crystal and electrode and driving them towards the other electrode. When the charges are injected into the crystal, the electric field distribution inside the crystal is altered. This changes the refractive index inside the crystal, causing the input beam to deflect. Later, Miyazu et al. [34] found that the injected charges could be trapped due to defects in the crystal. These charges could be stored in the crystal for hours before being naturally released or pushed out by the excitation of other energy sources. Assuming that the trapped charges were uniformly distributed with a density of N in the crystal, Miyazu et al. [34] developed a mathematical model to describe space-charge-preinjected KTN beam deflection. Based on Gauss's law, the overall electric field distribution inside a crystal with an applied external field can be expressed as follows [34]:

$$E(x) = -\frac{eN}{\varepsilon}\left(x - \frac{G}{2} + \frac{\varepsilon V}{eNG}\right), \tag{4.1}$$

where e is the electric charge, ϵ is the permittivity of the crystal, G is the gap between electrodes, and V is the applied voltage. The change in the refractive index due to the EO Kerr effect is given by the following equation [34]:

$$\Delta n(x) = -\frac{1}{2} n^3 g_{11} \varepsilon^2 E(x)^2$$

$$= -\frac{1}{2} n^3 g_{11} e^2 N^2 \left(x - \frac{G}{2} + \frac{\varepsilon V}{eNG} \right)^2, \tag{4.2}$$

where n is the refractive index and g_{11} is the EO coefficient of the crystal in polar form when the polarization of the beam is parallel to the applied electric field. For a beam that has traveled a distance of L in the crystal, the deflection angle can be given by the following equation:

$$\theta(x) = L \frac{d}{dx} \Delta n(x)$$

$$= -n^3 g_{11} e^2 N^2 L \left(x - \frac{G}{2} + \frac{\varepsilon V}{eNG} \right). \tag{4.3}$$

As can be seen in Eq. (4.3), the deflection angle, θ, is proportional to the external voltage. Therefore, the scanning speed of the deflector can be as fast as the voltage source. Fig. 4-1 shows the configuration of an SCC KTN beam deflector.

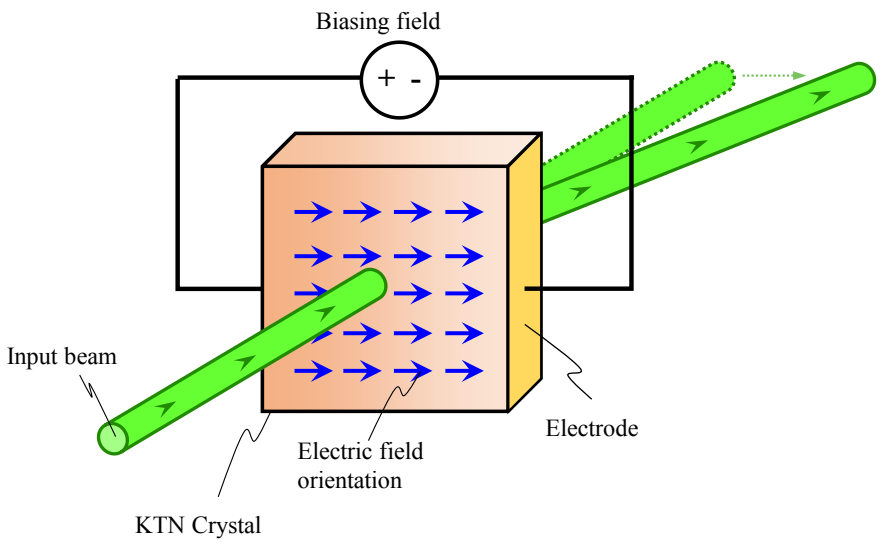

Figure **4-1**: Illustration of a 1-D SCC KTN beam deflector.

4.2 2-D beam deflection by temperature-gradient and SCC KTN beam deflectors

To achieve 2-D beam deflection, the input beam has to experience a gradient of the refractive index in two dimensions within the KTN crystal. To do so, we assume that the space charge is uniformly injected in the KTN crystal, as in the typical SCC deflection model, by applying a pair of parallel conductive plates in the x direction with a charge density of ρ. We also assume that there is a temperature gradient in the y direction created by attaching a pair of temperature-controlling plates on the bottom and top surfaces of the KTN crystal, as illustrated in Fig. 4-2. The red and blue arrows in the figure represent the directions of the temperature gradient and electric field, respectively, and the thick green line denotes the light propagation direction. The temperatures of bottom and top plates are T_1 and T_2, respectively. In this case, inhomogeneous permittivity, $\varepsilon(y) = \varepsilon_0 \varepsilon_r(y)$, is induced in the y direction.

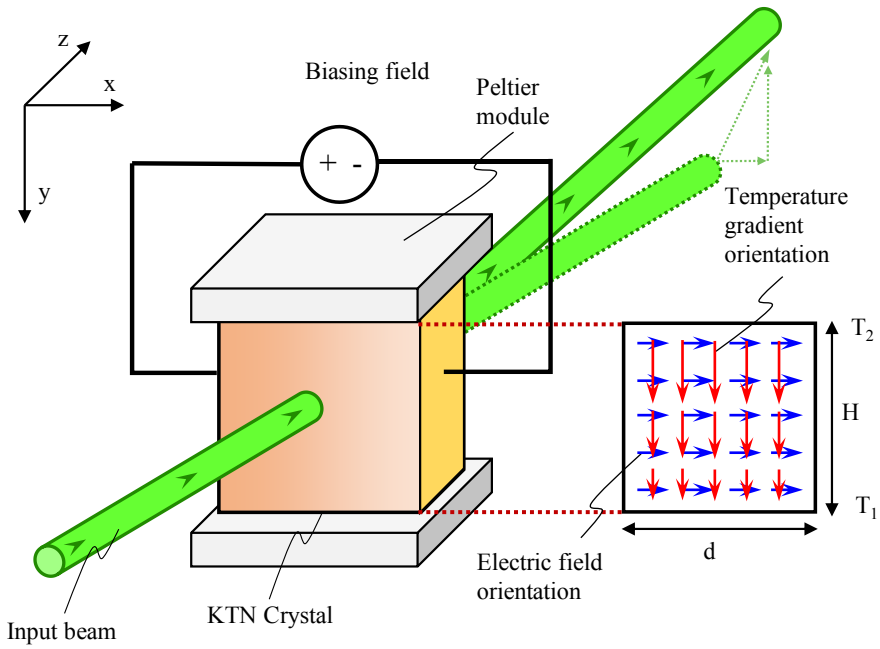

Figure **4-2**: Sketch of a 2-D temperature-gradient and SCC KTN beam deflector.

For simplicity, we assume that the temperature gradient is linear in the y direction and the distance between bottom and top plates is H. Therefore, the temperature at an arbitrary location, y, can be derived from the following equation:

$$T(y) = T_1 + (T_2 - T_1)\frac{y}{H}, \tag{4.4}$$

where $T_2 > T_1$. In the paraelectric phase, the relative permittivity of KTN follows the Curie-Wiess law [89]:

$$\varepsilon_r = \frac{C_1}{T - T_c}, \tag{4.5}$$

where C_1 is a material-specific Curie constant and T_c is the Curie temperature of KTN. Substituting Eq. (4.4) into Eq. (4.5), we obtain the following:

$$\varepsilon_r(y) = \frac{C_1}{T_1 + (T_2 - T_1)\dfrac{y}{H} - T_c}. \tag{4.6}$$

To achieve 2-D refractive index modulation, we first need to calculate the static electric field by solving the Maxwell equations. In this inhomogeneous dielectric case, Maxwell's equations are as follows [90]:

$$\nabla \times E = 0, \tag{4.7}$$

$$\nabla \cdot D = \rho, \tag{4.8}$$

where $E = (E_x, E_y, E_z)$ and $D = \varepsilon(y)E$. Since the permittivity is homogeneous in the z direction and there is no electric field applied in the z direction, we find that $E_z = 0$ due to symmetry. Substituting this condition into Eq. (4.7), we obtain the following:

$$\nabla \times E = \begin{vmatrix} \hat{x} & \hat{y} & \hat{z} \\ \dfrac{\partial}{\partial x} & \dfrac{\partial}{\partial y} & \dfrac{\partial}{\partial z} \\ E_x & E_y & 0 \end{vmatrix} = 0. \tag{4.9}$$

Eq. (4.9) can be further decomposed into three scalar equations as follows:

$$\frac{\partial E_x}{\partial z} = 0, \tag{4.10a}$$

$$\frac{\partial E_y}{\partial z} = 0, \tag{4.10b}$$

$$\frac{\partial E_x}{\partial y} = \frac{\partial E_y}{\partial x}. \tag{4.10c}$$

Eqs. (4.10a) and (4.10b) indicate that E_x and E_y are the only functions of x and y, as given by $E_x(x, y)$ and $E_y(x, y)$. In this case, Eq. (4.8), can be written as follows:

$$\frac{\partial(\varepsilon(y)E_x)}{\partial x} + \frac{\partial(\varepsilon(y)E_y)}{\partial y} = \rho. \tag{4.11}$$

Since $\varepsilon(y)$ is not a function of x, Eq. (4.11) can be simplified as follows:

$$\varepsilon(y)\frac{\partial E_x}{\partial x} + \frac{d\varepsilon(y)}{dy}E_y + \varepsilon(y)\frac{\partial E_y}{\partial y} = \rho. \tag{4.12}$$

To obtain a partial differential equation containing only E_x, we apply $\frac{\partial}{\partial x}$ to both sides of Eq. (4.12), creating the following:

$$\varepsilon(y)\frac{\partial^2 E_x}{\partial x^2} + \frac{d\varepsilon(y)}{dy}\frac{\partial E_y}{\partial x} + \varepsilon(y)\frac{\partial \frac{\partial E_y}{\partial x}}{\partial y} = 0. \tag{4.13}$$

Substituting Eq. (4.10c) into Eq. (4.13), we obtain the following:

$$\varepsilon(y)\frac{\partial^2 E_x}{\partial x^2} + \frac{d\varepsilon(y)}{dy}\frac{\partial E_x}{\partial y} + \varepsilon(y)\frac{\partial^2 Ex}{\partial y^2} = 0, \tag{4.14}$$

which only contains E_x. Similarly, by applying $\frac{\partial}{\partial y}$ to both sides of Eq. (4.12) and inserting Eqs. (4.10c) and (4.12) into the new equation, we obtain the following:

$$\varepsilon(y)\left(\frac{\partial^2 E_y}{\partial x^2}+\frac{\partial^2 E_y}{\partial y^2}\right)+\frac{d\varepsilon(y)}{dy}\frac{\partial E_y}{\partial y}+$$

$$\left[\frac{d^2\varepsilon(y)}{dy^2}-\frac{1}{\varepsilon(y)}\left(\frac{d\varepsilon(y)}{dy}\right)^2\right]E_y+\frac{1}{\varepsilon(y)}\frac{d\varepsilon(y)}{dy}\rho=0\ , \tag{4.15}$$

which only contains E_y. We assume following boundary conditions:

$$E_y(0,y)=0\,, \tag{4.16a}$$

$$E_y(G,y)=0\,, \tag{4.16b}$$

$$\int_0^G E_x dx=V\ , \tag{4.16c}$$

where G and V are the differences in distance and voltage between the two electrodes, respectively. Theoretically speaking, by solving Eqs. (4.14)–(4.16) simultaneously, we can obtain E_x and E_y. We further assume that the polarization of the incoming light occurs in the x direction. In this case, the corresponding refractive index modulation can be derived from the following equation:

$$\Delta n(x,y)=-\frac{1}{2}n^3 g_{11}\varepsilon_0{}^2(\varepsilon_r(y)-1)^2 E_x{}^2-\frac{1}{2}n^3 g_{12}\varepsilon_0{}^2(\varepsilon_r(y)-1)^2 E_y{}^2\,, \tag{4.17}$$

where g_{11} and g_{12} are the quadratic EO coefficients in the polar form and n_0 is the refractive index without an applied electric field. The beam deflection in the x and y directions can be derived from the following:

$$\theta_x = L\frac{\partial \Delta n(x,y)}{\partial x}$$

$$= -Ln^3 g_{11}\varepsilon_0^{\ 2}(\varepsilon_r(y)-1)^2 E_x \frac{\partial E_x}{\partial x} - Ln^3 g_{12}\varepsilon_0^{\ 2}(\varepsilon_r(y)-1)^2 E_y \frac{\partial E_y}{\partial x}, \tag{4.18a}$$

$$\theta_y = L\frac{\partial \Delta n(x,y)}{\partial y}$$

$$= -Ln^3 g_{11}\varepsilon_0^{\ 2}(\varepsilon_r(y)-1)\frac{d\varepsilon_r(y)}{dy} E_x^{\ 2} - Ln^3 g_{11}\varepsilon_0^{\ 2}(\varepsilon_r(y)-1)^2 E_x \frac{\partial E_x}{\partial y}$$

$$-Ln^3 g_{12}\varepsilon_0^{\ 2}(\varepsilon_r(y)-1)\frac{d\varepsilon_r(y)}{dy} E_y^{\ 2} - Ln^3 g_{12}\varepsilon_0^{\ 2}(\varepsilon_r(y)-1)^2 E_y \frac{\partial E_y}{\partial y}, \tag{4.18b}$$

where L is the propagation length of the light beam in the z direction.

Unfortunately, there are no obvious closed-form analytic solutions for Eqs. (4.14) and (4.15) when $\varepsilon(y)$ is not a constant and $\rho \neq 0$. Thus, we adopted a numerical approach to solve Eqs. (4.14) and (4.15). We began by establishing the temperature gradient for this computation. To ensure that the result of the numerical computation would be consistent with the experimental result, we used realistic experimental parameters. The dimensions of the KTN crystal were 3 mm x 3 mm x 3 mm. The Curie temperature was $T_c = 22\ ^oC$. The bottom (y = 0 mm) and top (y = 3 mm) temperatures were set at $T_1 = 23\ ^oC$ and $T_2 = 38\ ^oC$, respectively. We assumed $C_1 = 110000$ in Eq. (4.6). Fig. 4-3 shows the calculated permittivity distribution as a function of position on the y-axis under the conditions described above. To avoid complexity in the electric fields near the edges (i.e., $y = 0$ and $y = H$) as well as singularity when $T \rightarrow T_c$, based on Eq. (4.6), only $\varepsilon_r(y)$ within a range of 0.5–2.5 mm was employed. The calculated numbers were

similar to the experimental results reported in [17, 19, 23] for the KTN crystals with a similar Curie temperature.

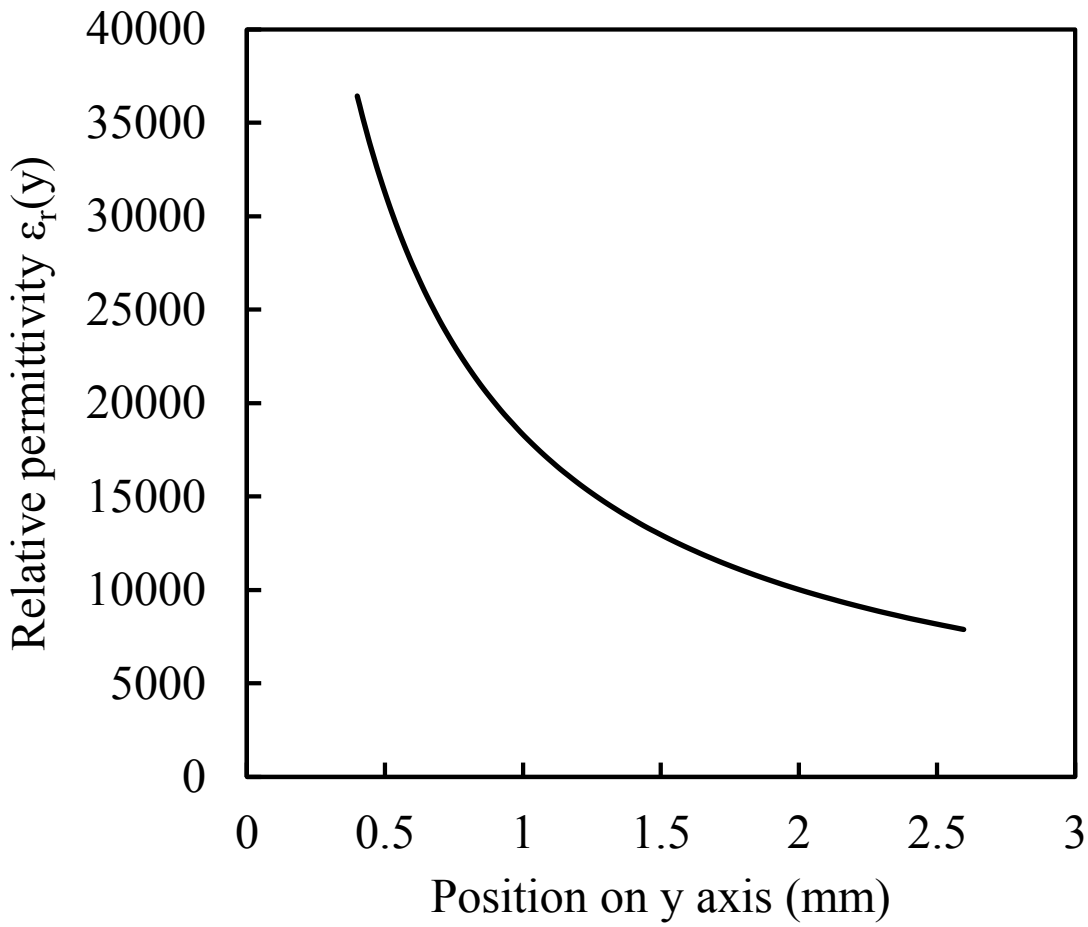

Figure **4-3**: Calculated relative permittivity, $\varepsilon_r(y)$, as a function of location y with the following parameters: $T_1 = 23\ ^oC$, $T_2 = 38\ ^oC$, $T_c = 23\ ^oC$, $C_1 = 110{,}000$, and $H = 3\ mm$.

To investigate the influence of the temperature gradient on the electric field distribution inside the KTN crystal, we compared the electric field distribution in KTN with and without the temperature gradient. We assumed an external applied voltage of $V = 800V$, $\varepsilon_r = 13000$ and a uniformly injected charge density of $\rho = -3\ C/m^3$, which were both realistic parameters and

within the same order of magnitude as the previously reported experimental results [33, 34, 84]. Fig. 4-4(a) shows the electric field distribution without the temperature gradient (i.e., $T_1 = T_2$). It is obvious that the electric field only occurs in the x direction. Then, based on Eqs. (4.13)–(4.15), we computed the electric field with a temperature gradient (i.e., $T_1 = 23\ ^oC\ and\ T_2 = 38\ ^oC$), as shown in Fig. 4-4(b). In this case, E_y was no longer 0, but it was too small compared to E_x to be observed. Hence, we enlarged E_y in Fig. 4-4 (b) by 200 times to show that the E-field distribution did in fact occur in both the x and y directions.

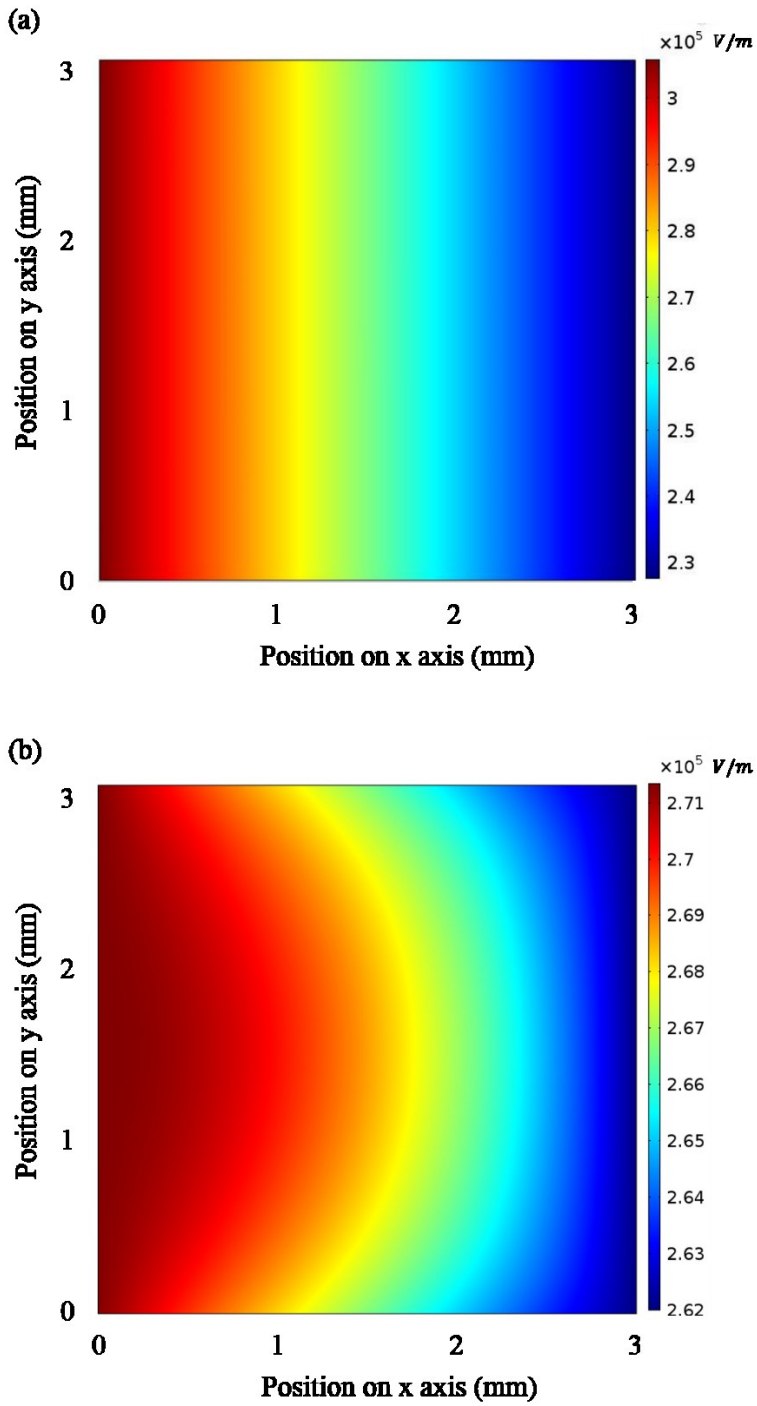

Figure **4-4**: Calculated electric field under an external biasing field (a) without a temperature gradient, in which case $E_y = 0$, and (b) with a temperature gradient of $T_1 = 23\ ^oC\ and\ T_2 = 38\ ^oC$, in which case $E_y \neq 0$. The colored bar shows the magnitude of the electric field in V/m.

We then computed the refractive index distribution by inserting the electric field distribution obtained in Figs. 4-4 (a) and (b) into Eq. (4.17). We started by applying the refractive index modulation without the external electric field, as shown in Fig. 4-5. The refractive index was almost uniform in this case, but a small variation induced by the internal electric field and created by the injected charge was slightly observable. This almost-uniform refractive index modulation had a negligible effect on light beam deflection.

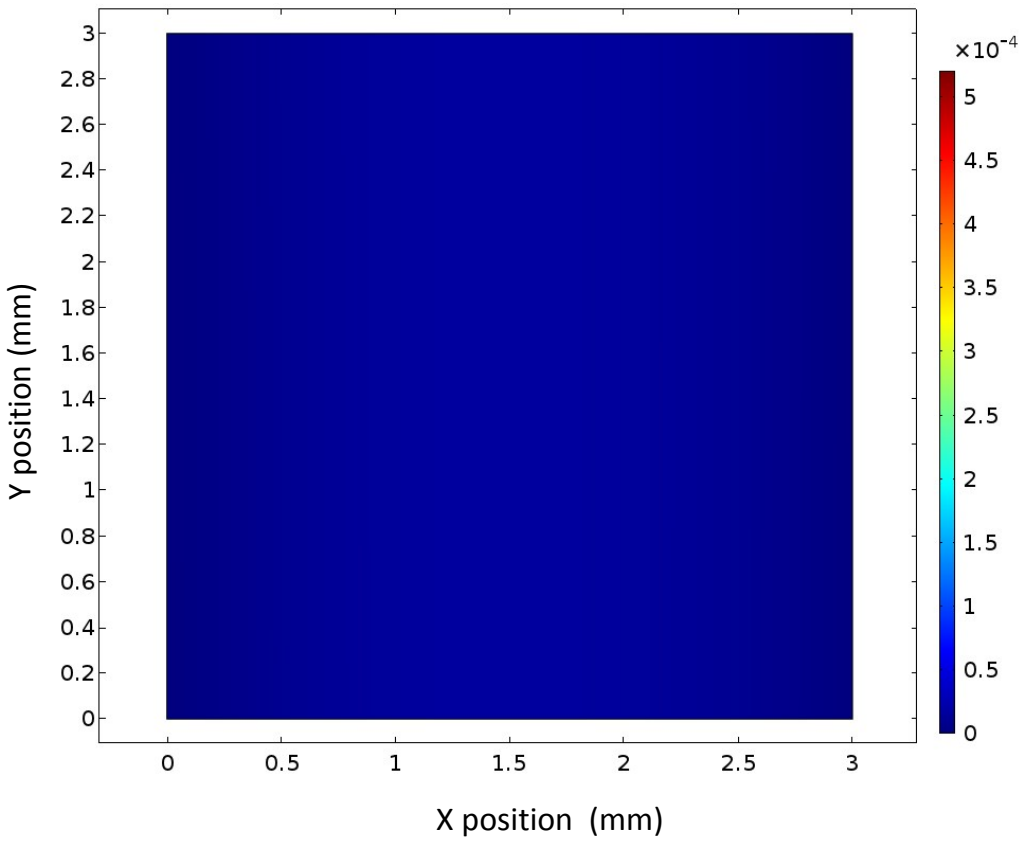

Figure **4-5**: Calculated refractive index modulation in space-charge-injected KTN crystal without applying an external electric field.

Again, we compared the refractive index modulation without and with a temperature gradient under an external electric field (V = 800 V), as shown in Figs. 4-6(a) and (b), respectively. Fig. 4-6(a) shows that refractive index modulation occurred in only the x direction, and thus beam deflection could occur only in the x direction. Fig. 4-6(b), on the other hand, clearly shows that, with the induced temperature gradient of $T_1 = 23\ ^oC$ and $T_2 = 38\ ^oC$, the refractive index was distributed in both the x and y directions, enabling 2-D beam deflection.

Finally, by substituting the calculated refractive index modulation into Eqs. 4-18(a) and 4-18(b), we obtained beam deflection as a function of the external electric field. The computed beam deflections were compared with the experimental results, as discussed in detail in the following section.

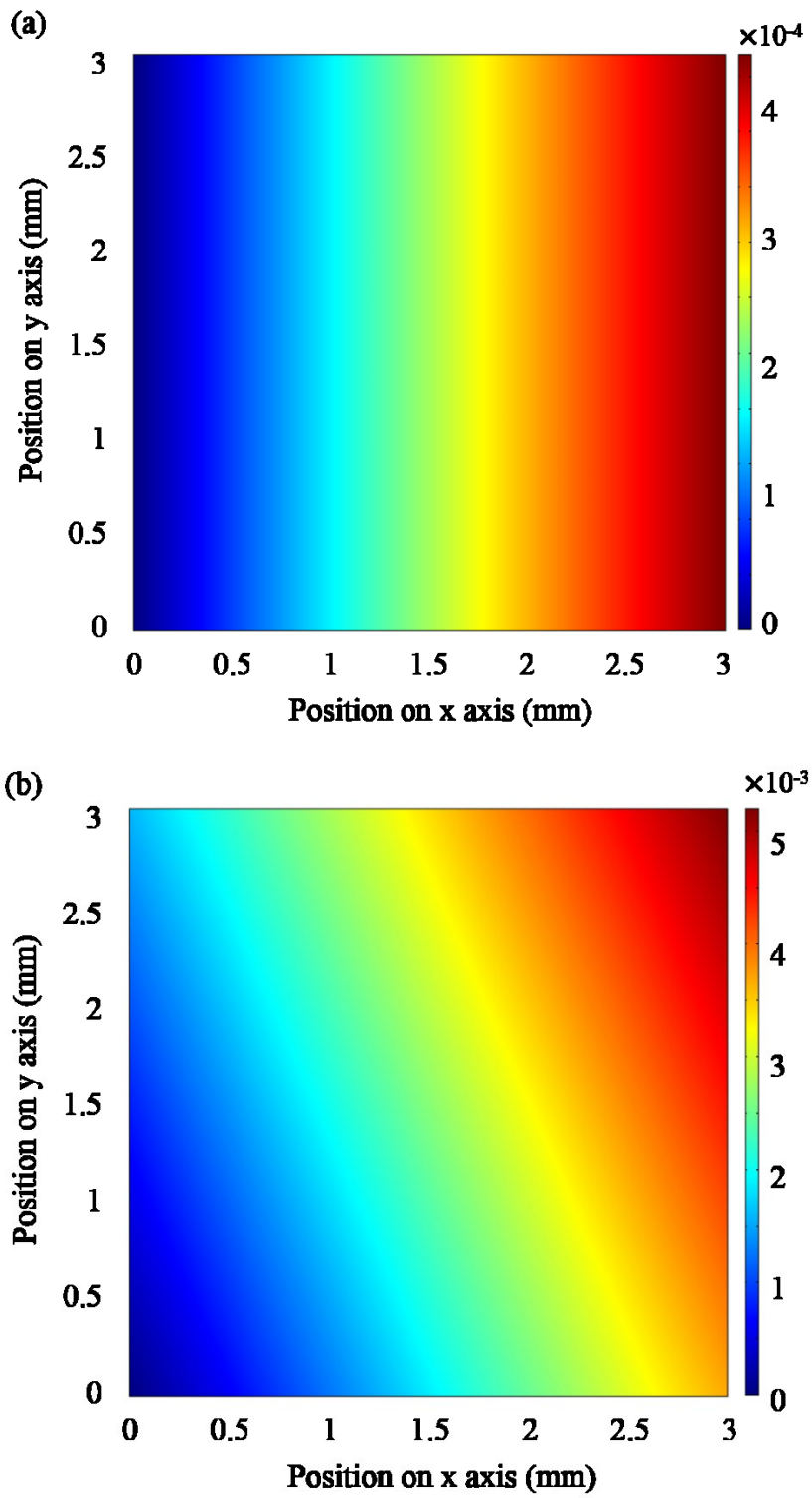

Figure **4-6**: Calculated refractive index distribution (a) without a temperature gradient (i.e., $T_1 = T_2$) and (b) with a temperature gradient of $T_1 = 23\ ^oC$ and $T_2 = 38\ ^oC$.

4.3 Experimental results and discussion

We conducted an experiment to validate the proposed 2D beam deflector with both SCC and a temperature gradient. In the experiment, a cubic KTN crystal with a side length of 3 mm was coated with a pair of titanium/gold electrodes on the surface along the x direction, as illustrated in Fig. 4-2. The Curie temperature of this KTN crystal was $T_c = 22\ ^oC$. Two Peltier thermo-electric modules connected to a temperature controller were attached to the surfaces in the y direction. The temperatures of the bottom and top Peltier thermo-electric modules were set at $T_1 = 23\ ^oC\ and\ T_2 = 38\ ^oC$, respectively. A horizontally polarized diode-pumped solid-state laser beam with an output wavelength of 532 nm travelled in the z direction through the center of the x-y surface. A DC biasing field was applied to the crystal in the x direction via the electrodes. The output beam was projected onto a graph sheet. Fig. 4-7 shows an illustration and photo of the experimental setup.

(a)

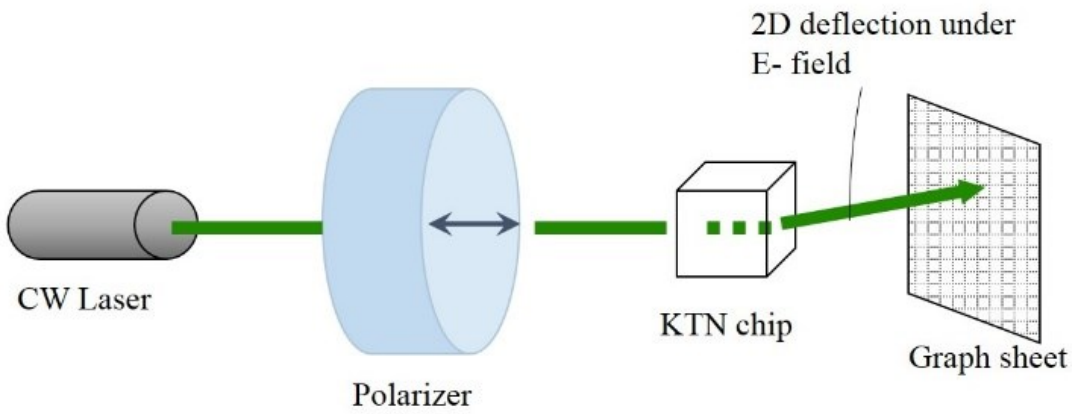

(b)

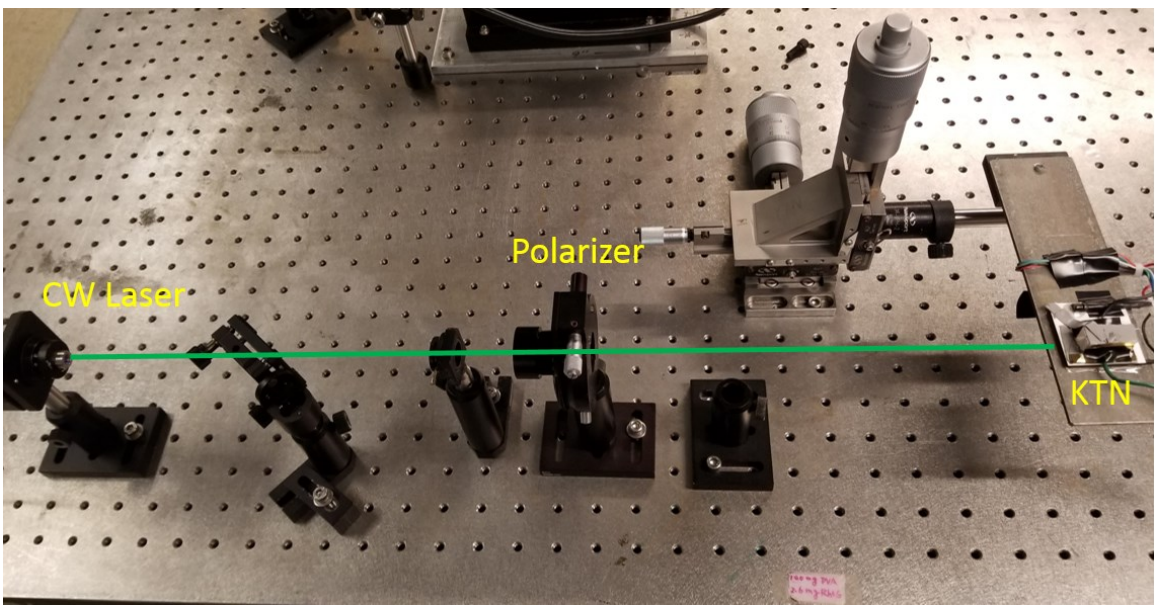

Figure **4-7**: (a) Illustration and (b) photo of the experimental setup used to measure the deflection angle.

In the experiment, the deflection angles were measured at different applied voltages (100–800 V) with an interval of 100 V. The measured data points formed a 2-D trace on the projection

surface, which was analyzed in the x and y directions separately, as shown in Figs. 4-8(a) and 4-8(b). The circular dots in Fig. 4-8(a) show the experimentally measured deflection angles in the x direction. For comparison, the deflection angles computed using Eq. 4.18(a) with the same parameters (i.e., $T_1 = 23\ ^oC\ and\ T_2 = 38\ ^oC$) are depicted as solid lines in Fig. 4-8(a). In Fig. 4-8(b), the triangular dots represent the deflection angles measured in the y direction with different applied voltages. To quantify the difference between the experimental and theoretical results, we computed the average relative difference (i.e., the average deflection difference/deflection range) between the theoretical and experimental results for deflection angles in x and y directions, which was 2.9% and 7.2%, respectively. This confirmed that the theoretical and experimental results had good agreement. Furthermore, as shown in Fig. 4-8(b), deflection shows a slight linear trend at low voltages (e.g., <200V) and a parabolic increase at high voltages (e.g., >200 V). In other words, the quadratic term (i.e., the first term of Eq. 4-17(b)) dominates in that equation as the applied field increases. Note that the measured deflection angle was smaller than that reported in [19] due to the lower injected charge density in our KTN sample. As mentioned in [26], there were large variations in the injected charge density with a given external electric field and penetration depth among different KTN samples, even those with similar compositions, due to uncontrollable perturbations (e.g., temperature fluctuations) in the growing process. For example, as reported in [26], with the same applied electric field (300 V/mm) and a penetration depth of 0.5 mm, sample A had an injected charge density of $\rho = -70\ \mathrm{C\ /\ m^3}$, while sample B had an injected charge density of $\rho = -5\ \mathrm{C\ /\ m^3}$. The value of sample B was comparable to the injected charge density in this study ($\rho = -3\ \mathrm{C\ /\ m^3}$) awith an applied field of 266.7 V/mm. In other words, although the value of the injected charge density in this study was small, it was still within the range of the previously reported values.

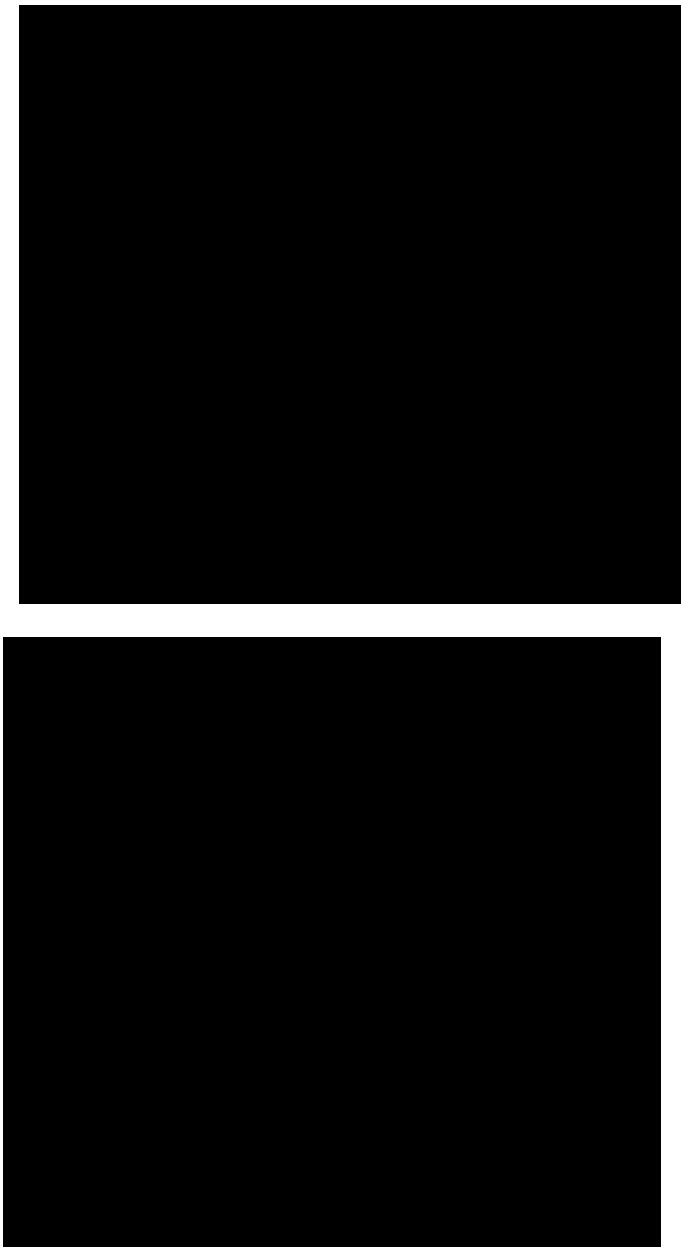

Figure **4-8**: Deflection angles (a) in the x direction at different applied voltages, with the circular dots representing the experimentally measured results and the solid line denoting the deflection angles calculated based on Eq. 4.18(a), and (b) in the y direction at different applied voltages, with triangular dots representing the experimentally measured results and the solid line denoting the deflection angles calculated based on Eq. 4.18(b).

As mentioned previously, in our approach, deflection in the x direction was caused by the space-charge-injection-induced gradient electric field, while deflection in the y direction was caused by the temperature-gradient-induced gradient electric field and gradient permittivity distribution. To show the 2-D deflection capability of the deflector, we measured deflection as a function of voltage in the x and y directions at different temperature gradients, as shown in Fig. 4-9. It is evident that the deflection angles could cover the entire x-y plane if the applied voltage and magnitude of temperature gradient were adjusted. In other words, the beam could be deflected to any location in the x-y plane if the proper combination of applied voltage and temperature gradient magnitude were selected.

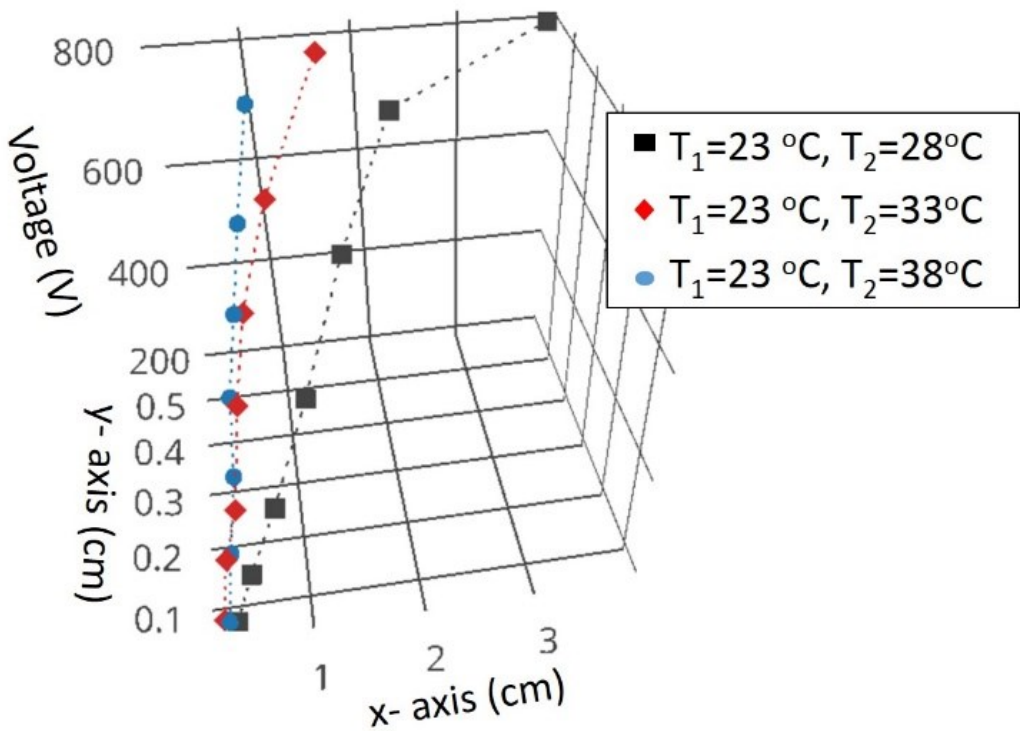

Figure **4-9**: Deflection locations in the x-y plane measured at different voltages (100–800V) with an interval of 100V under different temperature gradients. The square, diamond-shaped, and circular dots denote the measured deflection locations corresponding to temperature gradients of 23–28 ºC, 23–33 ºC, and 23–38 ºC, respectively.

4.4 Speed performance of the 2-D KTN deflector

Finally, to demonstrate the capability of high-speed beam deflection, we measured the deflection speed using the experimental setup illustrated in Fig. 4-10. An iris was placed between the beam deflector and a high-speed photodetector (FEMTO Messtechnik GmbH HCA-S-200M-Si) connected to an oscilloscope. When a fast-changing voltage signal was induced, the beam was deflected and then blocked by the iris. Hence, the photodetector could measure the change in light intensity as a function of time, which indicated the deflection speed. In this experiment, a fast-changing voltage signal with a rise time of about 1 ns was applied to the KTN crystal. Fig. 4-11 shows the drop in detected light intensity as a function of time. Despite some slight noise from the circuit, there is a clear response time of 77 ns (from 90% to 10%). The capacitance of the KTN crystal in this experiment was 0.54 nF, and the impedance of the circuit was 68 ohm. Thus, the rise time of the RC circuit was 81 ns, which is close to the measured response time. The speed of this device was mainly limited by the RC time constant of the circuit in this experiment. The results confirm that very fast deflection speed can be achieved.

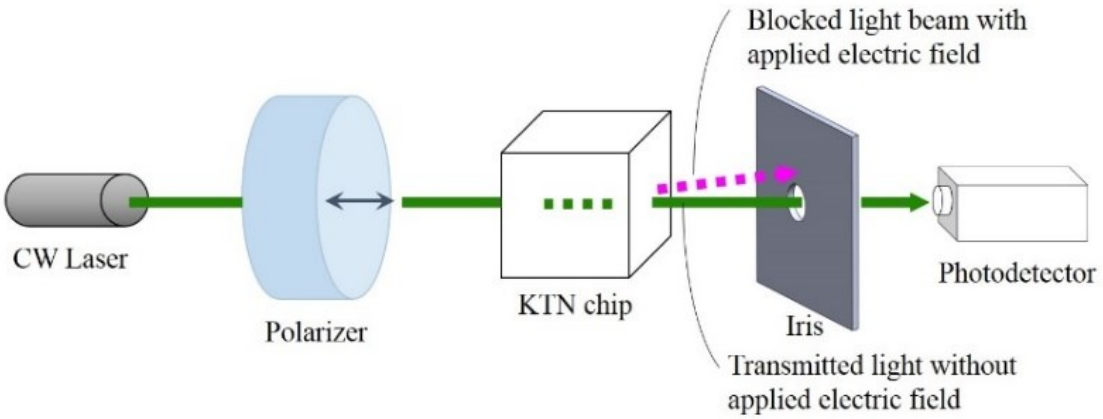

Figure **4-10**: Experimental setup used to measure deflection speed.

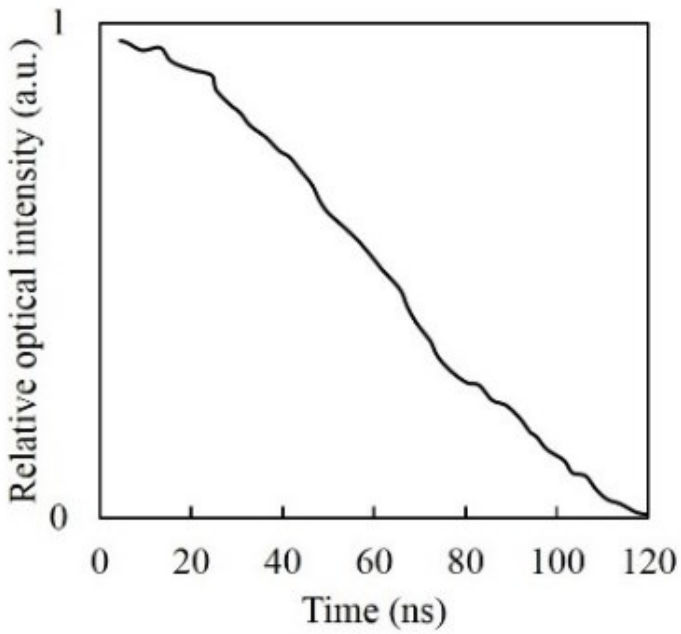

Figure **4-11**: Measured time response of beam deflection.

4.5 Conclusion

In this study, 2-D KTN beam deflection was successfully achieved by combining two deflection mechanisms: SCC beam deflection and temperature-gradient-controlled beam deflection in the x and y directions, respectively. By applying an external biasing field in the x direction and inducing a temperature gradient in the y direction on KTN single crystal, deflection in both the x and y directions was observed. The effects of the space-charge and temperature-gradient mechanisms were quantitatively analyzed and experimentally confirmed. The maximum difference between the experimental results and theoretical analyses was about 7%. Furthermore, high-speed (~80 ns) deflection capability was also experimentally demonstrated. Such a compact non-mechanical high-speed beam deflector can be very useful for a variety of applications, including high-speed 3D laser printing, high-resolution high-speed scanning imaging, and free-space reconfigurable laser communications.

Chapter 5

Advanced Laser-Induced Activation Technique for PCSS with SI-GaAs

Electrical devices with laser activation rely on the activation by absorbing a certain amount of optical energy from laser beams. A PCSS is one type of device that harnesses the photoconductivity of semiconductor materials to facilitate electrical switching. The device becomes electrically conductive when it is turned on by laser radiation, and it can hold a large biasing electric field while remaining insulating in its off state.

PCSS was first made with SI-GaAs decades ago, but it is still an active research topic because of its advantageous features, such as ultra-fast switching speed, low-jitter response and delay, high repetition rate, high scalability to large operating voltages or currents, optical control, and simple structure, which have led it to be used in a number of applications, including pulsed power systems, terahertz emitters, and high-speed electronics [37–40]. The abilities of various types of materials, including silicon, silicon carbide, gallium nitride, and hybrid nanocomposites, to further enhance the performance of light-controlled conductive switches have been explored [41–43]. Although the high stability and scalability of the low-bias linear switching of PCSS has been useful in some applications, such as high-speed switches, the high required triggering energy is not optimal. A PCSS in a non-linear mode, however, is advantageous because it requires much lower triggering energy and features a faster turn-on time. In fact, the turn-on time can be even faster than the rise time of optical triggering pulses. In addition, non-linear PCSS has a unique lock-on phase, with the lock-on time ranging from tens to hundreds of nanoseconds and the lock-on voltage determined by the material and dimensions of the switch [44]. In other words, it is possible for a switch to have an ultra-fast turn-on time, customized lock-on output, low required triggering energy, and very compact size. However, an ultra-long lock-on time (e.g., at the

millisecond scale) can be even more advantageous for certain applications, such as a firing set switch [45]. Such a switch requires a minimum ignition energy, which can be produced by, for example, igniting a propane–air mixture [46]. It usually takes a millisecond to accumulate enough ignition energy for the ignition switch in the conduction state. Thus, a PCSS with a long lock-on time (and thus low ignition power, a low driving voltage, and a compact size) is preferred as it provides enough time to achieve the minimum ignition energy.

This chapter reviews the basic physical characteristics of PCSS and technical details regarding the ultra-long lock-on phase of non-linear switching in PCSS. Then, it presents the experiment and characterizes the newly developed front-bonded-ruby PCSS.

5.1 PCSS essentials

Photoconductivity is the physical phenomenon of electrical conductivity between two terminals on a semiconductor material induced by absorption of electromagnetic radiation. The conductivity of some semiconductor materials can be significantly altered (i.e., by many orders of magnitude) when the material absorbs enough photon energy from optical radiation, which is often greater than the band-gap energy of the material. Electron–hole pairs are generated during this process, rendering the material electrically conductive. Thus, an optically controlled electrical switch with a very simple structure can be fabricated by placing metal electrodes across a suitable semiconductor material. A typical lateral configuration of PCSS is shown in Fig. 5-1.

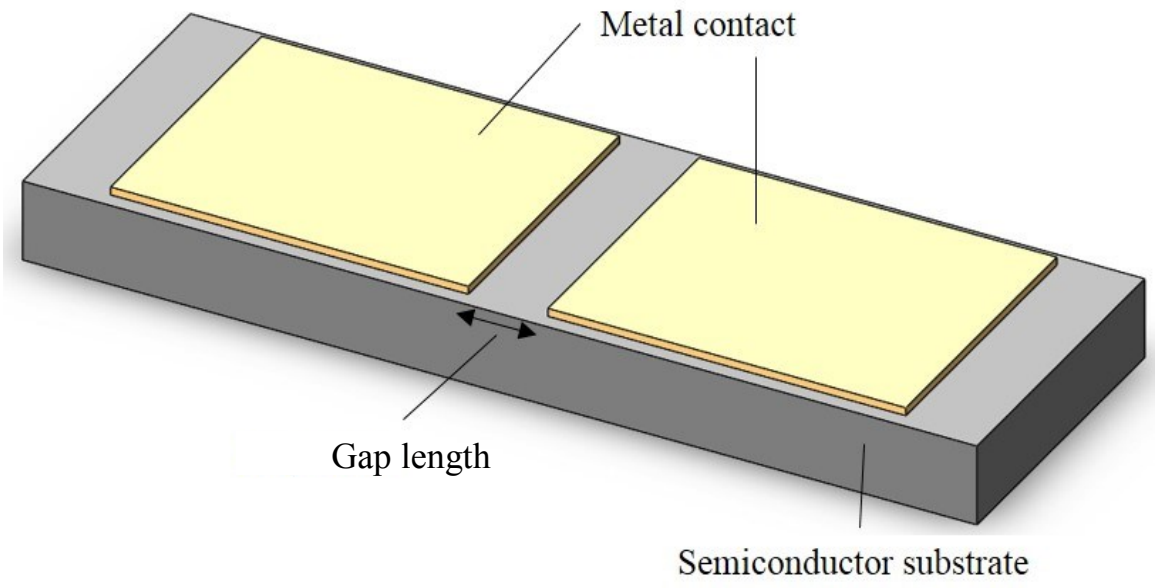

Figure **5-1**: Configuration of a typical lateral PCSS.

5.1.1 Optical absorption of PCSS

Photoconductivity involves optical absorption, photocarrier transport, and recombination, although optical absorption is at the core of the phenomenon. Photoconductivity is largely dependent upon the power of the incident radiation and independent of the size of the illuminated area; that is, a semiconductor of any size could become electrically conductive with sufficient optical radiation. Since the resistance between any two points on the surface of a material is proportional to the distance between the points, changes in conductivity can be modulated with the effect of photoconductivity, enabling a PCSS to function. A typical PCSS is simply a semiconductor substrate with two metal terminals deposited on the surface, as shown in Fig. 5-1. The conductivity between the metal electrodes changes by several orders of magnitude as the gap region absorbs enough energy from the incident radiation. The switching time of a PCSS is usually determined by the rise time of the triggering optical pulse, which is often longer than the time needed for photon absorption. For these reasons, PCSS is often considered an almost-ideal switch. Among the available semiconductor materials, GaAs is the most widely used for PCSS due to its dark resistivity, which can be as high as 10^8 ohm-cm, and high electron mobility.

Optical absorption can be roughly separated into two categories: intrinsic absorption and extrinsic absorption. Intrinsic optical absorption involves the raising of an electron's energy state from the valence band to the conduction band, while extrinsic optical absorption involves the raising of the energy state from a defect to the conduction band or from the valence band to a defect, as shown in Figs. 5-2(a) and (b).

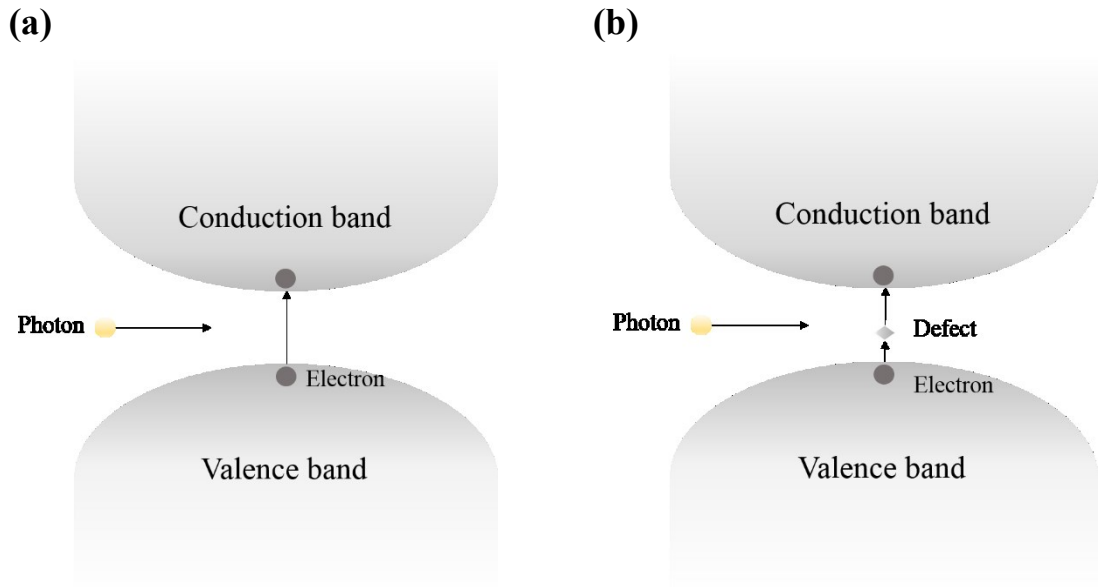

Figure **5-2**: Illustration of optical absorption in semiconductors.

For intrinsic optical absorption, if the conduction band minimum has the same k value in the energy plot as the maximum valence band energy, vertical transition of electron with only the absorption of a photon occurs. Such transition is called *direct optical transition*, and it occurs only in materials with a direct band gap. On the other hand, if the k values of the conduction band minimum and valence band maximum are different, optical transition from the top of the valence band to the bottom of the conduction band must involve absorption of a photon and simultaneous absorption or emission of a phonon. In materials with a direct bandgap, such as GaAs, optical absorption occurs near the surface of a material. Light penetrates much deeper into materials with an indirect bandgap, such as Si.

A few terms are used to describe the behavior of optical absorption. When an optical source illuminates a semiconductor material, its energy is absorbed at an optical absorption depth of d_0. Fig. 5-3 shows the optical absorption depth with respect to the visible light in GaAs. Since

d_0 is dependent upon the wavelength of the incident light, the wavelength of the light is often chosen so that the absorption depth is much less than the semiconductor thickness to ensure complete absorption of energy.

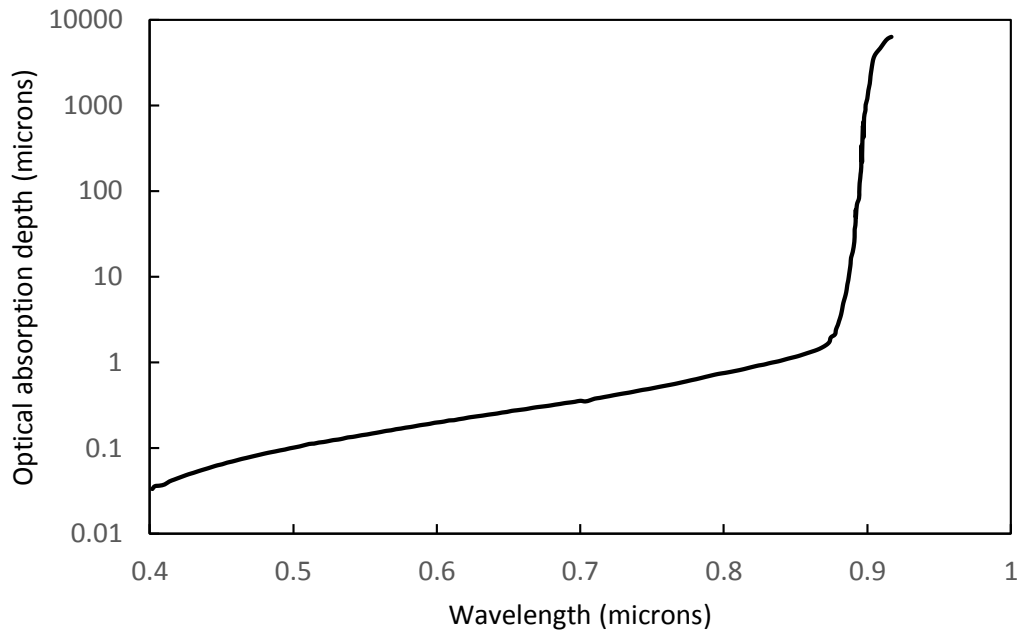

Figure **5-3**: Optical absorption depth versus optical wavelength in GaAs [37].

Before illumination, the off-state resistance, R_{off}, is determined by the dark resistivity of the semiconductor material, ρ_0, as follows:

$$R_{off} = \frac{\rho_0 \cdot h_s}{w_s \cdot t_s}, \tag{5.1}$$

where h_s, w_s, and t_s are the switch gap length, width, and thickness, respectively.

5.1.2 Linear switching mode of PCSS

Depending on the operating biasing field and the optical energy received by the PCSS, the PCSS can be in one of two modes of operation: the linear mode or the nonlinear mode, as described below. In the linear mode, the number of generated electron–hole pairs is equal to the number of photons absorbed by the material. Therefore, in general, the conductivity of PCSS is linearly proportional to the intensity of incident radiation. In other words, the switch closes in direct response to the amplitude of the optical triggering pulse, remains conductive during illumination, and opens as soon as the pulse is removed, with a time constant of the carrier lifetime of the material. In addition, the triggering delay and jitter of the output current are considered to be 0 due to the ultra-short photon absorption time (i.e., the electron–hole pair generation time).

The timely response of conductivity in an optically triggered PCSS can be described by resistance as a function of time:

$$\frac{dn_e}{dt} = \frac{dn_h}{dt} = \frac{dn_c}{dt} = \frac{P_L}{\varepsilon_\lambda} \times \frac{1 - S_r}{h_s \cdot w_s \cdot d_0} - \frac{n_c}{\tau_r}, \tag{5.2}$$

where h_s is the switch (gap) length (distance between the metal contacts), w_s the switch width, d_0 is the absorption depth of the triggering optical pulse, and n_e and n_h are the excess concentration of the generated electrons and holes, respectively. Since they are generated in pairs, they are both equal and can be marked by n_c, the carrier concentration. P_L is the power of the incident optical pulse, S_r is the surface optical reflection coefficient, ϵ_λ is the photon energy, and τ_r is the carrier recombination time for both electrons and holes. The carrier concentration, as a function of time, from Eq. (5.2) can be rewritten as follows:

$$n_c(t) = e^{-t/\tau_r} \int_0^t e^{-t'/\tau_r} \left[\frac{P_L}{\varepsilon_\lambda} \times \frac{(1 - S_r)}{h_s \cdot w_s \cdot d_0} \right] dt'. \tag{5.3}$$

Assuming a rectangular optical pulse shape with a duration of T_0 and constant intensity of P_0, Eq. (5.3) becomes the following:

$$n_c(t) = \frac{P_L(1-S_r)\cdot\tau_r\cdot(1-e^{-t/\tau_r})}{\varepsilon_\lambda\cdot h_s\cdot w_s\cdot d_0}. \tag{5.4}$$

If the optical pulse duration, T_0, is much smaller than the carrier recombination time, τ_r, the exponential term in Eq. (5.4) can be approximated to $1-T_0/\tau_r$. Therefore,

$$n_c(t) = \frac{P_L(1-S_r)\cdot\tau_r\cdot T_0}{\varepsilon_\lambda\cdot h_s\cdot w_s\cdot d_0} = \frac{E_0(1-S_r)}{\varepsilon_\lambda\cdot h_s\cdot w_s\cdot d_0}, \tag{5.5}$$

where $E_0 = P_0T_0$ is the total incident optical energy. The conductivity, σ, of the semiconductor material is expressed as follows:

$$\sigma = qn_e\mu_e + qn_h\mu_h = qn_c(\mu_e+\mu_h), \tag{5.6}$$

where μ_e and μ_h are the mobility of generated electrons and holes, respectively, and q is the elementary charge. The on-state resistance, R_{on}, of the switch when it is triggered is expressed by the following equation:

$$R_{on} = \frac{h_s}{\sigma\cdot w_s\cdot d_0} = \frac{\varepsilon_\lambda h_s^2}{qE_0(\mu_e+\mu_h)(1-S_r)}. \tag{5.7}$$

In other words, the on-state resistance is independent of the width of the switch, w_s, and proportional to the square of the gap length, h_s.

After removal of the optical pulse on the PCSS at T_s, the carrier concentration starts to decay:

$$n_c(t) = N_0e^{-t/\tau_r}, \tag{5.8}$$

with $N_0 = n_c(T_s)$. Fig. 5-4 shows the temporal change in the resistance of a PCSS triggered by an optical pulse.

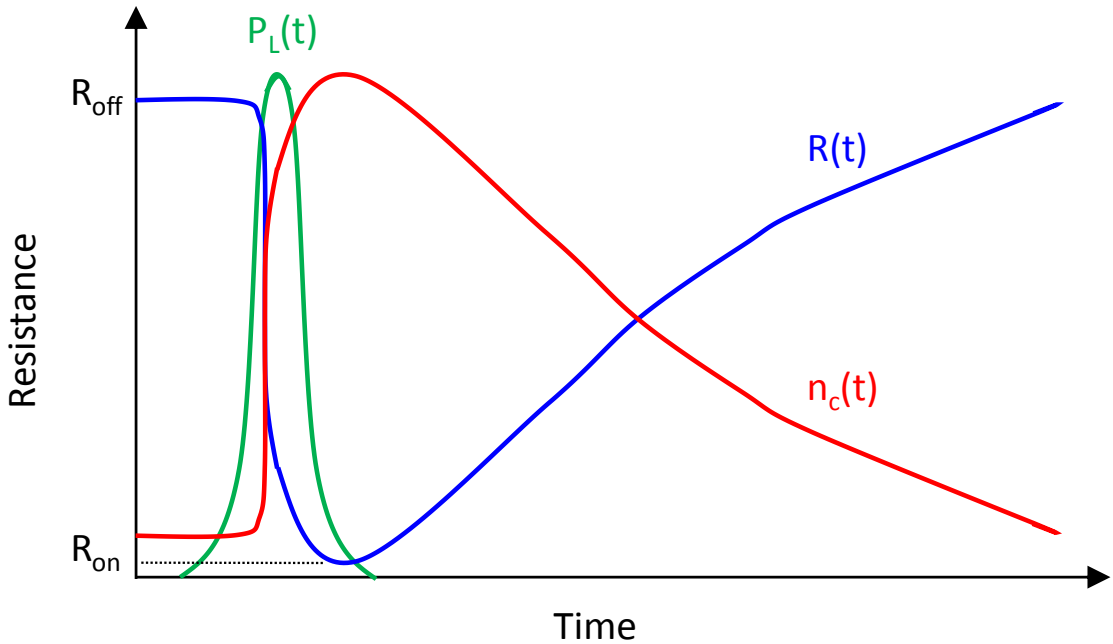

Figure **5-4**: Illustration of the temporal development of switch resistance, optical power, and carrier concentration in a PCSS.

If the PCSS is illuminated by a continuous wave (CW) optical source, generation and recombination of the carriers would reach equilibrium. The steady-state resistance can be expressed as follows:

$$R_{ss} = \frac{\varepsilon_\lambda h_s^{\,2}}{q\tau_r P_L(\mu_e + \mu_h)(1 - S_r)}\,. \tag{5.8}$$

When the recombination time, τ_r, is much less than the pulse duration, T_0, the excess carrier concentration can be approximated as follows:

$$n_c(t) = \frac{(1 - S_r)\cdot\tau_r}{\varepsilon_\lambda \cdot h_s \cdot w_s \cdot d_0} P_L(t)\,. \tag{5.9}$$

This is typically applicable in the case of a SI-GaAs PCSS, for which the carrier lifetime is usually less than or around 1 nanosecond and the pulse width triggering pulse is more than 5 ns.

5.1.3 Nonlinear switching mode of PCSS

The nonlinear mode, or high-gain mode, of PCSS occurs only in operations with very high biasing fields (>40 kV/cm). In this mode, the generated electron–hole pairs are no longer linearly proportional to the photons absorbed by the switch. Instead, the carriers are generated in an avalanche fashion; many more carriers are generated than the number of photons that are absorbed, resulting in a gain between the absorbed optical energy and induced electrical pulse. In other words, much lower optical energy is required to close the switch in the nonlinear mode than in the linear mode. The switching process in the nonlinear mode can be generally divided into three stages: the initiation phase, the sustaining (lock-on) phase, and the recovery phase.

It was found that once the threshold of the biasing field for the nonlinear mode is reached, the minimum triggering energy needed to initiate this mode is inversely proportional to the average field on the PCSS. In addition, the turn-on time of the switch is inversely proportional to the biasing field [37].

The second phase of the nonlinear mode is the lock-on phase. Unlike in the linear mode, in which resistance starts to rise once the optical pulse is gone, the switch stays conductive for a period of time because an excess number of generated carriers requires a much longer period to recombine before the current dissipates in the circuit. The length and amplitude of the lock-on field depends on the material as well as the circuit, which can last as long as microseconds after the optical pulse diminishes. It was found that the rise time of PCSS in the nonlinear mode can be significantly faster than the optical triggering pulse width because the rise time is inversely proportional to the average electric field on the PCSS [37]. In addition to the turn-on time and optical trigger threshold, a time delay in the lock-on phase was found to exist and to be inversely proportional to the applied field.

The final phase of the nonlinear mode is the recovery phase, which occurs when the dissipating current is no longer able to hold the lock-on phase and starts to disappear. This recovery process has always been very slow compared to linear switching.

Fig. 5-5 shows a typical nonlinear response of a PCSS. As shown, the switch remains conductive after the pulse is gone. For measurement, we probed the PCSS in series with a 50-kΩ load resistor, a DC high-power supply, and an oscilloscope. A 532-nm Q-switched Nd:YAG laser with a full width at half maximum (FWHM) of 5 ns was used in this experiment.

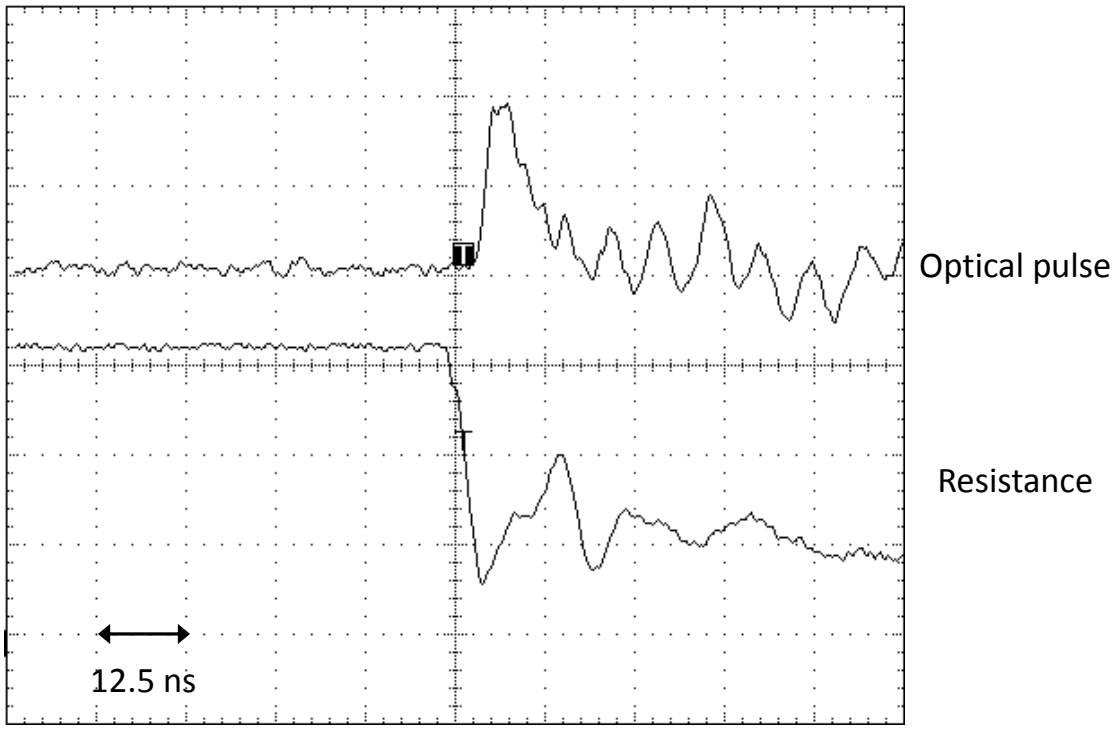

Figure **5-5**: Temporal response of the optical pulse and resistance of a PCSS in the nonlinear mode.

The nonlinear mode of PCSS suffers from the current filaments associated with the vigorous power-switching process. Repeatedly triggering the switch results in more and more

current filaments, which can cause irreversible damage, such as surface flashover or breakdown. However, this problem can be effectively suppressed by a surface coating of Al_2O_3.

In summary, the nonlinear switching mode of PCSS consists of three stages: initiation, sustaining (i.e., the lock-on phase), and recovery. The process of nonlinear switching involves many physical mechanisms and is so complicated that, although several theories regarding the working mechanisms have been proposed, the understanding of the nonlinear behavior in PCSS is still incomplete.

5.1.4 Comparison of switching modes of PCSS

To summarize the features of the linear and nonlinear switching modes of PCSS, the nonlinear mode requires a much higher electric field and much lower triggering energy to turn on the switch, implying that it involves current gain. In addition, it can be faster to turn on the switch in the nonlinear mode than in the linear mode. Further, it has a characteristic lock-on phase and slow recovery to a dark state. Due to the high density of energy in the nonlinear mode, current filaments often occur, causing damage to the surface of the PCSS.

5.2 Ultra-long lock-on phase in the non-linear switching mode

In the following sections, we report a new type of high-gain PCSS switching that features an ultra-long (e.g., on the order of millisecond) lock-on phase due to the integration of Si-GaAs and a ruby crystal.

As mentioned in Section 5.1, a PCSS functions by harnessing optical energy to produce charge carriers in the material to dramatically alter the resistivity of the material, thus causing the material to shift from an insulation state to a conductive state. The operation of SI-GaAs PCSS differs in the linear mode and non-linear mode depending on the optical triggering fluence and bias field. At a low triggering fluence and bias field, the PCSS is operated in the linear mode, and the exchange rate between the absorbed photons and the generated electron–hole pair is almost one to one. The switch turns on once the triggering pulse hits the material and the resistance of the switch is inversely proportional to the number of photons in the pulse. As soon as the pulse ends, the switch has a high resistance again. However, in the presence of a sufficiently high electric field as well as triggering fluence, the switch is operated in the non-linear, or high-gain, mode, which produces an avalanche effect; instead of generating just one electron–hole pair from one photon, a chain reaction occurs, resulting in the generation of many more charge carriers almost immediately. It is believed that the tremendous amount of charge carriers would fill up all spaces in the material, and because the carriers are generated faster than they can recombine, the switch enters a lock-on phase for a period of time. That is, the switch remains conductive even after the triggering pulse ends, rather than immediately resuming its off state, like in the linear switching mode. The amount of space in which charge domains can form is determined by the dimensions of the device. The switch starts to recover to its initial state when the carriers recombine faster than they are generated and eventually resumes its open state when they deplete. It has been found that this behavior is independent of the switch length, initial provided voltage, and triggering energy as long as the

minimum requirement for it to occur is fulfilled [91]. It is believed that multiple mechanisms may play a role in generating the carriers required to sustain the lock-on phase, although there is no complete, uncontroversial physical explanation. Numerous theories have been proposed to describe this behavior, such as band-to-band ionization, negative differential mobility (NDM) of the electrons in GaAs, the Gunn effect, double-injection, and a combination of trapping and band impact ionization, moving electric fields, and photon recycling [44, 92–94].

Even though the details concerning the lock-on mechanism are still under debate, it is clear that a minimum charge density is required to maintain the lock-on state, a PCSS can be treated as a Gunn device when operating in the non-linear mode [44], and the space charge density with respect to time in the active area of PCSS can be expressed as follows:

$$\rho(t) = \rho_0 e^{-t/t_R}, \tag{5.15}$$

where ρ_0 is the initial electron density, e is the electron charge, and t_R is the dielectric relaxation time, which can be expressed as follows:

$$t_R = \frac{\varepsilon}{en|\mu|}, \tag{5.16}$$

where ε is the permittivity of GaAs, n is the electron density, and μ is the average electron mobility of GaAs. It has been found that, for the space charge domain formed in the triggered PCSS to be stable, the transit time required for the charge domain to move from the cathode to the anode, given by $\tau = l/vs$, has be larger than t_R. We thus obtain the following equation:

$$\frac{l}{v_s} > \frac{\varepsilon}{en|\mu|}, \tag{5.17}$$

where l is the length of the active area of PCSS between the electrodes and v_s is the saturation velocity of electron in GaAs. Eq. (5.17) can be rewritten as follows:

$$n \times l > \frac{v_s \varepsilon}{e|\mu|} \approx 10^{12}\, cm^{-2}, \tag{5.18}$$

by inserting typical values of GaAs parameters, including $v_s = 1\times10^7$ cm/s, $\varepsilon = 13.18\times8.85\times10^{-12}$ $C^2N^{-1}m^{-2}$, μ=-2000 cm^2/V, and $e=1.6\times10^{-19}$ C. Eq. (5.18) provides the critical condition for the PCSS to maintain the lock-on phase. Once the charge density falls below this requirement, the PCSS starts to recover to its open state. To maintain the minimum required charge density, in this study we develop a new type of PCSS consisting of a SI-GaAs substrate and a front-bonded ruby crystal. The 532-nm laser pulses from an Nd-YAG laser shoot on the front surface of the ruby crystal. A portion of the laser pulse passes through the crystal, reaching the GaAs substrate, and the remaining portion of the laser pulse is absorbed by the ruby crystal. This results in emission of 694-nm fluorescent light, a portion of which also reaches the GaAs substrate. A high-fluence 532-nm short laser pulse with a pulse width of about several nanoseconds is used to cause the PCSS to enter its high-gain non-linear mode. In contrast, low-fluence, long-lifetime (i.e., on the order of milliseconds) 694-nm fluorescent light is used to generate the minimum charge density required to maintain the lock-on state.

5.3 Experimental results and discussion

In our experiment, a PCSS with a typical lateral configuration was fabricated. First, a SI-GaAs wafer with a resistivity of about 7×10^8 Ω-cm was well-lapped and polished. Second, a photoresistant mask was placed on top of the polished surface by optical lithography. Third, a pair of titanium/gold electrodes were placed on the patterned GaAs substrate. Finally, the remaining photoresist was removed. The gap between the two electrodes of the fabricated PCSS was 0.5 mm, and the electrodes were 2 mm wide. A 532-nm Nd-YAG Q-switch pulsed laser with a 5-ns pulse duration was used to trigger the PCSS. The 532-nm wavelength was selected for the following reasons: (1) the photon energy at the 532-nm wavelength is greater than the bandgap of GaAs, so it can effectively trigger the PCSS; (2) it is within the excitation wavelength range of the ruby crystal; and (3) it is a widely available laser wavelength that is available in our lab. A common ruby rod was cut and polished into a 2 mm × 2.5 mm × 4.5 mm cuboid, as shown in Fig. 5-10(a). The 2 mm × 2.5 mm face was placed between the PCSS electrodes shielding the gap area, as shown in Fig. 5-10(b). Norland optical adhesive was used to fill the space between the ruby and the PCSS, fixing the configuration while preventing electrical breakdown through air. Fig. 5-11 shows the configuration of the PCSS sample and the circuitry used to measure its performance.

(a)

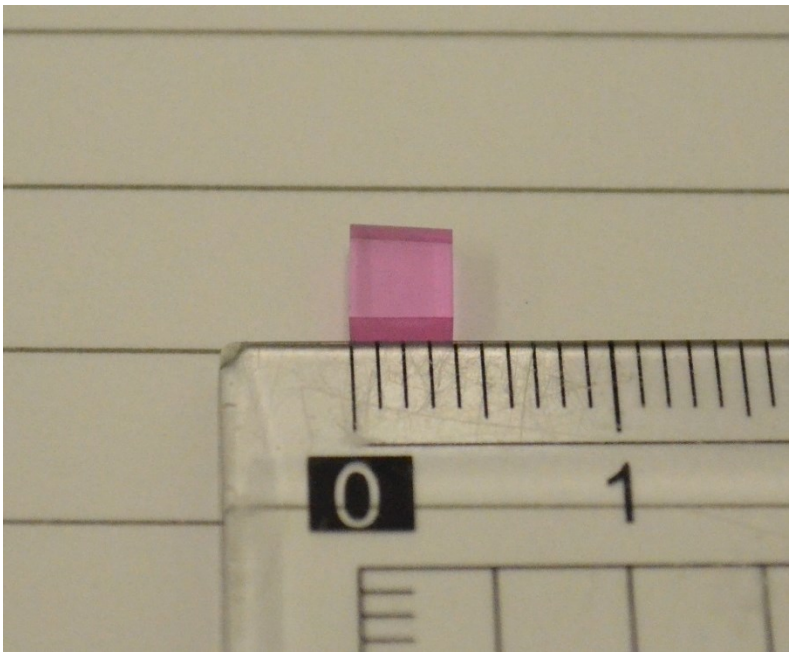

(b)

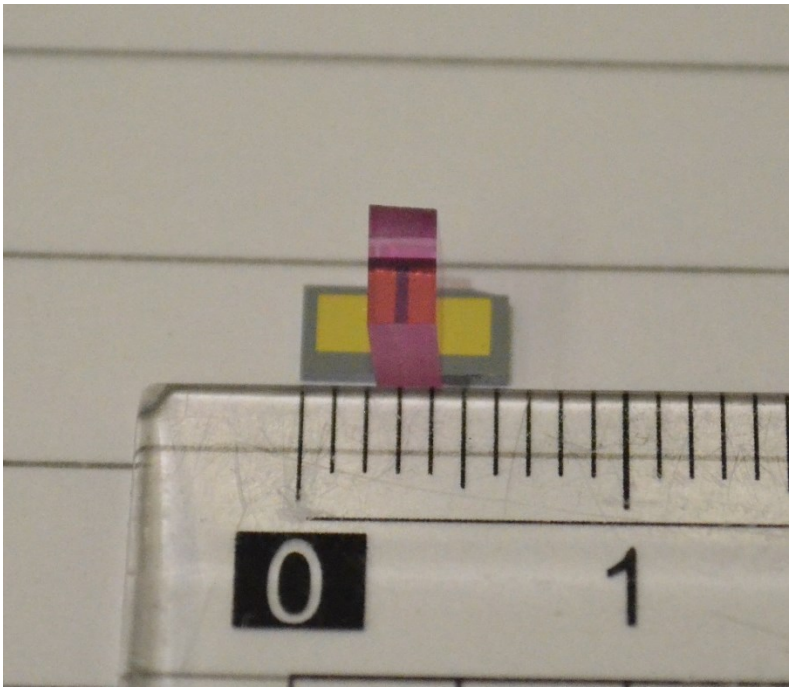

Figure **5-6**: Photos of (a) a polished ruby cuboid and (b) the PCSS bonded with the ruby crystal.

(a)

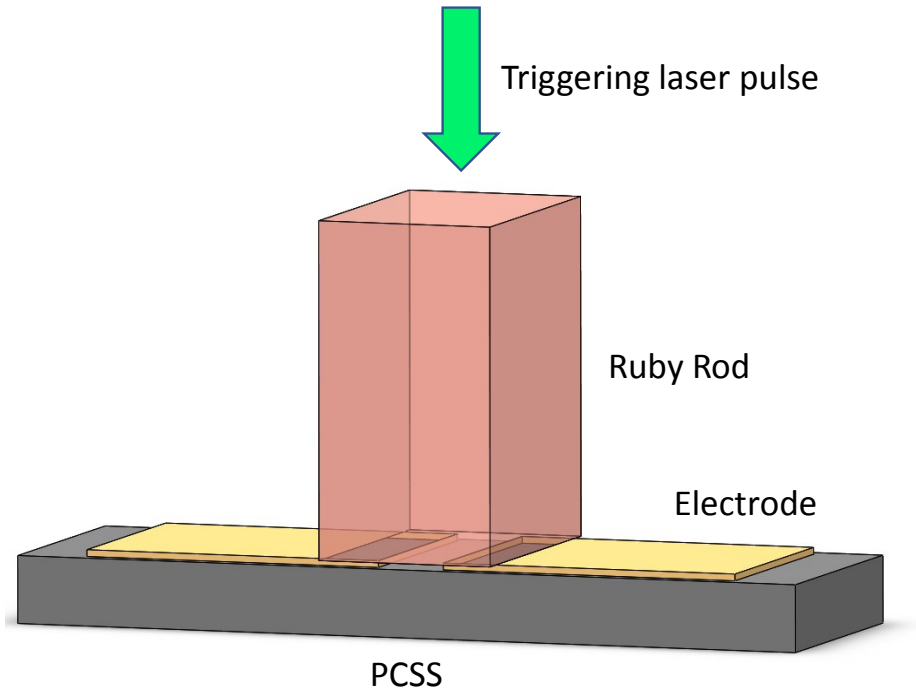

(b)

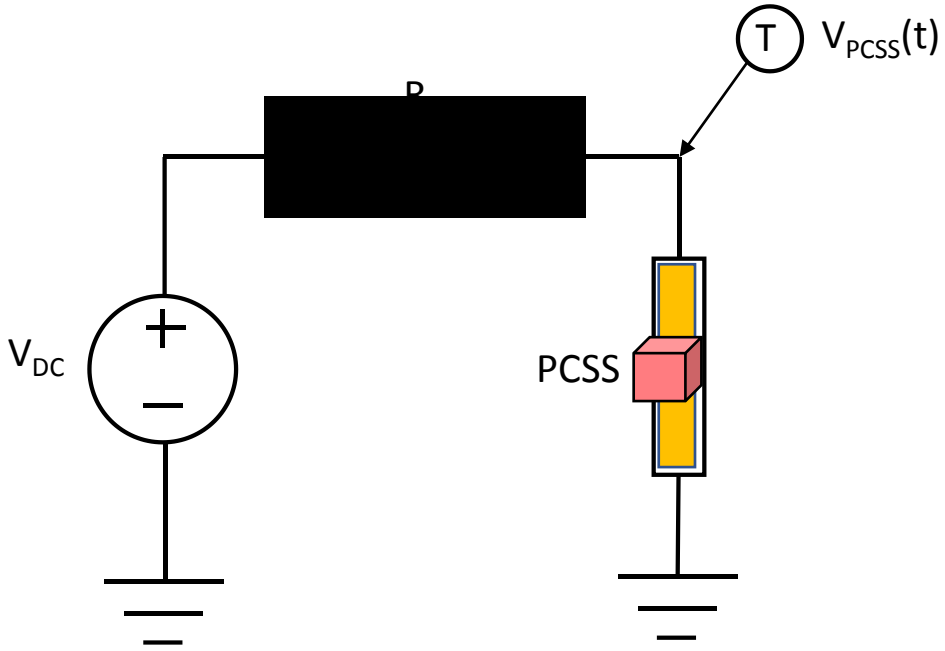

Figure **5-7**: Illustrations of (a) the configuration of the PCSS with a ruby and (b) the measurement setup.

The PCSS was connected in series with a DC voltage source and a 150-kΩ load resistor, R_L. This resistance was chosen as it is sufficiently smaller than the dark-state resistance of the PCSS (>5 GΩ) and sufficiently larger than the on-state resistance. A testing probe was placed between the R_L and the PCSS to measure the response of voltage across the PCSS. The time-dependent voltage response of the PCSS in the circuit is described by the following equation:

$$V_{PCSS}(t) = V_{DC} \frac{R_{PCSS}(t)}{R_{PCSS}(t) + R_L}. \tag{5.19}$$

For the purpose of comparison, we conducted an experiment with a high-gain PCSS and without a ruby crystal. We started by measuring the time-dependent voltage drop across the PCSS, which was operating in the non-linear mode. To ensure that measurement was performed when the PCSS was in its non-linear mode, an excessively large biasing field (60 kV/cm) and single-shot triggering energy (2.2 mJ) were introduced to the PCSS during the experiment. Fig. 5-12(a) shows the initial phase of non-linear switching. We believe that the PCSS worked in the nonlinear mode because, in the linear mode, the response of PCSS follows the pulse shape of the laser. Since the pulse width used in our experiment was around 5 ns, the response time of PCSS would also be around 5 ns if it were in the linear mode. However, the measured response time, as shown in Figs. 5-12 and 5-13, was much longer than 5 ns, and thus the PCSS was undoubtedly in the nonlinear mode in our experiment. The PCSS initially holds the majority of the voltage drop in the circuit at the off-state, and upon being triggered, the voltage across the PCSS immediately drops below zero (the solid line) and exhibits a little oscillation, in line with the non-linear responses reported in prior studies. Fig. 5-12(b) shows that the PCSS stayed in the lock-on phase for nearly 3 μs shortly after triggered and then recovered to the off-state within several microseconds. Fig. 5-12(c) confirms

that the V_{PCSS} was activated and responded in a timely manner at a large time scale. The maximum lock-on time of the PCSS without a ruby crystal was on the order of microseconds.

Second, we conducted the same measurements of the high-gain PCSS with a ruby crystal. Fig. 5-13 shows the result of triggering the PCSS with a ruby cuboid at the top of the illuminated area. Since the emission wavelength of ruby is 694 nm, the PCSS was illuminated by a combination of the 532-nm and 694-nm wavelengths. In this part of experiment, we ensured that the triggering energy of the 532-nm radiance was kept at 2.2 mJ after passing through ruby to obtain consistent results. In Fig. 5-13(a), a pulse very much like the one in Fig. 5-12(a) was measured, indicating that the triggering stage of the PCSS in both cases were similar. However, the switch started to act quite differently at a larger time scale. Unlike in Fig. 5-12(b), in which the pulse started to recover within 3 μs, the pulse in Fig. 5-13(b) stayed in the lock-on state for more than 10 μs. Additionally, as shown in Fig. 5-13(c), instead of starting to recover to the off-state, the resistance of PCSS seemed to be further reduced at a relatively slow speed. The voltage drop across the PCSS reached its minimum within nearly 200 μs and was sustained for nearly a millisecond, as shown in Fig. 5-13(d). Fig. 5-13(e) shows the PCSS before it started to recover from the sustaining phase. Finally, Fig. 5-13(f) shows that the PCSS recovered to its initial off state within 15 ms. The length of the lock-on time matches the fluorescent lifetime of a ruby crystal, which is also on the order of milliseconds. Thus, we achieved an ultra-long lock-on time (i.e., on the order of milliseconds) that was three orders of magnitude longer than when the fluorescent effect of ruby crystal was not harnessed.

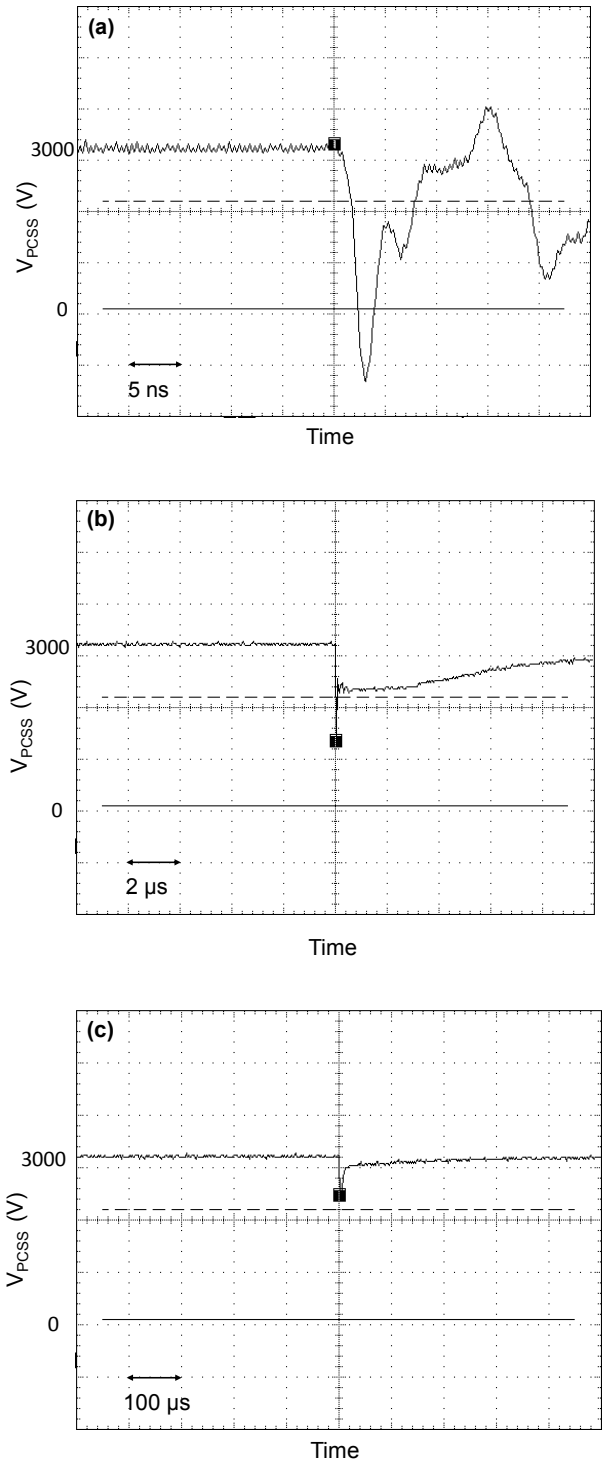

Figure **5-8**: Measured temporal response of the voltage across PCSS without the influence of a ruby at (a) 5-ns, (b) 2-μs, and (c) 100-μs scales.

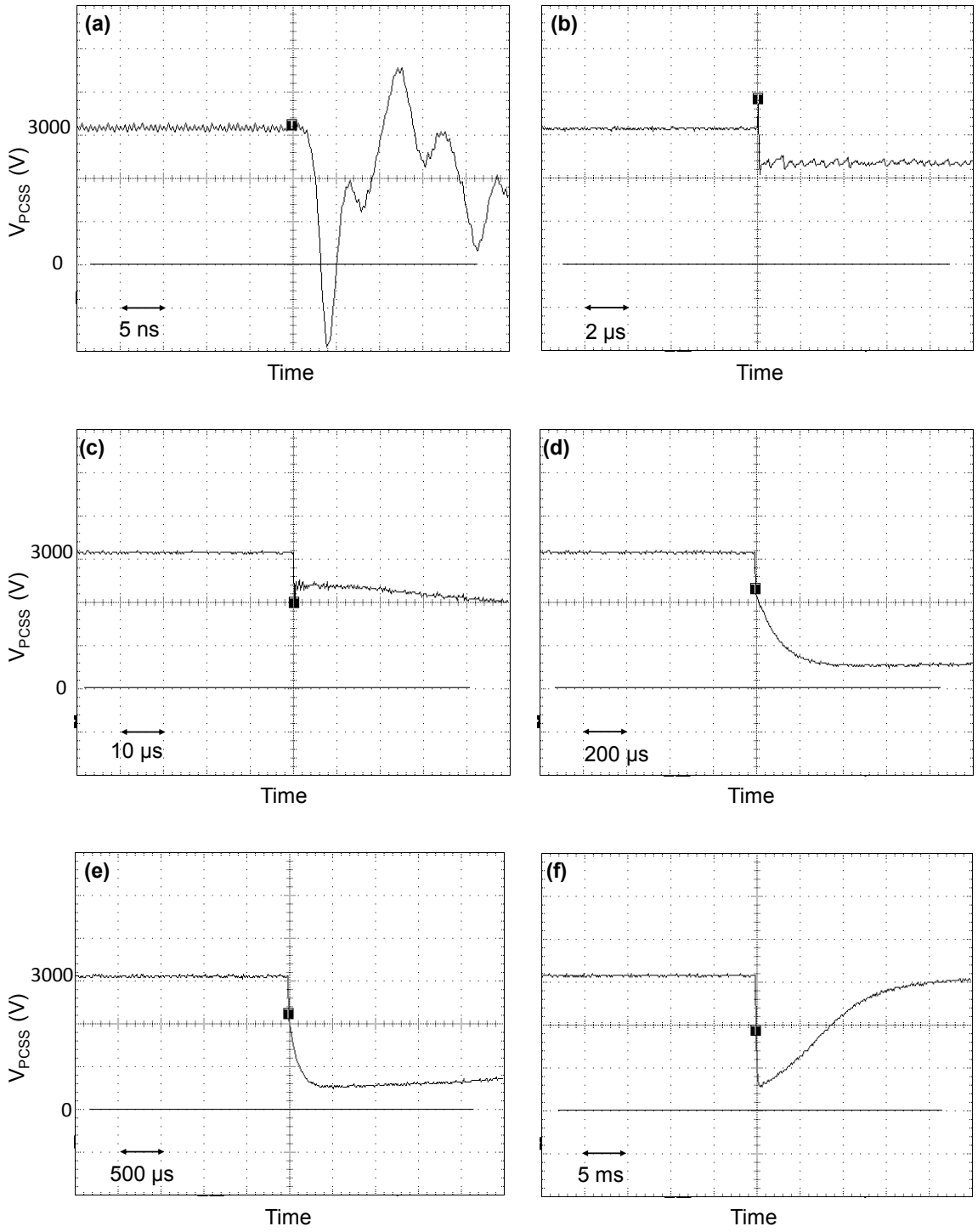

Figure **5-9**: Measured temporal response of the voltage across PCSS with the influence of a ruby at (a) 5-ns, (b) 2-µs, (c) 10-µs, (d) 200-µs, (e) 500-µs, and (f) 5-ms scales.

We believe that the working principle in our experiments is that much less light intensity is required to maintain the lock-on state than when the PCSS is triggered to shift from an insulating state to a conductive state. The minimum triggering light intensity can be determined based on the minimum pulsed laser fluence. As reported in [95], the minimum triggering fluence is 10 μJ/cm^2 for a laser beam with a pulse duration of 5 ns. Then, the required light triggering intensity, I_t, is as follows:

$$I_t = \frac{10x10^{-6}}{5x10^{-9}} = 2000W / cm^2 . \tag{5.20}$$

The minimum light intensity required to maintain the lock-on state can be estimated with the following logic. Since the fluorescence lifetime of a ruby is long (>10 ms), we can assume that fluorescent illumination occurs continuously. In this case, the total number of photons, N, received by GaAs can be derived from the following equation:

$$N = \frac{\eta P \tau}{E_p}, \tag{5.21}$$

where η is the quantum efficiency of GaAs, P is the fluorescence power, τ is the relaxation time of the charge carrier in a conductive state, and E_p is the single photon energy. Based on previous studies' results, η and τ can be assumed to be 0.5 [96] and 1 ns [97], respectively. Additionally, $E_p = 2.9x10^{-19}J$ can be assumed at a wavelength of 694 nm. The photogenerated charge density can be derived from the following equation:

$$n = \frac{N}{wld} = \frac{\eta P \tau}{wldE_p}, \tag{5.22}$$

where $w \cdot l$ represents the beam size and d is the effective penetration depth of fluorescent light in a GaAs wafer. Based on [44], the minimum charge density required to maintain the lock-on state is determined as follows:

$$n \times l = \frac{\eta P \tau}{w d E_p} = 10^{12} cm^{-2} . \tag{5.23}$$

The minimum required light intensity, I_m, can be obtained with the following equation:

$$I_m = \frac{P}{wl} = \frac{10^{12} d \cdot E_p}{\eta \tau l} . \tag{5.24}$$

Substituting d = 2 μm, $E_p = 2.9x10^{-19}J$, η = 0.5, τ = 1 ns, and l = 0.05 cm into Eq. (5.24), we obtain I_m = 2.32 W/cm^2, which is three orders of magnitude smaller than the result for I_t. Thus, a much lower light intensity is required to maintain the lock-on state. Since the lifetime of fluorescence is long (>10 ms; near-continuous illumination) and a very low light intensity is required to maintain the lock-on state, as described above, an ultra-long (>10 ms) lock-on time can be achieved.

5.4 Conclusion

In this chapter, we reviewed the basic characteristics of PCSS and reported the application of PCSS to a KTN beam deflector. We reported a new type of PCSS that combines a fluorescent ruby crystal and a SI-GaAs substrate, and we calculated the power required to activate the non-linear mode and maintain the lock-on phase. The PCSS was illuminated by both high-fluence 532-nm short laser pulses and low-fluence, long-lifetime 694-nm fluorescent light. The high-fluence laser pulse enabled the PCSS to enter the high-gain conductive mode, and the low-fluence fluorescent light was used to generate carriers to achieve the minimum charge density. Due to the long lifetime of the fluorescent light, an ultra-long lock-on time (i.e., on the order of milliseconds) was successfully achieved. The measured lock-on time was three orders of magnitude longer than that of a conventional Si-GaAs-based PCSS. A PCSS with an ultra-long lock-on time can be very useful for some applications, such as firing sets.

Chapter 6

Conclusions and Future Works

This dissertation was intended to produce deep, novel findings regarding the unknown aspects of KTN beam deflectors. We contributed to the theory of SCC KTN beam deflection by analyzing a non-uniform SCC beam deflector. The potential of KTN beam deflectors in different applications was broadened by our development of a 2-D KTN beam deflector in which both SCC and temperature control occur simultaneously on a single crystal. In addition to beam deflection, the technique of laser activation with PCSS, which is useful in KTN beam deflectors, was enriched by our discovery of a prolonged lock-on phase in the non-linear switching mode of PCSS. The studies were thoroughly described in previous chapters and are summarized in the following paragraphs.

The dissertation began with a review of information about KTN, including its preparation, physical properties, and unique features (e.g., its electrical, optical, EO, and thermal characteristics). It is a special material because it has the largest EO coefficient ever reported and possesses a variety of malleable features. Most of these properties are the result of its nature as a perovskite crystal, a relaxor ferroelectric, and a solid solution of $KTaO_3$ and $KNbO_3$.

In Chapter 3, the electric field distribution and deflection angle in a non-uniform SCC KTN beam deflector were quantitatively analyzed and experimentally verified. A physical model was proposed to depict the distribution of the non-uniform space charge, which can generally be divided into three parts. The experimental results exhibited a similar trend as the proposed model. Hence, the approach used to analyze the KTN beam deflector in this study seems to be good.

In Chapter 4, 2-D KTN beam deflection was successfully achieved by combining two deflecting mechanisms—SCC beam deflection and temperature-gradient-controlled beam deflection—in the x and y directions, respectively. By applying an external biasing field in the x

direction and inducing a temperature gradient in the y direction on a KTN single crystal, deflection was observed in both directions. The effects of the space-charge and temperature-gradient mechanisms were quantitatively analyzed and experimentally confirmed. Furthermore, high-speed (~80 ns) deflection capability was experimentally demonstrated. The maximum difference between the experimental results and theoretical analyses was around 7%.

In Chapter 5, voltage modulation was introduced to a PCSS. SCC KTN beam deflection occurred on the order of nanoseconds when measured with PCSS. This confirmed that the scanning speed of the SCC beam deflector is mainly limited by the speed of the driving source, not the EO effect. With proper voltage modulation, an ultra-fast beam deflector (within MHz to GHz) can be developed, which could be very useful for many applications, such as real-time swept-source-based low-coherence tomography. In the second part of the chapter, a new type of PCSS was developed by combining a fluorescent ruby crystal and a SI-GaAs substrate, and the power requirements for activating the non-linear mode and maintaining the lock-on phase were calculated. The PCSS was illuminated by both high-fluence 532-nm short laser pulses and low-fluence, long-lifetime 694-nm fluorescent light. The high-fluence laser pulses enabled the PCSS to enter its high-gain conductive mode, and the low-fluence fluorescent light was used to generate the carriers needed to achieve the minimum charge density. Due to the long lifetime of the fluorescent light, an ultra-long lock-on time (i.e., on the order of milliseconds) three orders of magnitude longer than that of the conventional Si-GaAs-based PCSS was achieved. A PCSS with an ultra-long lock-on time can be very useful in some applications, such as firing sets. Overall, although the findings in this study contribute to the field of beam steering technology, there is still much to explore regarding the applications of KTN.

Although the findings in this study has progressively expanded the boundary of science in the field of beam steering technology, there remains much potential to be discovered and questions to be answered regarding the applications of KTN material.

In addition to temperature-gradient-controlled beam deflection, another beam deflection mechanism, composition-gradient-controlled (CGC) beam deflection was discovered in a previous study [98]. The centration ratio of Ta and Nb atoms in KTN crystal can be controlled during the growth process such that a gradient distribution is formed. CGC beam deflection functions similarly to TGC beam deflection, except the gradient of the refractive index is induced by the inherent composition gradient of the concentration ratio of Ta and Nb atoms in the crystal. Therefore, the Curie temperature of the crystal becomes a function of position corresponding to the composition gradient distribution in the crystal.

The deflection angles produced by TGC and CGC beam deflection exhibit similar physical characteristics. Like TGC beam deflection, CGC beam deflection does not function by itself; rather, it must coexist with SCC beam deflection. When the composition gradient of the KTN crystal is perpendicular to the external biasing field, the deflection angles in the x and y direction can be expressed as follows:

$$\theta_x = -Ln^3 g_{11}\varepsilon(y)^2 E_x \frac{\partial E_x}{\partial x} - Ln^3 g_{12}\varepsilon(y)^2 E_y \frac{\partial E_y}{\partial x}, \tag{6.1a}$$

$$\theta_y = -Ln^3 \left[g_{11}\varepsilon(y)\frac{d\varepsilon_r(y)}{dy} E_x{}^2 + g_{11}\varepsilon(y)^2 E_x \frac{\partial E_x}{\partial y} + g_{12}\varepsilon(y)\frac{d\varepsilon_r(y)}{dy} E_y{}^2 + g_{12}\varepsilon(y)^2 E_y \frac{\partial E_y}{\partial y} \right], \tag{6.1b}$$

where L, n, g_{11}, and ε are the beam propagation length, refractive index, EO coefficient, and permittivity, respectively.

Combining the SCC, TGC, and CGC beam deflection mechanisms can result in an ultra-fast varifocal 2-D KTN beam deflector. Fig. 6-1 illustrates the design of such a deflector. Two pairs of metal strips are deposited on the top and bottom faces of a KTN crystal along the z

direction to power the device. A pair of temperature-controlling modules surrounding the crystal in the x direction induces a temperature gradient, and the crystal has an inherent composition gradient in the y direction. As a result, a laser beam entering the crystal in the z direction would be subjected to TGC and CGC beam deflection and the SCC varifocal effect within a single device. Due to the superior speed offered by KTN, the device is expected to work at the MHz level or higher, which could be very useful in beam scanning technology.

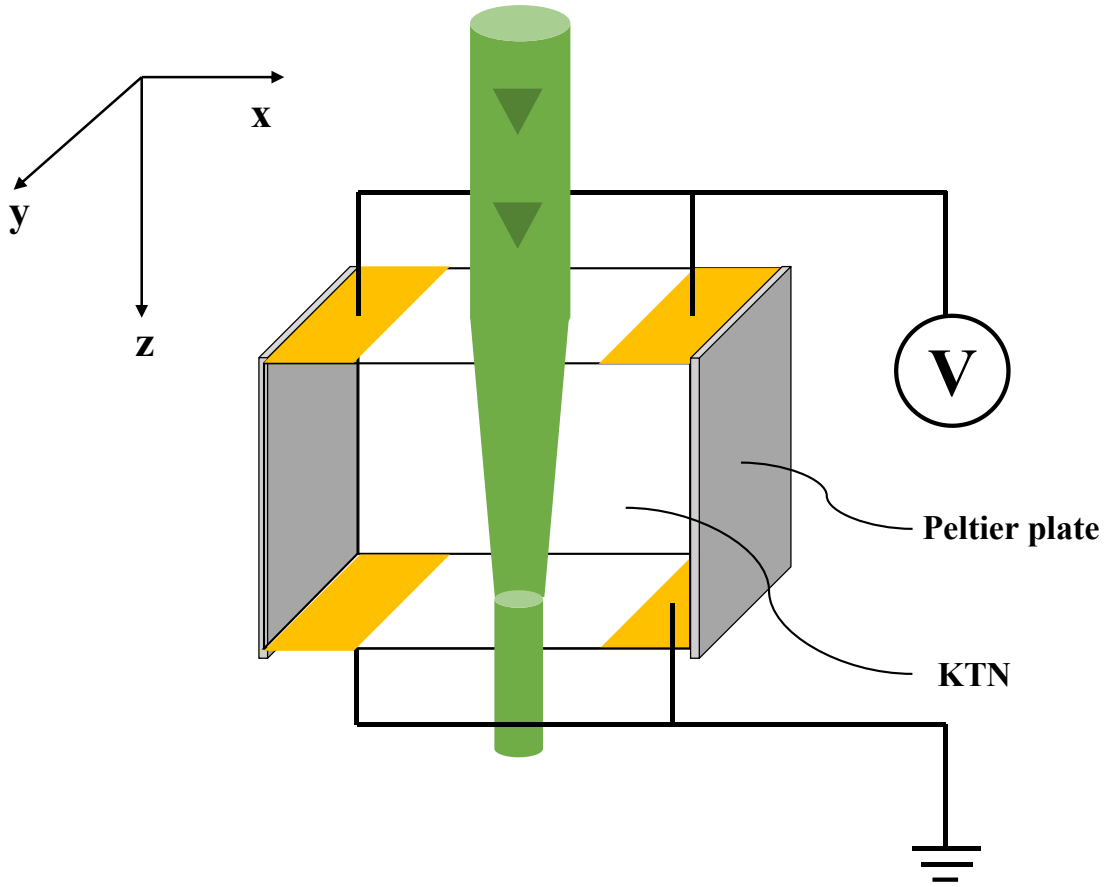

Figure **6-1**: Configuration of a varifocal 2-D KTN beam deflector.

Other than for beam deflection, the SCC EO effect in KTN can be utilized to create optical devices, such as a transmission grating with a tunable refractive index. Refractive index modulation via the non-linear EO effect in a SCC KTN crystal is described by the following equation:

$$\Delta n(x) = -\frac{1}{2} n^3 g_{11} \varepsilon^2 E(x)^2$$

$$= -\frac{1}{2} n^3 g_{11} e^2 N^2 \left(x - \frac{d}{2} + \frac{\varepsilon V}{eNd} \right)^2, \tag{6.2}$$

where x is the position in the direction of the electrodes, n is the refractive of KTN, g_{11} is the Kerr coefficient, ε is the dielectric constant, N is the space charge density, d is the distance between electrodes, and V is the driving voltage. According to the equation, SCC KTN crystal has a graded refractive index along the direction of the electrodes.

A previous study found that the amount of preinjected space charge depends on the applied electric field [99]. Therefore, the refractive index can be modulated by adjusting the voltage applied to a SCC KTN crystal, and a KTN-based transmission phase grating with a tunable index can be developed. The grating equation for a typical transmission phase grating can be written as follows:

$$n_{trn} \sin\left[\theta(m)\right] = n_{inc} \sin\theta_{inc} - m\frac{\lambda_0}{\Lambda_x}, \tag{6.3}$$

where n_{trn} and n_{inc} are the refractive indices of the transmission and incident regions, respectively; m is the diffraction mode, θ_{inc} is the incident angle, λ_0 is the wavelength of incident radiation, and Λ_x is the grating period. The grating equation can be reduced to the following:

$$n_{ktn} \sin\left[\theta(m)\right] = -m \frac{\lambda_0}{\Lambda_{ktn}}, \tag{6.4}$$

where n_{ktn} and Λ_{ktn} are the refractive index and grating period of the KTN crystal, respectively. The total number of possible diffracted modes, M, of the grating is determined as follows:

$$M = \frac{2n_{ktn}\Lambda_{ktn}}{\lambda_0} + 1. \tag{6.5}$$

Based on Eqs. (6.2) and (6.5) and by performing refractive index modulation of a SCC KTN crystal through a biasing field, we can effectively modulate the diffraction of the grating. Fig. 6-2 shows a conceptual drawing of a 1-D transmission phase grating made with a SCC KTN crystal. The other possible functionality of this device that is worth exploring is based on a recent finding in KTN materials. Di Mei et al. recently discovered of a giant refraction index in a KTN crystal doped with Li (KTN:Li crystal) [99]. In their report, a broadband index of refraction as large as 26 was observed in a KTN:Li crystal at its Curie temperature. In addition, field-induced phase transition on KTN crystals, which allows KTN crystals to undergo phase transition from the cubic phase to the ferroelectric phase with a sufficient applied electric field, was reported in previous studies [29, 85]. Therefore, in principle, this giant refractive index can be induced by applying the proper electric field to KTN crystals without changing the working temperature, which can be very useful in building EO devices with a tunable refractive index feature.

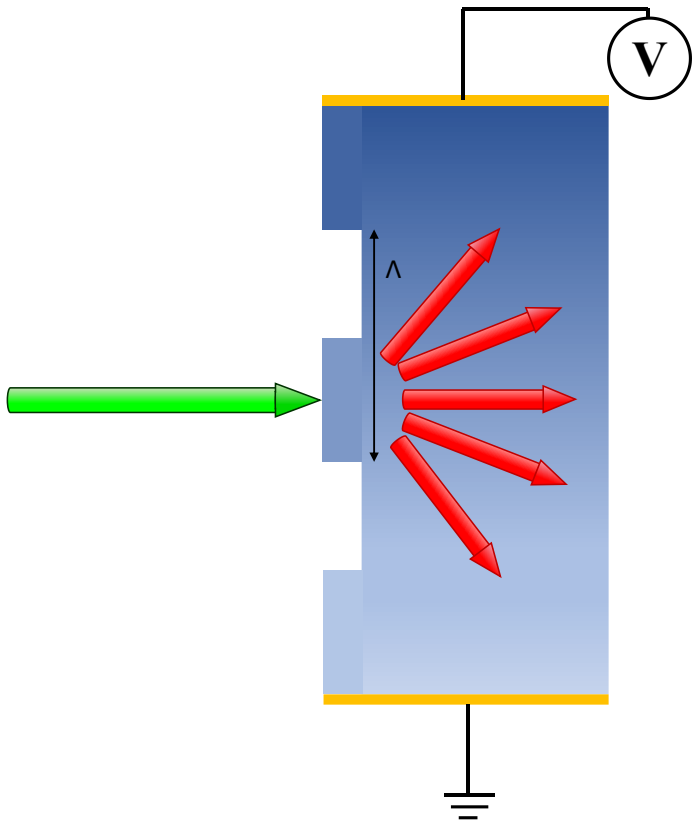

Figure **6-2**: Conceptual drawing of a 1-D transmission phase grating of an SCC KTN deflector with a normal incident beam.

References

1. Y. Okabe, Y. Sasaki, M. Ueno, T. Sakamoto, S. Toyoda, S. Yagi, K. Naganuma, K. Fujiura, Y. Sakai, J. Kobayashi, and K. Omiya, "200 kHz swept light source equipped with KTN deflector for optical coherence tomography," *Electron. Lett.* **48**(4), 201–202 (2012).
2. D. E. Holmgren, and W. Robinett, "Scanned laser displays for head mounted displays," *University of North Carolina Department of Computer Science Technical Report*, TR92-029 (1992).
3. K. Kobayashi, K. Akiyama, I. Yoshizawa, and T. Asakura, "Laser-beam scanning system using an acoustic-optic deflector: its application to fundus imaging," *Meas. Sci. Technol.* **1**(2), 151 (1990).
4. L. Sun, J. Kim, C. Jang, D. An, X. Lu, Q. Zhou, J. M. Taboada, R. T. Chen, J. J. Maki, S. Tang, H. Zhang, W. H. Steier, C. H. Zhang, and L. R. Dalton, "Polymeric waveguide prism-based electro-optic beam deflector," *Opt. Eng.* **40**, 1217–1222 (2001).
5. G. Zhou, F. Mok, and D. Psaltis, "Beam deflectors and spatial light modulators for holographic storage application," *Holographic Data Storage*, H. J. Coufal, Springer (2000).
6. Y. Ishizuka, "Rotary polygon mirror type light deflector," *United States Patent* US5933267 (1999).
7. W. Y. Oh, S. H. Yun, G. J. Tearney, and B. E. Bouma, "115 kHz tuning repetition rate ultrahigh-speed wavelength-swept semiconductor laser," *Opt. Lett.* **30**, 3159-3161 (2005).
8. Y. Mao, S. Chang, E. Murdock, and C. Flueraru, "Simultaneous dual-wavelength-band common-path swept-source optical coherence tomography with single polygon mirror scanner," *Opt. Lett.* **36**, 1990-1992 (2011).

9. H. Miyajima, N. Asaoka, T. Isokawa, M. Ogata, Y. Aoki, M. Imai, O. Fujimori, M. Katashiro, and K. Matsumoto, "A MEMS electromagnetic optical scanner for a commercial confocal laser scanning microscope," *J. Microelectromech. Syst*. **12**, 243 (2003).

10. H. Ra, W. Piyawattanametha, Y. Taguchi, D. Lee, M. J. Mandella, and O. Solgaard, "Two-dimensional MEMS scanner for dual-axes confocal microscopy," *J. Microelectromech. Syst*. **16**, 969 (2007).

11. A. Wolter, S.-T. Hsu, H. Schenk, and H. Lakner, "Applications and requirements for MEMS scanner mirrors," *Proc. SPIE* **5719**, 64 (2005).

12. V. Bodlaj, "Piezoelectric beam deflector," *United States Patent* US3902783 (September 2, 1975).

13. F. Filhol, E. Defay, C. Divoux, C. Zinck, and M.-T. Delaye, "Piezoelectric micromirrors for fast optical scanning with large angular deflection," *Proc. IEEE-LEOS Conf. Opt. MEMS* **2004**, 190 (2004).

14. D. O. Harris and A. VanderLugt, "Acousto-optic photonic switch," *Opt. Lett*. **14**, 1177 (1989).

15. X. Lv, C. Zhan, S. Zeng, W. R. Chen, and Q. Luo, "Construction of multiphoton laser scanning microscope based on dual-axis acousto-optic deflector," *Rev. Sci. Instrum*. **77**, 046101 (2006).

16. A. W. Warner, D. L. White, and W. A. Bonner, "Acousto-optic light deflectors using optical activity in paratellurite," *J. Appl. Phys*. **43**, 4489 (1972).

17. V. J. Fowler, C. F. Buhrer, and L. R. Bloom, "Electro-optic light beam deflector," *Proc. IEEE* **52**, 193 (1964).

18. S. Hisatake, K. Shibuya, and T. Kobayashi, "Ultrafast traveling-wave electro-optic deflector using domain-engineered $LiTaO_3$ crystal," *Appl. Phys. Lett*. **87**, 081101 (2005).

19. G. R. B. E. Römer and P. Bechtold. "Electro-optic and acousto-optic laser beam scanners." *Physics procedia* **56,** 29-39 (2014).

20. Y. Amnon and Y. Pochi, *Optical waves in crystals: propagation and control of laser radiation,* Wiley Interscience (1984).

21. T. Imai, M. Sasaura, K. Nakamura, and K. Fujiura, "Crystal growth and electro-optic properties of $KTa_{1-x}Nb_xO_3$," *NTT Tech. Rev*. **5**, 1 (2007).

22. S. Toyoda, K. Fujiura, M. Sasaura, K. Enbutsu, A. Tate, M. Shimokozono, H. Fushimi, T. Imai, K. Manabe, T. Matsuura, and T. Kurihara, "Low-driving-voltage electro-optic modulator with novel $KTa_{1-x}Nb_xO_3$ crystal waveguides," *Jpn. J. Appl. Phys*. **43**, 5862 (2004).

23. Y. Sasaki, "High-speed spectrometer using KTN optical beam scanner," *NTT Tech. Rev*. **7**, 1 (2009).

24. Y.-C. Chang, C.-M. Lin, J. Yao, C. Wang, and S. Yin, "Field induced dynamic waveguides based on potassium tantalate niobate crystals," *Opt. Express* **20**, 21126 (2012).

25. Y.-C. Chang, C. Wang, S. Yin, R. C. Hoffman, and A. G. Mott, "Kovacs effect enhanced broadband large field of view electro-optic modulators in nanodisordered KTN crystals," *Opt. Express* **21**, 17760 (2013).

26. Y.-C. Chang, W. Zhu, J.-H. Chao, S. Yin, R. C. Hoffman, A. G. Mott, and C. Luo, "Super broadband ultrafast waveguide switches based on dynamic waveguiding effect," *Proc. SPIE* **9200**, 92000X (2014).

27. T. Sakamoto, S. Toyoda, M. Ueno, and J. Kobayashi, "High-speed optical beam scanning using KTN crystal," *IEEE CPMT Symposium Jpn 2014*. 173-176 (2014).

28. W. Zhu, J.-H. Chao, C. Wang, J. Yao, and S. Yin, "Design and implementation of super broadband high speed waveguide switches," *Proc. SPIE* **9586**, 95860W (2015).

29. M. Ohmi, A. Fukuda, J. Miyazu, M. Ueno, S. Toyoda, and J. Kobayashi, "Development of novel high-speed en face optical coherence tomography system using KTN optical beam deflector," *Appl. Phys. Express* **8**, 027001 (2015).

30. P. Wu and S. Tang, "Wavelength-tunable laser based on electro-optic effect," *Proc. SPIE* **9343**, 934321 (2015).

31. D. Gong, Y. Wu, Y. Liang, W. Ou, J. Wang, B. Liu, and Z. Zhou, "Electric-field-controlled optical beam splitter using the Kerr effect and the Nb/(Ta+ Nb) composition ratio gradient," *Laser Phys*. **25**, 056102 (2015).

32. W. Zhu, J. Yao, J.-H. Chao, and S. Yin, "Alignment free all solid state angularly multiplexed holographic memory systems," *Asian J. Phys*. **24**, 1651 (2015).

33. K. Nakamura, J. Miyazu, Y. Sasaki, T. Imai, M. Sasaura, and K. Fujiura, "Space-charge-controlled electro-optic effect: Optical beam deflection by electro-optic effect and space-charge-controlled electrical conduction," *J. Appl. Phys*. **104**, 013105 (2008).

34. J. Miyazu, T. Imai, S. Toyoda, M. Sasaura, S. Yagi, K. Kato, Y. Sasaki, and K. Fujiura, "New beam scanning model for high-speed operation using $KTa_{1-x}Nb_xO_3$ crystals," *Appl. Phys. Express* **4**, 111501 (2011).

35. S. Tatsumi, Y. Sasaki, S. Toyoda, T. Imai, J. Kobayashi, and T. Sakamoto, "700-kHz beam scanning using electro-optic KTN planar optical deflector," *Proc. SPIE* **9744**, 97440L (2016).

36. T. Imai, J. Miyazu, and J. Kobayashi, "Charge distributions in $KTa_{1-x}Nb_xO_3$ optical beam deflectors formed by voltage application," *Opt. Express* **22**, 14114 (2014)

37. A. Rosen, "High-power optically activated solid-state switches," *Artech House Publishers* (1994).

38. F. J. Zutavern, S. F. Glover, K. W. Reed, M. J. Cich, A. Mar, M. E. Swalby, T. A. Saiz, M. L. Horry, F. R. Gruner, and F. E. White, "Fiber-optically controlled pulsed power switches," *IEEE Trans. Plasma Sci.* **36**(5), 2533–2540 (2008).

39. J. Y. Suen, W. Li, Z. D. Taylor, and E. R. Brown, "Characterization and modeling of a terahertz photoconductive switch," *Applied Physics Letters*, **96**, 14 (2010).

40. F. J. Zutavern, G. M. Loubriel, M. W. O'Malley, W. D. Helgeson, and D. L. McLaughlin, "High gain photoconductive semiconductor switching," *Pulsed Power Conference, Digest of Technical Papers,* Eighth IEEE International, 23-28 (1991).

41. S. Doğan, A. Teke, D. Huang, H. Morkoç, C. B. Roberts, J. Parish, B. Ganguly, M. Smith, R. E. Myers, and S. E. Saddow, "4H–SiC photoconductive switching devices for use in high-power applications," *Appl. Phys. Lett.* **82**(18), 3107–3109 (2003).

42. J. H. Leach, R. Metzger, E. A. Preble, and K. R. Evans, "High voltage bulk GaN-based photoconductive switches for pulsed power applications," *Gallium Nitride Materials and Devices VIII*, **8625**, 86251Z, International Society for Optics and Photonics (2013).

43. J. Wei, Z. Zang, Y. Zhang, M. Wang, J. Du, and X. Tang, "Enhanced performance of light-controlled conductive switching in hybrid cuprous oxide/reduced graphene oxide (Cu2O/rGO) nanocomposites," *Opt. Lett.* **42**(5), 911–914 (2017).

44. L. Tian and W. Shi, "Analysis of operation mechanism of semi-insulating GaAs photoconductive semiconductor switches," *J. Appl. Phys*. **103**(12), 124512 (2008).

45. G. M. Loubriel, J. F. Aurand, G. J. Denison, L. F. Rinehart, D. J. Brown, F. J. Zutavern, A. Mar, M. W. O'Malley, W. D. Helgeson, and L. Carin, "Optically-activated GaAs switches for ground penetrating radar and firing set applications," *Pulsed Power Conference, Digest of Technical Papers*, Twelfth IEEE International, **2**, 673–676 (1999).

46. Y. Ko, R. W. Anderson, and V. S. Arpaci, "Spark ignition of propane-air mixtures near the minimum ignition energy: Part I. An experimental study," *Combust. Flame* **83**(1–2), 75-87 (1991).

47. J.-H. Chao, W. Zhu, C.-J. Chen, S. Yin, and R. C. Hoffman, "Non-uniform space charge controlled KTN beam deflector," *Proc. SPIE* **9958**, 99580S (2016).

48. J.-H. Chao, W. Zhu, C.-J. Chen, A. L. Campbell, M. G. Henry, S. Yin, and R. C. Hoffman, "High speed non-mechanical two-dimensional KTN beam deflector enabled by space charge and temperature gradient deflection," *Opt. Express* **25**, 15481 (2017).

49. J.-H. Chao, W. Zhu, C.-J. Chen, Y.-G. Lee, A. Shang, S. Yin, and R. C. Hoffman, "Ruby fluorescence-enabled ultralong lock-on time high-gain gallium arsenic photoconductive semiconductor switch," *Opt. Lett*. **43**, 3929–3932 (2018).

50. S. Triebwasser, "Study of ferroelectric transitions of solid-solution single crystals of $KNbO_3$-$KTaO_3$," *Phys. Rev*. **114**(1), 63–70 (1959).

51. D. Rytz and H. J. Scheel, "Crystal growth of $KTa_{1-x}Nb_xO_3$ ($0<x\leq0.04$) solid solutions by a slow-cooling method," *J. Cryst. Growth*, **59**(3), 468–484 (1982).

52. A. J. Fox, "Nonlinear longitudinal KTN modulator," *Appl. Opt*., **14**(2), 343–352 (1975).

53. S. Triebwasser, "Behavior of ferroelectric $KNbO_3$ in the vicinity of the cubic-tetragonal transition," *Phys. Rev.* **101**(3), 993–997 (1956).

54. S. Triebwasser, "Method of preparation of single crystal ferroelectrics," *United States Patent* US2954300 (1960).

55. W. A. Bonner, E. F. Dearborn, and L. G. Van Uitert, "Growth of potassium tantalate-niobate single crystals for optical applications," *Am. Ceram. Soc. Bull.* **44**(1), 9–11 (1965).

56. W. R. Wilcox and L. D. Fullmer, "Growth of $KTa_{1-x}Nb_xO_3$ mixed crystals," *J. Am. Ceram. Soc*. **49**(8), 415–418 (1966).

57. A. L. Gentile and F. H. Andres, "A constant temperature method for the growth of KTN single crystals," *Mater. Res. Bull.* **2**(9), 853–859 (1967).

58. P. W. Whipps, "Growth of high-quality crystals of KTN," *J. Cryst. Growth* **12**(2), 120–124 (1972).

59. M. Sasaura, T. Imai, H. Kohda, S. Tohno, M. Shimokozono, H. Fushimi, K. Fujiura, S. Toyoda, K. Enbutsu, A. Tate, K. Manabe, T. Matsuura, and T. Kurihara, "TSSG pulling and LPE growth of $KTa_{1-x}Nb_xO_3$ for optical waveguides," *J. Cryst. Growth* **275**, e2099 (2005).

60. S. R. Sashital, S. Krishnakumar, and S. Esener, "Synthesis and characterization of rf-planar magnetron sputtered $KTa_{1-x}Nb_xO_3$ thin films," *Appl. Phys. Lett*. **62**, 2917 (1993).

61. B. Tunaboylu, S. R. Sashital, P. Harvey, S. C. Esener, and A. Bhalla, "Synthesis and properties of KTN films by sol-gel deposition and RF-magnetron sputtering," *Ferroelectr. Lett. Sect*. **28**, 75 (2001).

62. K. Suzuki, W. Sakamoto, T. Yogo, and S. Hirano, "Processing of oriented $K(Ta,Nb)O_3$ films using chemical solution deposition," *J. Am. Ceram. Soc*. **82**, 1463 (1999).

63. J. Buršík, V. Železnỳ, and P. Vaněk, "Preparation of potassium tantalate niobate thin films by chemical solution deposition and their characterization," *J. Eur. Ceram. Soc*. **25**, 2151 (2005).

64. A. Nazeri, "Crystallization of sol-gel deposited potassium-tantalate-niobate thin films on platinum," *Appl. Phys. Lett*. **65**, 295 (1994).

65. A. X. Kuang, C. J. Lu, G. Y. Huang, and S. M. Wang, "Preparation of $KTa_{0.65}Nb_{0.35}O_3$ thin films by a sol-gel process," *J. Cryst. Growth* **149**, 80 (1995).

66. A. Onoe, A. Yoshida, and K. Chikuma, "Epitaxial growth of orientation-controlled $KNbO_3$ crystal films on MgO using $KTa_{1-x}Nb_xO_3$ intermediate layer by metalorganic chemical vapor deposition," *Appl. Phys. Lett*. **78**, 49 (2001).

67. B. M. Nichols, B. H. Hoerman, J. H. Hwang, T. O. Mason, and B. W. Wessels, "Phase stability of epitaxial $KTa_{1-x}Nb_xO_3$ thin films deposited by metalorganic chemical vapor deposition," *J. Mater. Res*. **18**, 106 (2003).

68. A. Rousseau, M. Guilloux-Viry, E. Dogheche, M. Bensalah, and D. Remiens, "Growth and optical properties of $KTa_{1-x}Nb_xO_3$ thin films grown by pulsed laser deposition on MgO substrates," *J. Appl. Phys*. **102**, 093106 (2007).

69. W. Yang, Z. Zhou, B. Yang, Y. Jiang, Y. Pei, H. Sun, and Y. Wang, "Effect of oxygen atmosphere on the structure and refractive index dispersive behavior of $KTa_{0.5}Nb_{0.5}O_3$ thin films prepared by PLD on Si (0 0 1) substrates," *Appl. Surf. Sci*. **258**, 3986 (2012).

70. K. Korsah, R. Kisner, L. Boatner, H. Christen, and D. Paris, "Preliminary investigation of KTN as a surface acoustic wave infrared/ thermal detector," *Sens. Actuators A Phys*. **119**(2), 358–364 (2005).

71. T. Imai, S. Yagi, Y. Sugiyama, and I. Hatakeyama, "Growth of potassium tantalate niobate single crystal fibers by the laser-heated pedestal growth method assisted by a crystal cooling technique," *J. Cryst. Growth* **147**(3–4), 350–354 (Feb. 1995).

72. J. E. Geusic, S. K. Kurtz, L. G. Van Uitert, and S. H. Wemple, "Electro-optic properties of some ABO_3 perovskites in the paraelectric phase," *Appl. Phys. Lett*. **4**, 141 (1964).

73. X. P. Wang, J. Y. Wang, H. J. Zhang, Y. G. Yu, J. Wu, W. L. Gao, and R. I. Boughton, "Thermal properties of cubic $KTa_{1-x}Nb_xO_3$ crystals," *J. Appl. Phys*. **103**(3), 033513 (2008).

74. A. Reisman and E. Banks, "Reactions of the group VB pentoxides. VIII. Thermal, density and x-ray studies of the systems $KNbO_3$-$NaNbO_3$ and $KTaO_3$-$KNbO_3$," *J. Am. Chem. Soc.* **80**(8), 1877–1882 (1958).

75. Y. Wang, Y. Shen, and Z. Zhou, "Structures and elastic properties of paraelectric and ferroelectric $KTa_{0.5}Nb_{0.5}O_3$ from first-principles calculation," *Phys. B Condens. Matter* **406**(4), 850–853 (2011).

76. Y. Chang, *Field-induced and nanodisordered KTN crystals: properties, devices, and applications* (2014).

77. F. S. Chen, J. E. Geusic, S. K. Kurtz, J. G. Skinner, and S. H. Wemple, "The use of perovskite paraelectrics in beam deflectors and light modulators," *Proc. IEEE* **52**(10), 1258–1259 (1964).

78. J. Y. Wang, Q. C. Guan, J. Q. Wei, M. Wang, and Y. G. Liu, "Growth and characterization of cubic $KTa_{1-x}Nb_xO_3$ crystals," *J. Cryst. Growth* **116**(1–2), 27–36 (1992).

79. J. A. Van Raalte, "Linear electro-optic effect in ferroelectric KTN," *J. Opt. Soc. Am*. **57**, 671 (1967).

80. S. Loheide, S. Riehemann, F. Mersch, R. Pankrath, and E. Krätzig, "Refractive indices, permittivities, and linear electrooptic coefficients of tetragonal potassium tantalate-niobate crystals," *Phys. Status Solidi* **137**(1), 257–265 (1993).

81. H. Fay, "Characterization of potassium tantalate-niobate crystals by electrooptic measurements," *Mater. Res. Bull.* **2**(7), 499–507 (1967).

82. K. Fujiura and K. Nakamura, "KTN optical waveguide devices with an extremely large electro-optic effect," *Proc. SPIE* **5623**, 518–532 (2005).

83. X. Wang, J. Wang, Y. Yu, H. Zhang, and R. I. Boughton, "Growth of cubic $KTa_{1-x}Nb_xO_3$ crystal by Czochralski method," *J. Cryst. Growth* **293**(2), 398–403 (2006).

84. T. Imai, S. Toyoda, J. Miyazu, J. Kobayashi, and S. Kojima, "Permittivity changes induced by injected electrons and field-induced phase transition in $KTa_{1-x}Nb_xO_3$ optical beam deflectors," *Jpn. J. Appl. Phys*. **53**, 09PB02 (2014).

85. W. Zhu, J.-H. Chao, C.-J. Chen, S. Yin, and R. C. Hoffman, "Three order increase in scanning speed of space charge-controlled KTN deflector by eliminating electric field induced phase transition in nanodisordered KTN," *Sci. Rep*. **6**, 33143 (2016).

86. Y.-C. Chang, C. Wang, S. Yin, R. C. Hoffman, and A. G. Mott, "Giant electro-optic effect in nanodisordered KTN crystals," *Opt. Lett*. **38**, 4574 (2013).

87. K. Nakamura, J. Miyazu, M. Sasaura, and K. Fujiura, "Wide-angle, low-voltage electro-optic beam deflection based on space-charge-controlled mode of electrical conduction in $KTa_{1-x}Nb_xO_3$," *Appl. Phys. Lett.* **89**(13), 1115 (2006).

88. S. Tatsumi, Y. Sasaki, S. Toyoda, T. Imai, J. Kobayashi, and T. Sakamoto, "700 kHz beam scanning using electro-optic KTN planar optical deflector," *Optical Components and Materials XIII,* **9744**, 97440L (2016).

89. F. S. Chen, J. E. Geusic, S. K. Kurtz, J. G. Skinner, and S. H. Wemple, "Light modulation and beam deflection with potassium tantalate-niobate crystals," *J. Appl. Phys*. **37**(1), 388–398 (1966).

90. J. P. McKelvey, "Electrostatic fields in inhomogeneous dielectrics," *Am. J. Phys*. **56**(8), 713–718 (1988).

91. R. P. Brinkmann, K. H. Schoenbach, D. C. Stoudt, V. K. Lakdawala, G. A. Gerdin, and M. K. Kennedy, "The lock-on effect in electron-beam-controlled gallium arsenide switches," *IEEE Trans. Electron Devices* **38**(4), 701–705 (1991).

92. P. J. Stout and M. J. Kushner, "Characteristics of an optically activated pulsed power GaAs (Si: Cu) switch obtained by two-dimensional modeling," *J. Appl. Phys.* **77**(7), 3518-3522 (1995).

93. J. B. Gunn, "Instabilities of current in III–V semiconductors," *IBM J. Res. Dev.* **8**(2), 141-159 (1964).

94. A. R. Chowdhury, J. C. Dickens, A. A. Neuber, R. Ness, and R. P. Joshi, "Lock-on physics in semi-insulating GaAs: combination of trap-to-band impact ionization, moving electric fields and photon recycling," *J. Appl. Phys.* **123**(8), 085703 (2018).

95. F. J. Zutavern, G. M. Loubriel, M. W. O'Malley, W. D. Helgeson, and D. L. McLaughlin, "High gain photoconductive semiconductor switching," *Pulsed Power Conference*, *Digest of Technical Papers*, Eighth IEEE International, 23–28 (1991).

96. A. Lastras-Martínez, "Internal quantum efficiency measurements for GaAs light-emitting diodes," *J. Appl. Phys.* **49**(6), 3565–3570 (1978).

97. A. K. Jonscher, C. Pickup, and S. H. Zaidi, "Dielectric spectroscopy of semi-insulating gallium arsenide," *Semicond. Sci. Technol.* **1**(1), 71 (1986).

98. W. Zhu, J.-H. Chao, C.-J. Chen, A. L. Campbell, M. G. Henry, S. Yin, and R. C. Hoffman, "New functionalities of potassium tantalate niobate deflectors enabled by the coexistence of pre-injected space charge and composition gradient," *J. Appl. Phys*. **122**, 133111 (2017)

99. T. Imai, J. Miyazu, and J. Kobayashi, "Measurement of charge density distributions in $KTa_{1-x}Nb_xO_3$ optical beam deflectors," *Opt. Mat. Express* **4**(5), 976–981 (2014).

100. F. Di Mei, L. Falsi, M. Flammini, D. Pierangeli, P. Di Porto, A. J. Agranat, and E. DelRe, "Giant broadband refraction in the visible in a ferroelectric perovskite," *Nat. Photon.* **12**(12), 734–738 (2018).

Appendix A

Selected Publications

Journal Papers

1. **J.-H. Chao**, W. Zhu, C.-J. Chen, Y.-G. Lee, A. Shang, S. Yin, and R. C. Hoffman, "Ruby fluorescence-enabled ultralong lock-on time high-gain gallium arsenic photoconductive semiconductor switch," *Opt. Lett*. **43**, 3929-3932 (2018).
2. **J.-H. Chao**, W. Zhu, C.-J. Chen, A. L. Campbell, M. G. Henry, S. Yin, and R. C. Hoffman, "High speed non-mechanical two-dimensional KTN beam deflector enabled by space charge and temperature gradient deflection," *Opt. Express* **25**, 15481 (2017).
3. **J.-H. Chao**, A. Kshirsagar, and J. Ruzyllo, "Surface Processing for Area Selective Mist Deposition of Nanocrystalline Quantum Dot Films," *ECS Transactions* 58(**6**), 311-316 (2013).
4. W. Zhu, **J.-H. Chao**, C.-J. Chen, A. Shang, Y. G. Lee, S. Yin, M. Dubinskii, and R. C. Hoffman, "Photon excitation enabled large aperture space-charge-controlled potassium tantalate niobate (KTN) beam deflector," *Appl. Phys. Lett*. **112**, 132901 (2018).
5. W. Zhu, **J.-H. Chao**, C.-J. Chen, A. L. Campbell, M. G. Henry, S. Yin, and R. C. Hoffman, "New functionalities of potassium tantalate niobate deflectors enabled by the coexistence of pre-injected space charge and composition gradient," *J. Appl. Phys*. **122**, 133111 (2017).
6. W. Zhu, **J.-H. Chao**, C.-J. Chen, S. Yin, and R. C. Hoffman, "Three order increase in scanning speed of space charge-controlled KTN deflector by eliminating electric field induced phase transition in nanodisordered KTN," *Sci. Rep*. **6**, 33143 (2016).
7. W. Zhu, J. Yao, **J.-H. Chao**, and S. Yin, "Alignment free all solid state angularly multiplexed holographic memory systems," *Asian J. Phys*. **24**, 1651 (2015).

8. A. Sabeeh, Y. Thakur, **J.-H. Chao**, A. Kshirsagar, and J. Ruzyllo, “Methods of Patterned Mist Deposition of Nano-Crystalline Quantum Dot Films,” *ECS Transactions*, 64(**43**), 1-5 (2015).

Conference Proceedings

1. **J.-H. Chao**, W. Zhu, C.-J. Chen, S. Yin, and R. C. Hoffman, "Non-uniform space charge controlled KTN beam deflector," *Proc. SPIE* **9958**, 99580S (2016).
2. **J.-H. Chao**, W. Zhu, C. Wang, J. Yao, S. Yin, and R. C. Hoffman, "Nanosecond speed pre-injected space charge controlled KTN beam deflector," *Proc. SPIE* **9586**, 95860T (2015).
3. C.-J. Chen, **J.-H. Chao**, W. Zhu, A. Q. Shang, Y.-G. Lee, S. Yin, "High outcoupling efficiency blue organic light emitting diodes using an internal tilted nanotube array layer," *Proc. SPIE* **10755**, 1075507 (2018).
4. W. Zhu, **J.-H. Chao**, C.-J. Chen, A. Campbell, M. Henry, S. Yin, and R. C. Hoffman, "Nanosecond KTN varifocal lens without electric field induced phase transition," *Proc. SPIE* **10382**, 103820R (2017).
5. S. Yin, **J.-H. Chao**, W. Zhu, C.-J. Chen, A. Campbell, M. Henry, M. Dubinskiy, and R. C. Hoffman, "A large capacity time division multiplexed (TDM) laser beam combining technique enabled by nanosecond speed KTN deflector," *Proc. SPIE* **10382**, 103820P (2017).
6. W. Zhu, **J.-H. Chao**, C.-J. Chen, S. Yin, and R. C. Hoffman, "Multi-scanning mechanism enabled rapid non-mechanical multi-dimensional KTN beam deflector," *Proc. SPIE* **9958**, 99580R (2016).
7. C.-J. Chen, **J.-H. Chao**, W. Zhu, and S. Yin, "High light extraction efficiency LEDs with asymmetric obtuse angle micro-structured roofs. " *Proc. SPIE* **9958**, 99580T (2016)

8. W. Zhu, **J.-H. Chao**, C. Wang, J. Yao, S. Yin, "Design and implementation of super broadband high-speed waveguide switches," *Proc. SPIE* **9586**, 95860W (2015).

9. C.-J. Chen, W. Zhu, **J.-H. Chao**, H. Zhou, and S. Yin, "A two-dimensional analysis on high light extraction efficiency (LEE) LEDs with asymmetric micro-structured substrate," *Proc. SPIE* **10382**, 103820F (2017)

10 Y.-C. Chang, W. Zhu, **J.-H. Chao**, S. Yin, R. C. Hoffman, A. G. Mott, and C. Luo, "Super broadband ultrafast waveguide switches based on dynamic waveguiding effect," *Proc. SPIE* **9200**, 92000X (2014).

11. A. Q. Shang, Y. G. Lee, W. Zhu, **J.-H. Chao**, C.-J. Chen, S. Yin, "Influence of piezoelectric effect on the performance of high speed KTN deflectors," *Proc. SPIE* **10755**, 107550V (2018).

12. Y. G. Lee, A. Shang, W. Zhu, **J.-H. Chao**, C.-J. Chen, S. Yin, "Analyzing thermal effect of charging and discharging process in KTN crystal for optical beam deflector applications," *Proc. SPIE* **10755**, 107550T (2018).

13. H. Zhou, C.-J. Chen, W. Zhu, **J.-H. Chao**, and S. Yin, "Rapid silicon carbide micro-crystal growth by high power CO2 laser," *Proc. SPIE* **10382**, 103820L (2017).

VITA

Ju-Hung Chao

Mr. Ju-Hung Chao obtained his Bachelor of Science in Electrical Engineering at National Tsing Hua University (Taiwan) in 2008. He joined the master program of electrical engineering at Penn State in 2011 and received his Master of Science degree in electrical engineering in 2013. In the work of his master's thesis, he focused on the surface processing for area selective mist deposition technique for nanocrystalline quantum dots. He then enrolled in the Ph.D. program of electrical engineering at Penn State in 2014 and joined Dr. Shizhuo Yin's research lab. During his Ph.D. studies, he was involved in multiple projects, including ultra-fast free-space optical switches, multi-dimensional KTN beam deflectors, and advanced laser induced triggering techniques with PCSS. He has extensive end to end hands-on experiences of EO device development including theory derivation, mathematical simulation, sample preparation, nanofabrication, electrical characterization and optics experiments. Moreover, he has authored and co-authored a number of journal papers, conference proceedings, and a USA patent.